TECHNISCHE UNIVERSITÄT
KAISERSLAUTERN

AG Magnetismus

Prof. Dr. Burkard Hillebrands

Annual Report 2008

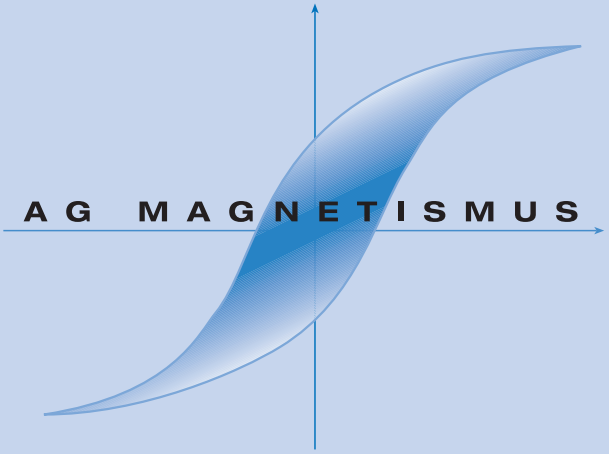

FACHBEREICH PHYSIK

Annual Report 2008

Address:	Prof. Dr. Burkard Hillebrands Fachbereich Physik Technische Universität Kaiserslautern Erwin-Schrödinger-Straße 56 67663 Kaiserslautern, Germany Tel.: +49-(0)631-205-4228 Fax.:+49-(0)631-205-4095
Postal address:	Postfach 3049 67653 Kaiserslautern, Germany
Internet:	http://www.physik.uni-kl.de/hillebrands/
E-Mail:	hilleb@physik.uni-kl.de

Our Group

From left to right:

Roland Neb, Dr. Simon Trudel, Helmut Schultheiss, Dr. Andrii Chumak, Katrin Vogt, Dr. Vitaliy Vasyuchka, Oksana Gaier, Dr. Alexander Serga, Dr. Britta Leven, Dr. Andreas Beck, Dr. Andrés Conca Parra, Sebastian Schäfer, Volker Kegel, Sibylle Müller, Sebastian Hermsdörfer, Christopher Rausch, Christian Sandweg, Thomas Schneider, Björn Obry, Georg Wolf, Dr. Jaroslav Hamrle, Benjamin Jungfleisch, Florin Ciubotaru, Dr. Aleksandra Trzaskowska, Prof. Dr. Burkard Hillebrands

Contents

Chapter 1: Introduction

Dear Colleagues and Friends,

with this report we present our results obtained in the last 12 months, covering the period of November 2007 to October 2008. Again, we feel this was a very successful year for us. We made progress in understanding individual channels of damping in magnetization dynamics, such as via three-magnon scattering processes in small magnetic rings and in nanocontacts, we pushed forward the concept of magnon gases as a model system well suited for studying correlation effects, we investigated magnonic crystals, studied the exchange interaction in Heusler compounds and found a remarkable correlation between the exchange constant and spin-wave stiffness constant with the Curie temperature. Regarding progress in experimental techniques Brillouin light scattering microscopy has now become standard in our laboratory, and phase resolved Brillouin light scattering spectroscopy and microscopy have been largely improved by a newly developed frequency shifter.

The Priority Programme 1133 “Ultrafast magnetization processes” funded by the Deutsche Forschungsgemeinschaft has ended, and we have organized a final International Colloquium in Irsee, Bavaria. The Priority Programme consisted of 18 groups all over Germany who had collaborated within this programme for the maximum time of six years. In Irsee the results were presented to an international audience with many invited experts from the field. We have edited a special cluster issue of Journal of Physics D - Applied Physics comprising papers of almost all of the members of the Priority Programme.

My work as a member of the Senate Board Funding regarding Collaborative Research Centers of the Deutsche Forschungsgemeinschaft has ended after six years of service. This was a very interesting, but time consuming responsibility.

We are happy to welcome several new members of our group. Dr. Vitaliy Vasyuchka has joint us from the National Taras Shevchenko University in Kiev, as well as Dr. Simon Trudel, who has obtained a Humboldt fellowship. New Ph.D. students are Frederik Fohr, Christian Sandweg, Georg Wolf, and new Diploma students are Björn Obry and Christopher Rausch.

Our work would not have been possible without valuable collaborations with people all over the world. They are too many to list them here all. In particular we would like to thank, in alphabetical order, Yasuo Ando, Hartmut Benner, John Chapman, Claude Chappert, Oksana Chubykalo-Fesenko, Darrell Comins, Russell Cowburn, Vladislav Demidov, Sergej Demokritov, Pallavi Dhagat, Bernard Dieny, Günter Dumpich, Hajo Elmers, Jürgen Fassbender, Gerhard Fecher, Claudia Felser, Jacques Ferré, Albert Fert, Suzanna and Paulo Freitas, John Gregg, Kouichiro Inomata, Gerhard Jakob, Albrecht Jander, Martin Jourdan, Boris Kalinikos, Sang-Koog Kim, Peter Kopietz, Mikhail Kostylev, Jürgen Kübler, Liesbet Lagae, Norbert Laube, Wolfram Maaß, Jan Marien, Roland Mattheis, Andrezj Maziewski, Gennadiy Melkov, Jacques Miltat, Alexandra Mougin, Yoshichika Otani, Carl Patton, Dorothée Petit, Kamil Postava, Günter Reiss, Karsten Rott, John R. Sandercock, Rudi Schäfer, Gerd Schönhense, Andrei Slavin, Bob Stamps, André Thiaville, Vasyl Tiberkevich and Stefan Visnovsky for their interactions with us and their strong input to our work.

Collaborations within the Fachbereich Physik at the University of Kaiserslautern (in particular Martin Aeschlimann, James Anglin, Sebastian Eggert, Michael Fleischhauer, Egbert Oesterschulze, Hans-Christian Schneider, Volker Schünemann, Herbert Urbassek and their groups), the Institut für Oberflächen- und Schichtanalytik, as well as the Nano+Bio Center have been very stimulating.

I am much obliged to Peter Pesch and his team from the TZO GmbH for providing convenient general conditions for our work in Rheinbreitbach.

I would also like to thank all our sponsors, which are the Deutsche Forschungsgemeinschaft, the Bundesministerium für Bildung und Forschung, the Humboldt Foundation, the Deutscher Akademischer Austauschdienst, the European Community, INTAS, the State of Rheinland-Pfalz and the University of Kaiserslautern. My special thanks go to Andreas Beck, Thomas Schneider and Sibylle Müller for their help in preparing this report and to Hubert Gerber from Photo-Repro-Druck, TU Kaiserslautern.

It is my special pleasure to greet all former group members. May this report help to stay in touch with each other. If you are interested in our work I would be happy to hear from you. If you have any questions, comments, suggestions, or any kind of criticism, please contact us.

With all my best wishes for Christmas, and a Happy New Year,

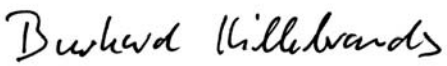

Kaiserslautern, November 2008

Chapter 2: Personnel

2.1 Members of the group

Group leader:

Prof. Dr. Burkard Hillebrands

Senior scientists:

Dr. Britta Leven, Akad. Rätin
Dr. Jaroslav Hamrle
Dr. Alexander Serga

Postdocs and long-term guest scientists:

Dr. Andreas Beck	
Dr. Andrii Chumak	
Dr. Andrés Conca Parra	
Dr. Abdelghani Laraoui	
Dr. Patricia Martin Pimentel	until 12/07
Dr. Simon Trudel (Humboldt Research Fellowship)	since 08/08
Dr. Vitaliy Vasyuchka	since 01/08

PhD students:

Dipl.-Phys. Florin Ciubotaru	
Dipl.-Phys. Frederik Fohr	since 12/07
Dipl.-Phys. Oksana Gaier	
Dipl.-Phys. Sebastian Hermsdörfer	
Dipl.-Phys. Lisa Kleinen (Rheinbreitbach)	
Dipl.-Phys. Roland Neb	
Dipl.-Math. Timo Neumann	
Dipl.-Phys. Christian Sandweg	since 01/08
Dipl.-Phys. Sebastian Schäfer	
Dipl.-Phys. Thomas Schneider	
Dipl.-Phys. Helmut Schultheiss	
Dipl.-Phys. Georg Wolf	since 01/08

Diploma Students:

Björn Obry	since 02/08
Christopher Rausch	since 08/08

Erasmus student:

Ewelina Sieczkowska	until 03/08

Engineers and Technicians

Jörg Elmer (Rheinbreitbach)
Alexander Paul until 11/08
Dipl.-Ing. (FH) Dieter Weller

Secretary:

Sibylle Müller

2.2 Visiting scientists, postdoctoral fellows and exchange students

Dr. Ryszard Gieniusz, University of Bialystok, Poland — 07.04.08 - 04.05.08

Ryszard visited our group as a visiting scientist, coming from the group of Prof. Andrzej Maziewski. In our group he studied the magnetic and elastic properties of thin Mo/Co/Au layered films by means of Brillouin light scattering spectroscopy.

Dr. Mikhail Kostylev, University of Western Australia, Perth, Australia — 15.10.07 - 24.09.08

Mikhail's visit was supported by the Deutsche Forschungsgemeinschaft in the frame of the SFB/Transregio 49 *"Condensed Matter Systems with Variable Many-Body Interactions"*. Mikhail studied parametric instabilities of a spatially confined magnon gas. He was mainly focusing on the theoretical analysis of guided spin-wave bullets in longitudinally magnetized stripes of a ferrimagnetic film.

Prof. Andrei Slavin, University of Rochester, Michigan, U.S.A. — 18.05.08 - 21.06.08

Andrei's visit was supported by the Deutsche Forschungsgemeinschaft in the frame of the SFB/Transregio 49 *"Condensed Matter Systems with Variable Many-Body Interactions"*. During his visit he was working on theoretical studies of evolution of pumping-free magnon gases and condensates.

Dr. Vasyl Tiberkevich, University of Rochester, Michigan, U.S.A. — 18.05.08 - 12.06.08

Vasyl's stay was supported by our Graduate School ("Graduiertenkolleg"). He delivered lectures on nonlinear dynamics of spin-torque nano-oscillators. During his visit he also was working on theoretical description of nonlinear spin-wave processes in thin ferrite films.

Dr. Aleksandra Trzaskowska, Adam Mickiewicz University Poznan, Poland — 01.06.08 - 29.10.08

Aleksandra visited our group as a visiting scientists, coming from the group of Prof. Slawomir Mielcarek. Aleksandra's visit was funded by DAAD. During her stay she familiarized herself with time- and phase-resolved BLS spectroscopy as well as with the BLS microscopy technique. Alexandra was also investigating magnon spectra in structured magnetic films.

Prof. Pallavi Dhagat, Oregon State University, Corvallis, U.S.A. 15.06.08 - 16.09.08

Pallavi was working with us within the SPIN-SAW project on interactions between surface acoustic waves and spin waves. She performed experimental and a theoretical study of magnetoacoustic interaction in thin ferrimagnetic films of yttrium-iron-garnets.

Prof. Albrecht Jander, Oregon State University, Corvallis, U.S.A. 10.06.08 - 05.09.08

Albrecht was staying with us to work within the SPIN-SAW project both on methods of acoustic wave excitation in YIG films and on experimental investigation of scattering of magnetostatic waves by SAW.

Simon Ghionea, Oregon State University, Corvallis, U.S.A. 05.06.08 - 24.09.08

Simon was working in frame of the SPIN-SAW project on excitation of SAW in YIG film by meander-line acoustic transducers.

Richard Przybyla, Oregon State University, Corvallis, U.S.A. 15.06.08 - 11.08.08

Richard's work in frame of the SPIN-SAW project was focusing on excitation of acoustic waves in a ZnO coated YIG film using interdigital transducers.

Prof. Gennadiy Melkov, National Taras Shevchenko
University of Kiev, Ukraine 10.08.08 - 25.08.07

Gennadiy's visit was supported by the Deutsche Forschungsgemeinschaft in the frame of project *"Linear and nonlinear magnonic crystals"*. Gennadiy was participating in experimental and theoretical study of spin-wave dynamics in periodically structured magnetic materials.

Takahide Kubota, Department of Applied Physics,
Graduate School of Engineering, Tohoku University, Sendai, Japan 15.08.08 - 20.08.08

Takahide was staying with us to study Mn_2VAl and $Co_2Mn_{1-x}Fe_xSi$ thin films by means of Brillouin light scattering and magneto-optical Kerr effect magnetometry. His visit was within the existing collaboration between the group of Prof. Y. Ando at the Tohoku University and our group in Kaiserslautern. The collaboration is run within the Research Unit 559 *"New materials with high spin polarization"* funded by the Deutsche Forschungsgemeinschaft and by the NEDO International Joint Research Grant Programm 2004/T093.

Gukcheon Kim, Department of Applied Physics,
Graduate School of Engineering, Tohoku University, Sendai, Japan 15.08.08 - 20.08.08

Gukcheon, coming from the group of Prof. Y. Ando at the Tohoku University, visited our group within the German-Japanese collaboration *"New materials with high spin polarization"* as well. During his stay, he investigated CoPt thin layers by means of Brillouin light scattering and magneto-optical Kerr effect magnetometry.

2.3 Guest seminars

Takahide Kubota 21.10.2007	Tohoku University, Sendai, Japan *Tunneling spin polarization of various ferromagnetic alloys* Gruppenseminar
Dr. Stéphane Mangin 15.11.2007	Nancy-Université, France *Influence of field orientation on current-induced magnetization reversal in nanopillars with perpendicular anisotropy* Sonderseminar
Dr. Vasyl Tiberkevich 28.05.2008	University of Rochester, USA *Nonlinear spin-torque* Seminar Graduiertenkolleg 792
Dr. Stuart P. P. Parkin 22.11.2007	IBM Almaden Research Center, San Jose, California, USA *The magnetic racetrack memory* Sonderseminar
Dr. Dorothée Petit 29.05.2008	Imerial College London, UK *Controlling domain walls in thin ferromagnetic nanowires for ultrahigh density data storage and magnetic logic* Sonderseminar

2.4 Visits of group members at other laboratories

Oksana Gaier	Tohoku University, Sendai, Japan 01.09-17.12.07 Host: Prof. Y. Ando

2.5 Group member photo gallery

Dr. Andreas Beck
Postdoc

Dr. Andrii Chumak
Postdoc

Florin Ciubotaru
Ph.D. student

Dr. Andrés Conca Parra
Postdoc

Jörg Elmer
Technician

Frederik Fohr
Ph.D. student

Oksana Gaier
Ph.D. student

Dr. Jaroslav Hamrle
Senior scientist

Sebastian Hermsdörfer
Ph.D. student

Prof. Dr. Burkard Hillebrands
Group leader

Lisa Kleinen
Ph.D. student

Dr. Abdelghani Laraoui
Postdoc

Dr. Britta Leven
Senior scientist

Patricia Martín Pimentel
Postdoc

Sibylle Müller
Secretary

Roland Neb
Ph.D. student

Timo Neumann
Ph.D. student

Björn Obry
Diploma student

Alexander Paul
Technician

Christopher Rausch
Diploma student

Christian Sandweg
Ph.D. student

Sebastian Schäfer
Ph.D. student

Thomas Schneider
Ph.D. student

Helmut Schultheiss
Ph.D. student

Dr. Alexander Serga
Senior scientist

Ewelina Sieczkowska
Erasmus student

Simon Trudel
Postdoc

Vitaliy Vasyuchka

Dieter Weller
Mechanical engineer

Georg Wolf
Ph.D. student

Chapter 3: Research Topics

The field of magnetism in films and multilayers is still a strongly developing area in modern solid state physics. This is caused both by the challenging developments in the discovery and understanding of the basic physical phenomena, and by the strong impact into industrial applications in the areas of sensors and information storage technology. New mechanisms like interlayer exchange coupling, the giant magnetoresistance effect, the room-temperature tunneling magnetoresistance effect, and, since very recently, spin current phenomena were discovered all within the last one and a half decade. Applications based on these effects were developed, like the magnetic read head based on the giant magnetoresistance effect found in nearly every hard disk drive sold nowadays. The combination with microelectronics, the so-called field of magneto-electronics is strongly expanding and bridging the gap between conventional magnetism and semiconductor physics in view of potential applications in sensor devices and magnetic random access memories, as well as new fields such as magnetic logic.

Most of our research projects are in this field. A main focus is on spin dynamics. We study the eigen-frequency spectrum of excitations of the magnetization on the frequency scale using the Brillouin light scattering technique, and the temporal evolution by time resolved magneto-optic methods. We investigate high frequency properties like spin waves, time dependent magnetization effects, and fast magnetic switching. Recently, our focus shifted strongly towards transport phenomena using linear and nonlinear spin waves.

A key issue is the fabrication of high-quality epitaxial film and multilayer systems and devices using molecular beam epitaxy as prototype systems to study fundamental problems.

In the field of applications we address problems of fast magnetic switching and the exchange bias effect. We transfer our results into actual devices by working closely together with industrial partners.

Magnetic films are very attractive and versatile nonlinear media. Considering spin waves in films as one example of nonlinear waves we study nonlinear effects which are of a great importance for nonlinear science in general.

As a second working area we develop and investigate carbon films for medical applications in the framework of the Institute for Thin Film Technology in Rheinbreitbach.

Overview on projects

1) Epitaxial magnetic films and multilayers: growth, structure and magnetic properties

The preparation of samples with highest possible structural quality and characterization is very important to be able to study magnetic phenomena with the required precision. We achieve this by using molecular beam epitaxy employing the standard *in-situ* methods for chemical and structural analysis. They comprise Auger spectroscopy for chemical analysis, low and high energy electron diffraction, and *in-situ* scanning tunneling and atomic force microscopy. To characterize the magnetic properties we perform *in-situ* Brillouin light scattering spectroscopy and magneto-optic Kerr effect magnetometry. *Ex-situ*, the samples are investigated using Brillouin light scattering spectroscopy, vector Kerr magnetometry, vibrating sample magnetometry, and more. Scientific subjects are magnetic anisotropies induced at interfaces and by controlled

defects, and interlayer coupling effects between magnetic films in multilayers. Special attention is paid to the interplay between the morphology at the interfaces (atomic defects, steps, roughness and interdiffusion) and the magnetic properties.

2) Heusler compounds

Studies of ferromagnetic half-metals are a very interesting topic now for their possible applications in spintronic devices as a potential source of a 100 % spin-polarized current. Heusler alloys are promising candidates for these applications due to their high Curie temperature and expected half-metallicity even for partially disordered systems. Our studies of Heusler compounds are made within the Research Unit (Forschergruppe) 559 *"New Materials with High Spin Polarization"*. Within this network, our main goals are:

- To investigate magnetic properties of Heusler compounds, such as exchange stiffness constant, anisotropy energies, magnetization reversal mechanism as well as magnetic and magneto-optical properties. The main techniques used for those studies are Brillouin light scattering spectroscopy and magneto-optic Kerr effect magnetometry.
- To study the modification of the properties of Heusler compounds using ion irradiation. For this purpose we own a He^+ ion irradiation system. Furthermore, we have a fruitful collaboration with the IFOS, Technische Universität Kaiserslautern and with the Forschungszentrum Dresden-Rossendorf, Dresden (Dr. Jürgen Fassbender). In general, ion irradiation is a very powerful tool to modify magnetic properties of ferromagnets as it allows tuning of magnetic properties as anisotropy, exchange etc. in a controlled way. Furthermore, those changes can be applied with high lateral resolution, below 100 nm.

3) Dynamic magnetic properties of laterally patterned nanostructures

We investigate the basic magnetic properties of systems patterned on the micrometer to nanometer scale. In particular we focus on the domain structure and the change in the spin wave mode spectrum due to lateral confinement effects. We have developed a Brillouin light scattering setup, operating in a Fourier microscope like mode, to obtain sub-micrometer scale spatial information about the distribution of dynamic excitations in small magnetic objects. We also developed a micro-focus Brillouin light scattering system to investigate single magnetic elements. Using these methods we have observed lateral quantization of spin waves in magnetic stripes and rectangular elements. Main results are the observation of quantized modes and of edge modes existing in areas with a large internal field gradient, and static and dynamic coupling effects between magnetic objects. The experiments are accompanied by numerical simulations. A new area is the spin-wave tunneling effect and applications to spin wave logic.

4) Nonlinear properties of high-amplitude spin waves

Spin waves with high precession angles are an interesting object for the investigation of general effects of nonlinear wave propagation in dispersive, anisotropic, and dissipative media. Contrary to nonlinear optical pulses, the spectrum of spin waves can be easily manipulated, by, e.g., changing the orientation and the value of the applied magnetic field. In addition spin waves are much slower than light pulses making their observation easier.

Using the time-resolved Brillouin light scattering technique developed in our lab, we measure the intensity distribution of spin waves propagating in a magnetic film with spatial and temporal resolution. Central problems are: the amplification of spin waves in the linear and nonlinear intensity regimes, the formation of instabilities (e.g. self-focusing), the propagation of nonlinear

excitations (solitons, magnetic “bullets”) and excitations in nonlinear media with a nontrivial topology such as rings. An important development of these studies is the concept of magnon gases with weak and strong correlations.

5) Fast magnetic switching

For memory devices it is of special importance how fast and secure magnetic domains can be written and the magnetization of a single magnetic object can be reversed. The corresponding time scale is in the picosecond to nanosecond regime. In order to investigate these phenomena a time-resolved scanning magneto-optic Kerr microscope has been constructed. The time evolution of the magnetization is sensed stroboscopically. The magnetization dynamics, spin wave propagation effects and in particular the switching behavior of thin magnetic films and nanostructures are investigated.

6) Magnetic nanopatterning

Ion irradiation is an excellent tool to locally modify magnetic properties on the sub-micrometer scale, without substantially affecting the surface topography. This effect is used to magnetically pattern ultrathin films and multilayers using resist masks patterned by electron beam lithography. The major difference between this technique and conventional lithographic techniques is that the environment of the nanostructures can also be magnetic (paramagnetic, antiferromagnetic). A focus is on coupled magnetic systems, such as exchange bias bilayers and exchange coupled trilayers.

7) Exchange bias systems

The investigation of exchange bias systems is of fundamental as well as technological importance. The effect is a shift of the hysteresis loop along the field axis, and it appears in multilayers of coupled ferromagnetic and antiferromagnetic films. In particular we study structurally well characterized epitaxial bilayers. The role of defects and interfacial mixing is investigated using ion irradiation in order to artificially create disorder. Ion irradiation techniques are also applied to modify the magnitude and direction of the exchange bias field. TEM studies are carried out to investigate the structural and magnetic properties as well as their dependency on the irradiation with He^+ and Ga^+ ions. A picosecond all-optical pump-probe setup was developed to study thermal activated unpinning of the exchange coupling at the FM/AF interface. This is of high technological interest, especially for magnetic sensor and storage applications.

8) Biofunctionalized surfaces for medical applications

Amorphous thin carbon films are known to be very biocompatible, and they can be prepared by various deposition techniques to qualify for miscellaneous applications in the biological and medical field. At the Institute for Thin Film Technology we develop in close collaboration with our spin off company NTTF GmbH biocompatible and biofunctionalized surfaces for medical implants, surgical instruments and cellbiological equipment. Currently we are working on carbon coatings for endwelling catheters and cell culture dishes (both made of temperature sensitive polymers) as well as on the development of diffusion barrier coatings on polymers.

Chapter 4: Equipment

A) Preparation and characterization of thin films and multilayers

1. multi–chamber molecular beam epitaxy system (Pink GmbH) comprising
   a. deposition chamber
      (electron beam and Knudsen sources, RHEED, LEED, Auger)
   b. scanning tunneling and needle sensor microscopy chamber
      (*in-situ* STM/needle AFM, Omicron)
   c. Brillouin light scattering and Kerr magnetometry chamber
      (magnetic field 1.2 T, temperature range 80 – 400 K)
   d. load lock chamber
   e. preparation chamber
      (optical coating, heating station 2300 °C)
   f. transfer chamber
   g. atom beam reactor chamber with *in-situ* four point probe resistance measurement stage
2. two-chamber UHV multideposition system
   a. deposition chamber
      (electron beam and Knudsen sources, LEED, Auger)
   b. ion beam chamber with fine focus noble gas keV ion source (Omicron), ion beam oxidation module and mask system
3. two-magnetron sputtering system for hard coatings
4. atomic force microscope (Solver, NT-MDT)
5. clean room facility with flow box, spin coater, etc.

B) Magnetic characterization

1. vector Kerr magnetometer
   (longitudinal and transverse Kerr effect, magnetic field 1.2 T, temperature range 2 – 350 K, automated sample positioning)
2. time-resolved vector Kerr magnetometer (10 ps time resolution and microwave setup for generation of short field pulses)
3. scanning Kerr microscope with time resolution
4. picosecond all-optical pump-probe setup (adjustable delay up to 6 ns; ps-laser Lumera Lasers GmbH)
5. magnetic force microscope with magnet (NT-MDT)
6. three Brillouin light scattering spectrometers, computer controlled and fully automated (magnetic field 2.2 T) with stages for
   a. low temperature measurements (2 – 350 K)
   b. space-time resolved measurements for spin wave intensity mapping (resolution 50 µm, 0.83 ns)

   c. time-resolved BLS microscope (resolution 250 nm, 250 ps)
   d. time-resolved BLS microscope with variable out of plane magnetic field (0.8 T)
   e. *in-situ* measurements
   f. elastic measurements
7. microwave setup (up to 32 GHz) comprising a network analyzer, microwave amplifiers, modulators, pulse generators, etc.
8. magnetotransport setups (magnetic field 1.5 T, temperature range 20 – 400 K)

C) Equipment at the Institute for Thin Film Technologies (IDST), Rheinbreitach

1. Preparation of thin films:
   a. chemical vapor deposition (CVD) facility
   b. physical vapor deposition (PVD) facility
   c. plasma enhanced CVD (PECVD) facilities with an inductively coupled rf-plasma beam source and several magnetrons of different sizes
2. Surface and thin film analysis:
   a. profilometer: measurement of coating thickness and roughness determination of intrinsic stress and Young modulus
   b. Ball on Disk: measurement of friction coefficient analysis of surface friction
   c. Revetest: determination of adhesive strength analysis of microcracks
   d. microindention: determination of plastic and elastic microhardness (Vickers)
   e. optical contact angle measurement: determination of solid surface free energy and surface tension evaluation of hydrophobicity and hydrophilicity
   f. reflection- and transmission-spectroscopy (UV-VIS): optical measurements with wavelength range from 185 nm to 915 nm (resolution 1 nm), determination of absorption coefficient and optical gap (Tauc)
   g. (environmental) scanning electron microscopy (ESEM)[1]: comprehensive structural microanalysis of conducting, isolating, anorganic, organic and wet samples
   h. energy dispersive X-ray microanalysis (EDX)[1]: non-destructive fast analysis of elements
   i. neutron activation analysis (NAA)[2]: qualitative und quantitative analysis of main and trace components
   j. elastic recoil detection analysis (ERDA)[2]: analysis of trace elements with depth resolution analysis of hydrogen content
   k. Rutherford Backscattering (RBS)[2]: analysis of trace elements with depth resolution
   l. synchrotron-X-ray-fluorescence (SYXRF)[2]: non-destructive analysis of elements

[1] in cooperation with NTTF GmbH, Rheinbreitbach

[2] accelarator enhanced analysis in cooperation with the accelarator laboratories of the Universities of Munich, Bonn and Cologne

Chapter 5: Transfer of Technology

1. Magnetism

With our facilities within the Department of Physics at the University of Kaiserslautern we offer consultance and transfer of technology in the areas of thin film magnetism, magnetic film structures and devices, magnetic sensors, and in corresponding problems of metrology.

We are equipped to perform magnetic, transport, elastic and structural measurements of films and multilayer systems.

This is in detail:

- magnetometry using vibrating sample magnetometry, Kerr magnetometry, Brillouin light scattering spectroscopy
- magnetic anisotropies, optionally with high spatial resolution
- magneto-transport properties
- test of homogeneity of magnetic parameters
- exchange stiffness constants in magnetic films
- elastic constants
- surface topography

2. Institut für Dünnschichttechnologie (IDST) - Transferstelle der Technischen Universität Kaiserslautern, Rheinbreitbach

(Institute for Thin Film Technology - Center for Technology Transfer of the University of Kaiserslautern, Rheinbreitbach)

As part of technology transfer the Institute of Thin Film Technology (IDST) offers among other activities

- consultance in tribological problems
- development of product specific coatings
- optimization of coatings especially for medical applications
- coating of polymers and temperature sensitive materials
- coating of samples and small scale production series
- management for R&D-projects

The institute is located in Rheinbreitbach about 20 km south of Bonn in the Center for Surface Technologies (TZO) to support the economy in the northern part of the Rheinland-Pfalz State.

Address:

Institut für Dünnschichttechnologie
Maarweg 30-32
53619 Rheinbreitbach, Germany

Scientific director:

Prof. Dr. B. Hillebrands phone: +49 631 205 4228
e-mail: hilleb@physik.uni-kl.de

Contact:

Lisa Kleinen phone: +49 2224 900 693
fax: +49 2224 900 694
e-mail: kleinen@physik.uni-kl.de

Please contact us for more information.

Chapter 6: Experimental Results

A. Dynamics in Nanostructures and Domain Walls

6.1 DC current control of three magnon scattering processes in spin-valve nanocontacts

F. Ciubotaru, H. Schultheiss, A. Laraoui, S.J. Hermsdörfer, A.A. Serga, B. Leven, and B. Hillebrands[1]

Spintronics research accelerated in response to the theoretical predictions of Slonczewski [1] and Berger [2] in 1996 that the electron spin can interact directly with the magnetization of a magnetic element through the spin transfer torque effect. This effect allows for a spin-polarized current to exchange spin angular momentum with a magnetic element. Not very long after its theoretical prediction, the spin torque effect was experimentally confirmed through the development of nano-scale lithography and fabrication equipment, which allows for the definition and fabrication of very small cross-sectional area devices. This enables the strong confinement of current and associated high current densities required to observe the spin transfer torque effect with the application of a limited bias current. In agreement with theoretical predictions, a spin torque device can experience both current-induced switching [3–5] and steady-state precession of its free magnetic layer [6, 7]. The current-induced switching behavior triggered huge interest for data storage devices such as current-switched magnetoresistive random access memory (MRAM) with lower power consumption. Additionally, spin-torque nano-oscillators can produce microwave radiation when spin-polarized electrons are flowing through a nanocontact to a ferromagnetic thin film. This effect has considerable interest due to a possible application as monochromatic GHz-range sources for integrated electronic circuits.

Here we report on Brillouin light scattering (BLS) microscopy investigations of radiation of nonlinear spin waves within three magnon scattering processes in spin-valve nanocontacts and on the effect of direct current on the threshold properties of these processes.

We have investigated the dynamics of the magnetization in the free layer of extended spin-valve structures ($15 \times 45\,\mu m^2$) with different deposited metallic point contact diameters (d = 80 nm to 200 nm). The entire structure has been fabricated at IMEC, Leuven, Belgium. The multilayer is composed of Ta(3.5 nm) / Cu(16 nm) / Ta(3.5 nm) / Cu(16 nm) / $Ni_{81}Fe_{19}$(2 nm) / IrMn(6 nm) / $Co_{90}Fe_{10}$(5 nm)/ Cu(3.5 nm) / $Ni_{81}Fe_{19}$(7 nm) / Pt(3 nm). The $Ni_{81}Fe_{19}$ (7 nm) acts as a magnetic free layer and the $Co_{90}Fe_{10}$(5 nm) layer, which is exchange biased by the IrMn antiferromagnet, serves as a reference layer for the giant magnetoresistance and spin-transfer measurements (Fig. 1a). The layers are sputter-grown in an ultrahigh vacuum system with a base pressure of $3 \cdot 10^8$ Torr. After patterning by conventional lift-off lithography, the stack is passivated by a 50 nm SiO_2 layer deposited using rf sputtering. After passivation of the magnetic thin film elements with insulating SiO_2, both the micrometer scale side contacts and the nanometer scale point contact are defined in a single e-beam lithography step using a PMMA resist layer. The point contact is established through a nanometer scale hole with a diameter of 80 nm in an insulating SiO_2 layer. The top electrode ends in a very small tip above the point contacts, so that a large part of the magnetic

[1] In collaboration with M. van Kampen, L. Lagae, IMEC, Leuven, Belgium; A.N. Slavin, Department of Physics Oakland, University, Rochester, MI, USA.

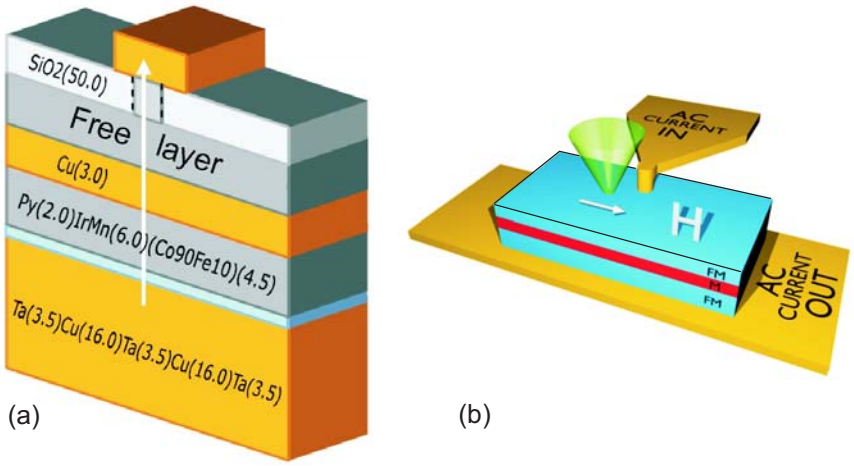

Fig. 1: a) Simplified schematic of the GMR thin film multilayer configuration, showing the bottom electrode, the spin valve stack consisting of an (exchange bias pinned) fixed and free magnetic layer separated by a Cu spacer layer, insulating SiO_2 layer and the top electrode. b) Experimental configuration of measurements with focused light near the point contact in the presence of an external in-plane bias magnetic field H.

layer around the point contact is accessible by the focused laser (Fig. 1b), which is a requirement for Brillouin light scattering microscopy investigations on these devices.

MOKE hysteresis loop measurements gave a coercive field of the free layer as 3.5 Oe. Also, a small bias field of 20 Oe was observed in the free layer switching, which is attributed to the coupling between the magnetic layers. For a point contact with a 80 nm diameter, the electrical resistance is 19.4 Ω and the corresponding magnetoresistance of the spin valve structure is 48 mΩ (= 2.4 % of GMR). Using a bias-tee the device is subjected to an ac microwave and a dc current. The corresponding current densities are in the range of 10^7 to 10^8 A/cm^2. The sample was placed in an external magnetic field H applied in the plane of the magnetic layer, along the long axis of the magnetic element and investigated using Brillouin light scattering microscopy (Fig. 1b). This technique uses a focused laser spot to probe the magnetization of the free magnetic layer around the contact with a spatial resolution of better than 300 nm and a frequency resolution of up to 0.2 GHz [8, 9].

The first experiments aimed to investigate the direct current (dc) induced spin-wave radiation due to the spin torque effect. However, all the point contacts were destroyed by currents over 20 mA and no direct current generated spin-wave emission could be observed. From the microwave RF experiments [10], the typical critical current density required to start spin torque driven vortex oscillations of the magnetization of the free layer is known to be approximately 25 mA and high frequency spin-wave radiation is for substantially larger currents (more than 45 mA) [11]. The early breakdown of the contacts for relatively low currents impede BLS experiments, which are intended to show direct current induced spin-wave emission from a point contact into the free magnetic layer. However in an alternative approach, spin waves can also be resonantly excited through the application of an ac current and manipulated by a dc current.

To obtain an idea of the possible modes of spin waves that can be excited, the device was subjected to an ac current of varying frequencies between 2 GHz and 12 GHz. The BLS intensity spectra were recorded at a fixed position near the point contact and for various amplitudes of the applied external magnetic field. The obtained data of BLS frequency versus ac excitation frequency for 150 Oe and 245 Oe in-plane field is shown in Fig. 2a and Fig. 2b, respectively. The results reveal strong nonlinear effects, namely the generation of eigenmodes with higher frequency (2 f, 3 f)

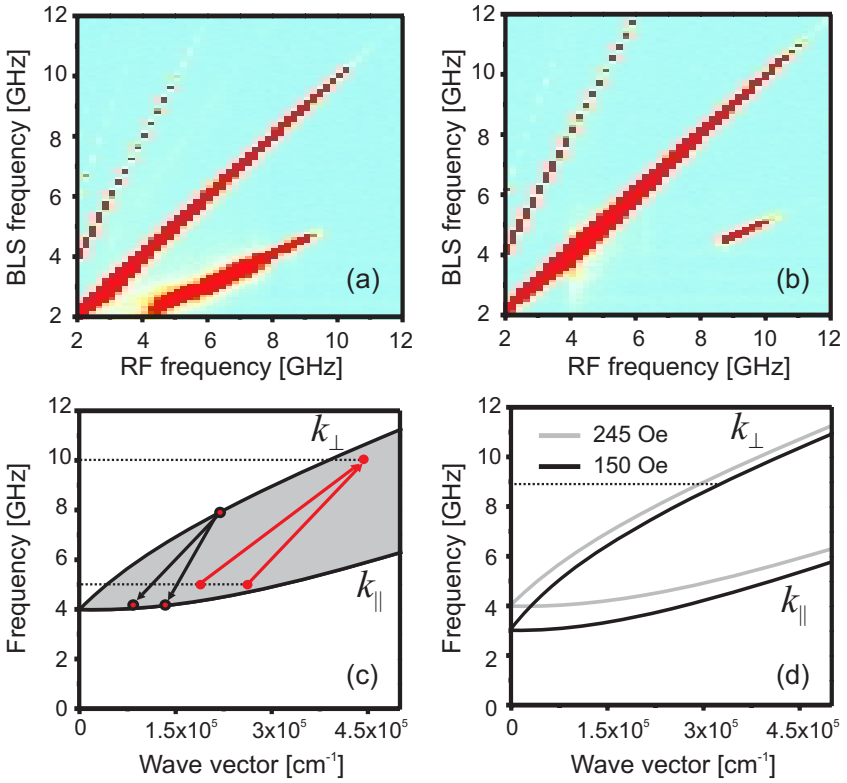

Fig. 2: BLS spectral intensity maps as a function of RF excitation frequency (x-axis) for applied magnetic fields of 150 Oe (a) and 245 Oe (b). For the 245 Oe field, the magnon splitting process is prohibited to produce magnons below approximately 4.45 GHz (i.e. excitation frequency 8.9 GHz). c) Simplified schematic description of three magnons splitting and confluence processes. The top curve corresponds to the MSBVW mode, while the bottom curve represents the MSSW mode and in between is the band of dispersion curves for angles of 0 ° to 90 °. d) Effect of the magnetic field (H = 150 Oe and 245 Oe) on the shift of the dispersion curves.

but also modes with a non integer-factor (0.5 f, 1.5 f) with respect to the exciting microwave frequency f (the diagonal line in the figures). With an increase of the magnetic field the frequency onset for non-integer modes shifts to higher frequencies from 2 GHz for H = 150 Oe to 4.2 GHz for H = 245 Oe. The non-linear modes are associated with three magnon splitting and confluence processes [12], as explained in Fig. 2c. Energy and momentum are conserved in the case of three magnon splitting processes, for example one magnon with a frequency of 8 GHz is split into two magnons with a frequency of 4 GHz each. In the case of an applied field of 245 Oe (Fig. 2b), the splitting process seems to be halted below a threshold excitation frequency close to 8.5 GHz, indicated by the abrupt onset of the $f/2$ signal at this frequency. Apparently, the splitting process cannot produce spin waves with a frequency of less than approximately 4.4 GHz. This threshold can be understood by looking at the dispersion curves displayed in Fig. 2d. They were calculated for a 7 nm thick permalloy film and two values of applied field H = 150 Oe and 245 Oe, takeing into account both dipole-dipole and exchange interactions. The lowest curve corresponds to the magnetostatic backward volume wave (MSBVW) and the highest curve corresponds to the magnetostatic surface wave (MSSW). Within these limits the band of dispersion curves for angles varying from 0 ° to 90 ° between the spin-wave wavevector and the static magnetization direction is defined. One can see that the bottom of the spin-wave band is close to 4 GHz for the field of 245 Oe.

To obtain more information about the effect of dc current on these processes (f and $f/2$ modes), we studied the power dependence of the emitted spin waves as a function of the applied microwave

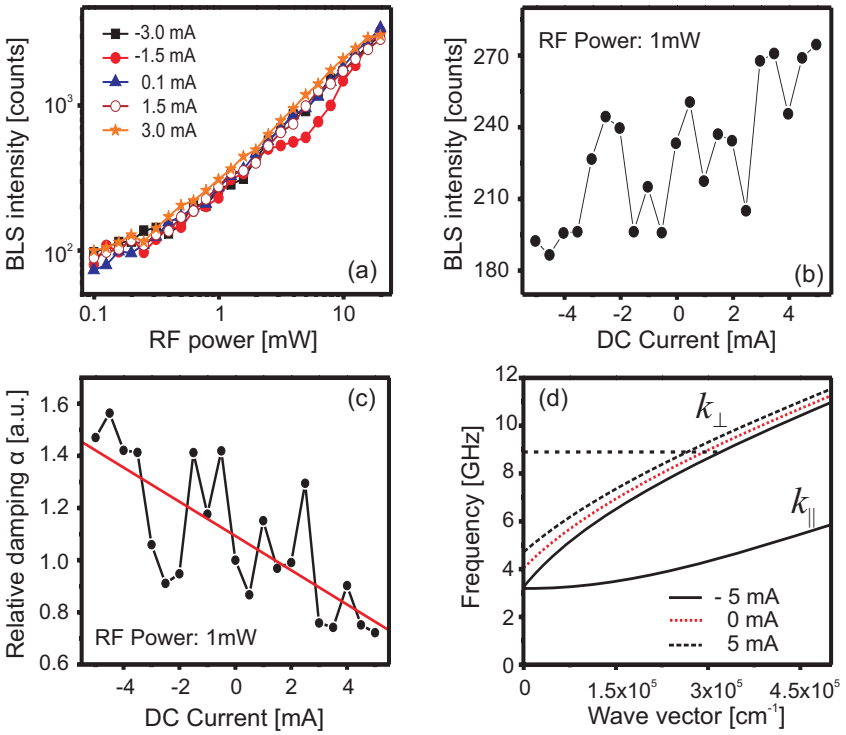

Fig. 3: a) Logarithmic scale BLS intensity of the direct excited spin-wave mode (f) as a function of RF excitation power (x-axis) and dc current for an applied magnetic field of 281.5 Oe and a pumping frequency of 8.9 GHz. b) Normalized BLS intensity of the f mode excited at a fixed RF power of 1 mW as function of the dc current. c) Normalized damping ($\propto$ inverse square root of the BLS-intensity) as a function of the direct current. d) Effect of the Oersted field created by the dc current (dc = -5 mA, 0 mA and 5 mA) on the shift of the magnetostatic dispersion curves.

power and the dc current (current densities up to $10^8\,\mathrm{A/cm^2}$). The measurements were done for a fixed pump frequency of 8.9 GHz and for different values of the externally applied magnetic field. A positive polarity of the current corresponds to a flow of electrons from the bottom electrodes to the top nanocontact electrode.

First, we investigated the effect of a dc current on the directly excited mode f. For an applied magnetic field of 281.5 Oe the resonance mode increases linearly with the increasing applied RF frequency (Fig. 3a) (independent of the dc current). For a fixed output RF power of 1 mW the influence of the dc current leads to an increase of the BLS intensity, as shown in Fig. 3b. The observed influence can be explained both by the spin-torque effect and the effect of the Oersted field created by the dc current. Within the spin-torque effect the effective damping of magnetization dynamics of the free layer is affected by the spin-polarized current. For one polarity of the current the damping of the precession decreases, whereas for the other polarity it increases. Since the damping determines the value of the high-frequency dynamical susceptibility of the medium, the amplitude of the emitted spin waves is increased or reduced depending on the direction of the current. When analyzing this effect, one should take into account that the spin-torque-transfer effect is essential in the nanocontact area. At resonance ($f = f_\mathrm{R}$ is the resonance frequency), the dynamic magnetization m in the nanocontact is connected to the high-frequency dynamical susceptibility [12]:

$$m = \chi h = \frac{f_\mathrm{M}}{2\alpha} h \propto \frac{1}{\alpha} \quad , \tag{1}$$

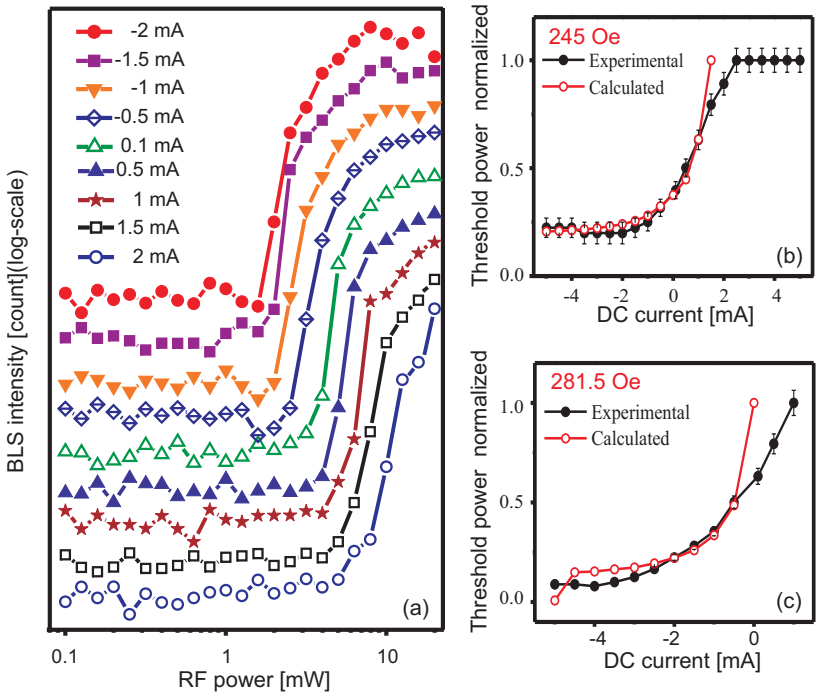

Fig. 4: Logarithmic scale BLS intensity of the half frequency spin-wave mode ($f/2$) as a function of RF excitation power (x-axis) and dc current for applied magnetic field of 245 Oe. Dependence of the power threshold for f/2 spin-wave mode appearance with the dc current and magnetic field (245 Oe (b) and 281.5 Oe (c)).

where $f_M = 4\pi\,\gamma\,M_S$, γ is the gyromagnetic ratio = 2.8 GHz/Oe, M_S is the static saturation magnetization of the free layer = 700 emu/m^3, α is the Gilbert damping, and h is the ac magnetic field. Knowing that the BLS-intensity is proportional to the dynamical magnetization squared and by using equation (1) one can write the damping α as:

$$\alpha \propto \frac{1}{m} = \frac{1}{\sqrt{I_{BLS}}} \quad . \tag{2}$$

One can see from Fig. 3c that the damping decreases with increasing dc current. It should be noted that the values of α are normalized to the one corresponding to zero dc current. This can be explained by the spin-torque-transfer effect, as predicted in [1] and experimentally observed in [13].

Within the Oersted field effect, the magnetostatic dispersion curves shift to high frequencies when the dc current is increased, as expected in the case of an applied magnetic field (Fig. 2d) and calculated in [14]. To investigate this effect, we have measured the effect of dc current on the BLS frequency dependence as a function of the RF frequency. The dc current induces mainly a shift of the frequency threshold of the $f/2$ mode appearance from -3.8 to 4.8 GHz for a current varying between -4 and 4 mA. If we compare these values with the calculated frequency of the bottom dispersion curves for a given magnetic field, we have found best fits for a contribution of an additional field of 160e/1 mA to the effective magnetic field. In fact, this contribution is due to the difference between the two in-plane components of the Oersted field created by the dc current flowing through the nanocontact to the asymmetric top electrode (Fig. 1b). This asymmetry causes an inhomogeneous magnetic field within the point nanocontact area. By using the fitted values of the Oersted field, we have calculated the magnetostatic dispersion curves for different values of the dc current. As shown in Fig. 3d, the Oersted field causes a shift of the dispersion curves to high frequencies. By increasing the Oersted field (dc current) at a fixed pumping frequency of 8.9 GHz the wave vector of the excited spin waves decreases, i.e., the spin waves are excited more efficiently and the BLS intensity increases.

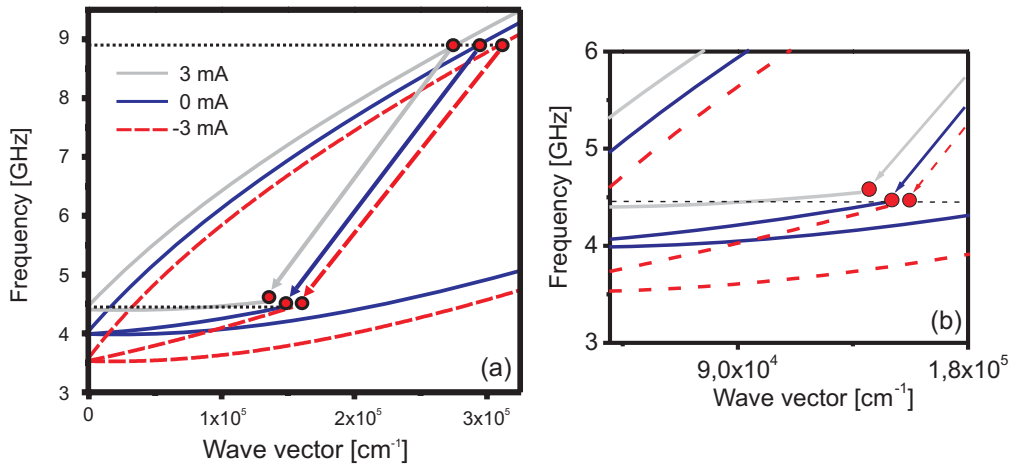

Fig. 5: (a) Effect of the Oersted field on the angle of propagation of f/2 spin-wave modes for different values of the dc current (−3 mA, 0 mA and 3 mA). With changing the Oersted field created by the dc current and working at a fixed pumping frequency of 8.9 GHz, the excited $f/2$ modes are propagating with different angles θ_k with respect to the direction of the static magnetization (∥ to H). For a critical current I_{dc} of 0 mA the angle θ_k is 15.75° and for I_{dc} of −3 mA θ_k is 24.52°. For a dc current of 3 mA, the excitation of the $f/2$ mode is forbidden due the shift of the bottom of the spin-wave band (5 GHz) to high frequencies greater than the half of the pumping frequency (4.45 GHz) (b).

We have also investigated the dependencies of the $f/2$ mode as a function of the RF power and dc current. Without applying any dc current, the intensity of the $f/2$ mode shows a threshold behavior with respect to the applied RF power, as can be seen in Fig. 4a (H = 245 Oe). In the presence of a dc current the power threshold for the $f/2$ mode excitation (Fig. 4a) can be tuned. In Figs. 4b and 4c we plot the power threshold of the $f/2$ mode appearance as a function of the dc current for a magnetic field H = 245 Oe and 281.5 Oe, respectively. For both values of the magnetic field, the threshold power increases nonlinearly with increasing dc current. In addition, for negative currents a saturation is observed for both applied fields. For positive currents the saturation was not seen for an applied field of 281.5 Oe due to the power threshold shift to higher values, more than 20 mW for dc currents up to 1 mA, and to the limited output of our microwave source (= 20 mW). The observed influence of the dc current on the threshold properties of the half frequency spin-wave mode is not compatible with the spin torque effect. This should lead to a linear decrease of the internal damping while increasing the current [1, 7].

To explain the experimental data, we calculated the threshold power dependence with the dc current by taking into account the effect of the Oersted field created by the current in the free Py layer. The model is based on a calculation of the band of spin waves between MSBVW and MSSW geometries as a function of the dc current and with a contribution of the Oersted field of 16 Oe for 1 mA. As seen in Fig. 5a, by applying a dc current the dispersion curves shift to lower frequencies for a current of −3 mA and to higher frequencies for a current of 3 mA (3 mA corresponds to an Oersted field of 48 Oe). For example, the frequency of the bottom dispersion curve increases from 3.5 GHz to 5 GHz with an increase of the dc current from −3 mA to 3 mA. By changing the Oersted field and working at a fixed pump frequency of 8.9 GHz, the excited $f/2$ modes propagate at different angles θ_k with respect to the direction of the static magnetization (∥ to H). For example for I_{dc} = 0 mA the corresponding angle is θ_k = 15.75° and for I_{dc} = −3 mA the angle is 24.52°. In the case of a dc current of 3 mA, the excitation of the $f/2$ mode is not possible due the shift of the bottom of the spin-wave band (5 GHz) to higher frequencies greater than half of the pumping frequency (4.45 GHz) and because the conditions for three magnon splitting processes are not

satisfied (Fig. 5b). By extracting the angle of propagation θ_k of $f/2$ spin-wave modes from the dispersion curves we can easily calculate the threshold power using the formulas [12]:

$$P_{\mathrm{thr}} \propto (h_{\mathrm{thr}})^2 \quad , \tag{3}$$

$$h_{\mathrm{thr}} = \frac{2 f f_{\mathrm{r}}^2}{\gamma f_{\mathrm{M}} \sin(2\theta_k)(\frac{f}{2} + f_{\mathrm{H}})} \quad . \tag{4}$$

where h_{thr} is the threshold field, f is the pump frequency (8.9 GHz in our case), $f_{\mathrm{H}} = \gamma$ H, and $f_{\mathrm{r}} = \alpha\, f_{\mathrm{H}}$. By using Eq. (3) and (4), and the values of θ_k extracted from the dispersion curves we calculated the normalized threshold power dependence with the dc current in the range of -5 to 5 mA. The results of the normalized threshold power as a function of the dc current (Oersted field) are plotted in Figs. 4b and 4c for two values of the applied magnetic field of 245 Oe and 281.5 Oe, respectively. The difference between the experiment and the theory is mainly generated by the magnetic inhomogeneities which are not taken into account in the calculations. In theory, increasing the dc current should cause a decrease in θ_k (tends to 0°), i.e, the threshold power approaches the infinity for a critical current I_{dc}. I_{dc} = 2 mA for an applied magnetic field H of 281.5 Oe and I_{dc} = 1 mA for H = 245 Oe. Above this critical current the conditions of three magnon splitting are not fulfilled. The good agreement between the calculated data and the experimental results demonstrates that the threshold properties of the $f/2$ mode are mainly controlled by the Oersted field.

In conclusion, we investigated the magnetization dynamics in spin-valve nanocontacts (D = 80 nm) under the influence of applied ac and dc current by means of Brillouin light scattering microscopy. Strong nonlinear spin waves are excited with the ac current and discussed within the framework of three magnon scattering. In the presence of a dc current the efficiency of the directly excited f mode can be enhanced. This effect can be explained by both spin transfer and Oersted field effects. In addition, the threshold properties for $f/2$ excitation can be controlled by the Oersted effect created by the current injected through the nanocontact.

This work was supported by the European Commission within the EU-MRTN SPINSWITCH (MRTN-CT-2006-035327) and by the Deutsche Forschungsgemeinschaft within the SPP1133.

References

[1] J.C. Slonczewski, J. Magn. Magn. Mater. **159**, L1-L7 (1996).
[2] L. Berger, Phys. Rev. B **54**, 9353 (1996).
[3] J.A. Katine, F.J. Albert, R.A. Buhrman, E.B. Myers, D.C. Ralph, Phys. Rev. Lett. **84**, 3149 (2000).
[4] J. Grollier, V. Cros, A. Hamzic, J.M. George, H. Jaffrès, A. Fert, G. Faini, J. Ben Youssef, H. Legall, Appl. Phys. Lett. **78**, 3663 (2001).
[5] T.Y. Chen, Y. Ji, C.L. Chien, Appl. Phys. Lett. **84**, 380 (2004).
[6] W.H. Rippard, M.R. Pufall, S. Kaka, S.E. Russek, T.J. Silva, Phys. Rev. Lett. **92**, 027201 (2004).
[7] S.I. Kiselev, J.C Sankey, I.N. Krivorotov, N.C. Emley, R.J. Schoelkopf, R.A. Buhrman, D.C. Ralph, Nature **425**, 380 (2003).
[8] V.E. Demidov, S.O. Demokritov, B. Hillebrands, M. Laufenberg, P.P. Freitas, Appl. Phys. Lett. **85**, 2866 (2004).
[9] K. Perzlmaier, M. Buess, C.H. Back, V.E. Demidov, B. Hillebrands, S.O. Demokritov, Phys. Rev. Lett. **94**, 057202 (2005).
[10] Q. Mistral, M. van Kampen, G. Hrkac, J.-V. Kim, T. Devolder, P. Crozat, C. Chappert, L. Lagae, T. Schrefl, Phys. Rev. Lett. **100**, 257201 (2008).
[11] X.G.H. Janssens, *Spin Wave Emission from Point Contact Spin Torque Nano-Oscillators*, Technische Universiteit Eindhoven (2007).
[12] A.G. Gurevich, G.A. Melkov, *Magnetization Oscillations and Waves*. Boca Raton, FL: CRC (1996).
[13] V.E. Demidov, S.O. Demokritov, G. Reiss, K. Rott, Appl. Phys. Lett. **90**, 172508 (2007).
[14] M.A. Hoefer, T.J. Silva, M.D. Stiles, Phys. Rev. B **77**, 144401 (2008).

6.2 Dissipation of spin-wave modes due to mode coupling in $Ni_{81}Fe_{19}$ rings

B. Obry, H. Schultheiss, C. Sandweg, S. Hermsdörfer, S. Schäfer, P.A. Beck, B. Leven, and B. Hillebrands

The topic of spin waves in magnetic nanostructures has recently been addressed to a great extent due to its importance for the understanding of fundamental questions in magnetization dynamics as well as technological applications. Especially microscopic ring structures made from $Ni_{81}Fe_{19}$ with a magnetization configuration in the onion state have been investigated concerning their coherence and dissipation properties with respect to spin waves [1, 2]. It has been shown that the excitation spectrum is quantized for rings with diameters of 1 µm and becomes continuous for a ring of 3 µm diameter, showing a transition from coherence to partial decoherence. Furthermore, two different kinds of excitation spectra have been found with distinct frequencies, the first appearing at the pole regions of the rings (0 °, 180 °, see inset of Fig. 1), the second at the equator regions (90 °, 270 °). The dissipation behaviour of those two excitation modes has also been investigated and quantitatively analyzed.

Here it will be shown that the coupling of two eigenmodes in a ring represents one possible dissipation channel, where the two coupled eigenmodes are at the pole and equator regions, given a proper external static magnetic field and a suitable excitation frequency.

We report on the investigation of permalloy ($Ni_{81}Fe_{19}$) rings placed on top of a coplanar waveguide (Fig. 1). The waveguide consists of a 200 nm thick Au layer and a central strip line with a width of 20 µm. By using molecular beam epitaxy in a UHV system with subsequent electron lithography, utilizing a lift-off technique, permalloy rings with a thickness of 15 nm are fabricated on top of the Au layer. Different outer diameters of 1, 2 and 3 µm as well as different widths of 100, 200 and 400 nm make it possible to investigate the influence of the ring size on the mode coupling. In order to exclude magnetostatic and dynamic coupling of two adjacent rings, their distance to each other is

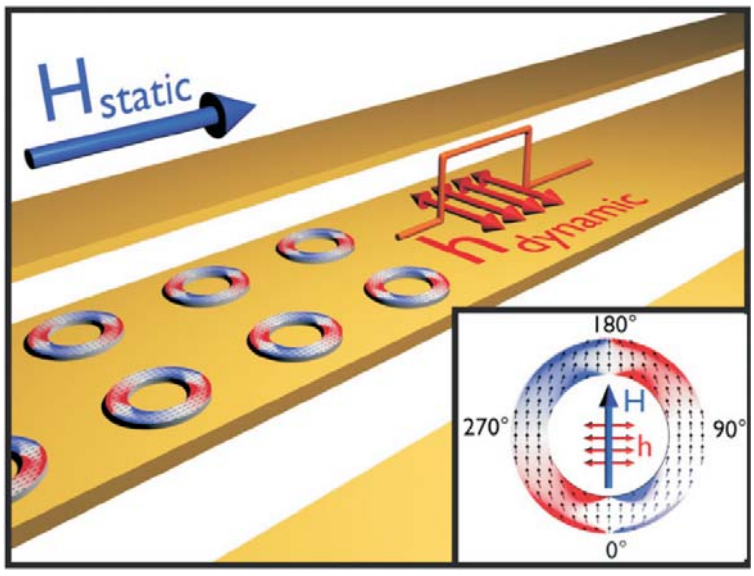

Fig. 1: Sample structure. Permalloy rings with diameters between 1 µm and 3 µm, widths between 100 nm and 400 nm and a thickness of 15 nm are placed on top of a coplanar Au waveguide. The inset shows the magnetization configuration of a ring in the onion state. **H** indicates the static external magnetic field, whereas **h** is the dynamic Oersted field created by a microwave current in the coplanar waveguide.

twice the ring diameter. The magnetization configuration of the rings is initialized to the onion state by saturating the sample by an in-plane magnetic field **H** parallel to the axis of the waveguide (see inset of Fig. 1). Optimizing the total energy of the system, the magnetization will try to align with the ring boundaries in order to minimize demagnetizing fields and with **H** for magnetostatic energy reasons. Thus there exist regions where the magnetization is aligned perpendicular to the ring perimeter due to the large value of **H**, called pole regions (0°, 180°), whereas the magnetization aligns parallel to the ring perimeter at the so-called equator regions (90°, 270°). Application of a microwave current through the waveguide results in a dynamic Oersted field, which is oriented concentrically about the waveguide. The rings on top of the waveguide thus experience the Oersted field as a sinusoidal in-plane magnetic field with frequencies in the GHz range, corresponding to the excitation frequencies of spin waves in the rings. Hence spin waves will be excited, if the microwave frequency matches an eigenfrequency of the magnetic system. This excitation is most effective for the case of perpendicular orientation between the dynamic Oersted field vector and the vector of the internal magnetization of the ring. As can be seen from the inset in Fig. 1, the regions where this condition is fulfilled are the two pole regions (0°, 180°) and the two equator regions (90°, 270°).

Pole and equator regions will exhibit a different behavior, if a microwave current is applied. The resonance frequency of the spin-wave excitation, i.e., the microwave frequency which gives the largest spin wave signal, turns out to be lower at the pole than at the equator [1]. Hence there exist two different eigenmodes in the ring, the pole mode and the equator mode. Figure 2 shows the spin-wave signal dependence on the applied microwave frequency, measured with Brillouin light scattering microscopy at the pole region (black lines) and at the equator region (grey lines) for three different values of the external static magnetic field **H**. The applied microwave frequency was varied from 2 GHz to 6 GHz. The resonance condition changes with **H**. Decreasing the external field causes a decrease of the resonance frequency for both the pole and equator regions. Note that the magnitude of the resonance excitation signal at the equator increases. For $\mathbf{H} = 150\,\mathrm{Oe}$ the resonance frequency at the pole is 2.4 GHz, whereas it is 4.9 GHz at the equator, i.e., about twice the pole resonance frequency. As explained below, a frequency ratio of 2:1 is the necessary condition for having a coupling between pole and equator modes.

The existence of mode coupling can be seen from the intensity graph in Fig. 3a. Therefore, BLS spectra were taken at each point along the ring perimeter. In the intensity graph the detected spin wave signal for a given azimuthal angle α and a given frequency, expressed in terms of the

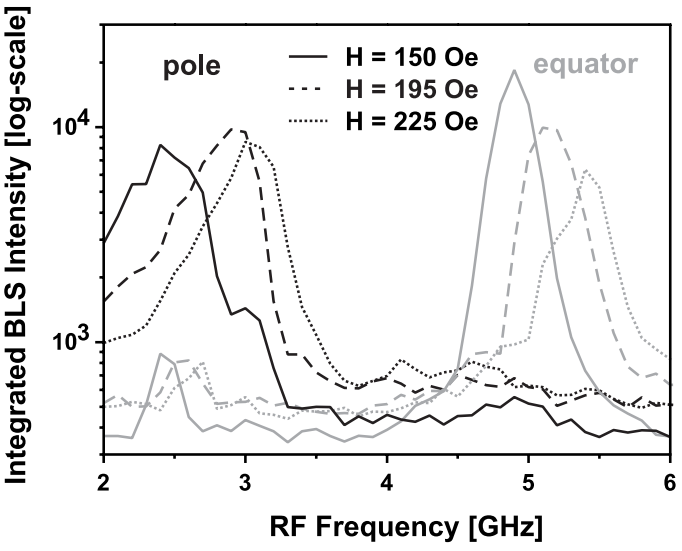

Fig. 2: FMR-type microfocus Brillouin light scattering measurement. The BLS intensity is plotted over the RF excitation frequency for different values of the external magnetic field **H**. The black curves correspond to BLS scans at the pole (0°, 180°) of the ring, the results measured at the equator (90°, 270°) are displayed in grey.

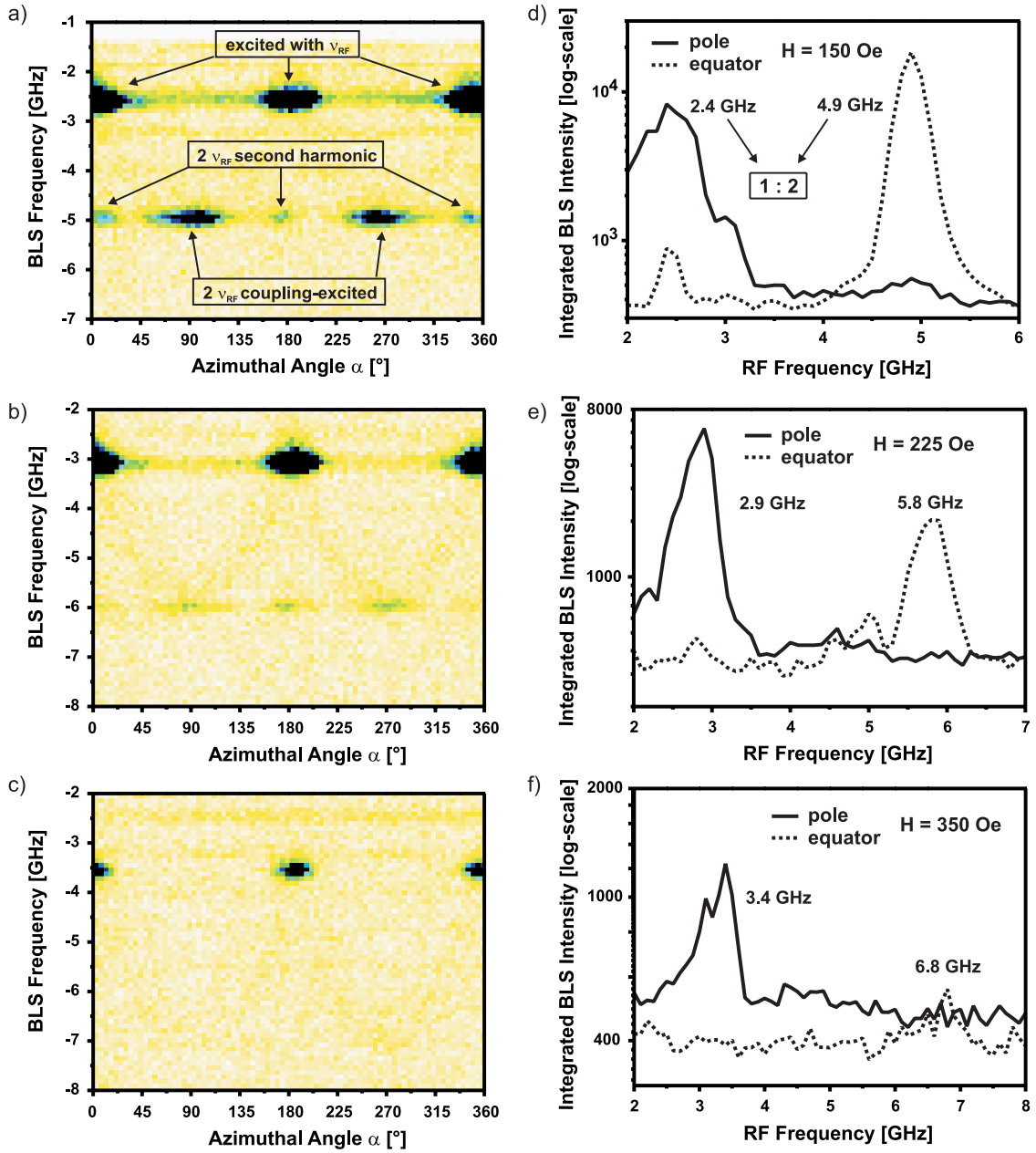

Fig. 3: Microfocus BLS measurements for a ring with 3 µm diameter and varying ring width of 400 nm (a,d), 200 nm (b,e) and 100 nm (c,f). In (a-c) the strength of mode coupling is indicated: Applying an RF frequency of ν_{RF} there can be seen the directly excited pole mode but also a signal with $2\nu_{RF}$ at the equator. Note the negative BLS frequencies as the measurements are made in Stokes condition. In (d-f) the corresponding FMR-type measurements are displayed for a value of the external magnetic field **H** at which the resonance frequency at the pole is half the resonance frequency at the equator. From a to c the coupling gets weaker with decreasing ring width as well as the ratio of the directly-excited equator mode intensity and the directly-excited pole mode intensity (d to f).

BLS frequency shift, is shown. In this case a microwave current with a frequency of 2.4 GHz is applied to the coplanar waveguide, in order to excite only the pole mode, which has its maximum amplitude at $\alpha = 0^\circ$ and 180°. The external static magnetic field was set to $\mathbf{H} = 150$ Oe. In agreement with the former measurements, the intensity graph in Fig. 3a exhibits a large spin-wave signal at the pole regions $\alpha = 0^\circ, 180^\circ$ with a spin-wave frequency of $\nu = 2.4$ GHz. Furthermore, at the same azimuthal positions, the second harmonics of the pole mode appear with twice the

microwave frequency and smaller amplitude. However, two more spin-wave signals are measured with a spin-wave frequency of twice the microwave frequency but at the equator positions $\alpha = 90\,^{\circ}$, 270°. Thus the equator mode seems to be excited, although the applied microwave frequency is far off the equator resonance frequency. Hence there must be some coupling between the pole mode and the equator mode, which enables the equator mode excitation by means of the pole mode. Note that the equator mode signal cannot be any second harmonic signal, since there are no spin waves detected in the equator regions for the microwave frequency $\nu = 2.4\,\mathrm{GHz}$.

Figure 4 again shows the spatial distribution of the spin-wave intensity as a function of the azimuthal angle, extracted from the intensity graph in Fig. 3a. The solid line corresponds to the signal, which is measured at $\nu = \nu_{RF} = 2.4\,\mathrm{GHz}$, while the dotted line indicates the detected spin waves with a frequency of about $\nu = 4.8\,\mathrm{GHz}$.

A possible explanation of the coupling mechanism can be found in magnon-magnon-scattering processes, especially in the special case of three-magnon-scattering. Consider two magnons of the same frequency ν_{RF} scattering and combining to create one magnon of the sum of the original frequencies $2\nu_{RF}$. Translating that into our case there would be two magnons at the pole, which are produced by the microwave excitation, combining by three-magnon-scattering into one magnon of twice the microwave frequency. Since there is the equator mode at this frequency, it is energetically favourable for that resulting magnon to have the maximum mode amplitude at the equator. Furthermore and going more into detail, the nonlinear terms of the Landau-Lifshitz-Gilbert equation could be taken into consideration, which account for the appearance of a signal with double frequency $2\nu_{RF}$. This additional spin wave at the pole will couple to the equator mode by dipolar interaction. This theory is supported by the fact that a large indirectly excited signal at the equator coincides with a large second harmonic signal at the pole (cf. Fig. 3). Note that magnon-magnon-scattering is also a nonlinear process, which is connected to the dipolar interaction.

In the following we investigate the dependence of the mode coupling strength on the given ring geometry. The main differences appear between rings of different widths. The three intensity graphs from Fig. 3 correspond to rings of 3 µm diameter and a width of 100 nm, 200 nm and 400 nm, respectively. However, the coupling condition for the 100 and 200 nm widths are achieved at different external magnetic field values and apparently the resonance frequency of the pole mode deviates as well. Hence the ring with a width of 100 nm is excited with a microwave frequency of $\nu_{RF} = 3.4\,\mathrm{GHz}$ in an external static magnetic field of $\mathbf{H} = 350\,\mathrm{Oe}$ while for the 200 nm width the conditions are $\nu_{RF} = 2.9\,\mathrm{GHz}$ and $\mathbf{H} = 225\,\mathrm{Oe}$.

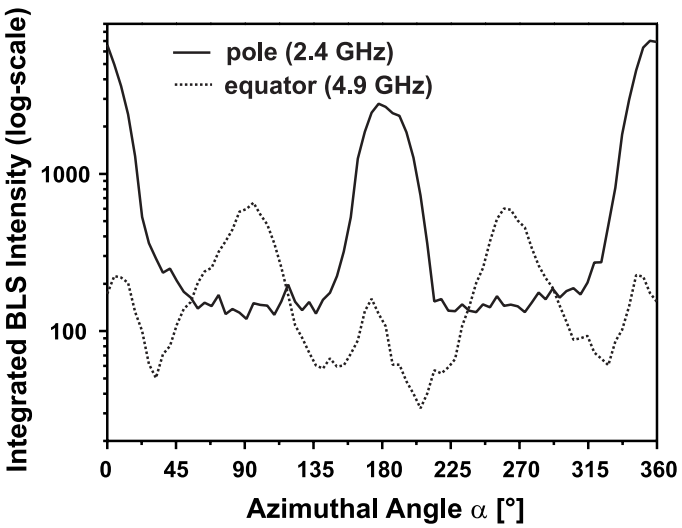

Fig. 4: Spatial BLS intensity distribution along the ring perimeter, measured for an external magnetic field of $\mathbf{H} = 150\,\mathrm{Oe}$ and an RF excitation frequency of $\nu = 2.4\,\mathrm{GHz}$ at both pole (solid) and equator (dotted). The azimuthal angle α is defined as in the inset of Fig. 1. The measured spin-wave frequency for the pole mode was $\nu = 2.4\,\mathrm{GHz}$, whereas it was $\nu = 4.8\,\mathrm{GHz}$ for the equator mode. The measurement was done for a ring of 3 µm diameter and 400 nm width.

When exciting spin waves in the ring with a microwave current, which equals the pole resonance frequency, the equator mode signal increases with increasing ring width (Fig. 3). While there is a large spin-wave signal at the azimuthal angles 90 ° and 270 ° for twice the microwave frequency in the rings with 400 nm width, the spin-wave signal of the equator mode gets lower for ring widths of 200 nm and the signal cannot be detected for the 100 nm rings. It has to be mentioned that the overall BLS intensity decreases with decreasing ring width. But comparing the equator-mode signal with the second harmonic signal of the pole mode in the three graphs, there is a clear change in the relative intensities, too. The equator-mode signal for the width of 400 nm is much larger than the second-harmonic signal, whereas both signals exhibit about equal intensities in the case of the 200 nm rings. It follows that the coupling strength decreases with decreasing ring width.

The reason for that change in the coupling strength can be found by comparison of the frequency resonance measurements displayed in Fig. 3d-f. Those measurements were performed in order to determine the magnetic field value **H** and the microwave frequency that are needed to fulfill the coupling condition of having a resonance frequency of the equator mode which is twice the resonance frequency at the pole. The three graphs show BLS intensities measured at the equator (higher frequencies) and at the pole (lower frequencies) as a function of the microwave frequency, which was varied from 2 GHz to 6 GHz, 7 GHz and 8 GHz, respectively. The static external magnetic field is chosen to fulfill the coupling condition for the resonance case. Note that in these measurements both the pole and equator modes are directly excited. Taking into account the absolute intensities in the resonance cases, the decrease of the overall BLS intensity is resembled. That is due to the fact that the coupling condition requires a lower external magnetic field for a broader ring. Thus the magnetization within the ring is more easily excited by the dynamic Oersted field, which remains constant in amplitude. The ratio of pole and equator mode intensities, however, turns out to change as well. The equator mode dominates the pole mode in the case of the 400 nm ring width, while both modes are equal for a ring width of 200 nm. For the 100 nm rings the equator mode is much less intense than the pole mode. This is possible since the internal magnetic field of the ring in the onion state depends on the external magnetic field only at the equator, whereas it is influenced by the external magnetic field as well as demagnetizing fields at the pole [1]. Thus the efficiency of exciting spin waves, which depends on the internal magnetic field, changes differently with the ring width for the respective modes. Therefore it can be concluded that the mode coupling strength depends on the ratio of both the directly excited equator and pole mode intensities. The larger the ring width, the stronger is the coupling.

In conclusion we identified three-magnon-scattering as one possible mechanism of energy dissipation in microscopic permalloy rings magnetized in the onion state. By means of this process, energy can be transferred from the pole mode of the ring into the equator mode, if the coupling condition is fulfilled. The coupling condition requires a frequency ratio of the pole eigenfrequency and the equator eigenfrequency of 1:2, which can be tuned by the external magnetic field.

The authors acknowledge fruitful discussions with Vasyl Tiberkevich, Andrei Slavin, Robert Camley, Carl Patton. The authors acknowledge the Nano+Bio Center (Sandra Wolff, Bert Lägel, and Christian Dautermann) of the University of Kaiserslautern for technical support during the sample processing. Financial support by the DFG within the Priority Program SPP1133 is acknowledged.

References

[1] H. Schultheiss, S. Schaefer, P. Candeloro, B. Leven, B. Hillebrands, A.N. Slavin, Phys. Rev. Lett. **100**, 047204 (2008).

[2] H. Schultheiss, C.W. Sandweg, B. Obry, S. Hermsdoerfer, S. Schaefer, B. Leven, B. Hillebrands, J. Phys. D **41**, 164017 (2008).

6.3 Investigation of the lifetime of quantized spin waves in nano-scaled magnetic ring structures

H. Schultheiss, C.W. Sandweg, B. Obry, S. Hermsdörfer, S. Schäfer, P.A. Beck, B. Leven, and B. Hillebrands

The investigation of the magnetic excitation spectrum of magnetic nano-structures is of large importance for the fundamental understanding of the magnetization dynamics as well as for technological applications. The demands concerning speed and reliability for future logic and data storage devices are pushing the operating frequency towards the GHz-regime – the typical time-scale of spin waves, the fundamental excitations of the magnetization. Since the discovery of the spin-wave quantization effect in patterned magnetic thin films [1, 2] many works focused on the research of eigen-excitations in magnetic media with a reduced dimensionality. The amplitude profile, the discrete frequencies and the quantization conditions of spin-wave eigenmodes in stripes [1–4], rectangles [4, 5], disks and ellipses [6, 7] are now well understood and allow nowadays even for an engineering of the spin-wave eigenmode spectrum in such a small magnetic structure taking into account issues of geometric shape, multilayer stacks, and even magnetic domain structure.

The magnetization dynamics of rings magnetized in the onion state show a large richness of possible eigenmodes. Quantization of spin waves takes place not only due to the confinement in radial and azimuthal direction in the so-called equatorial regions at 90° and 270° (see inset in Fig. 1 for the definition of the angular positions) but also in spin-wave wells in the so-called pole regions at 0° and 180° created by the inhomogeneity of the total internal field [8]. The spatial profiles of these eigenmodes have been widely discussed in the last years by several research groups [8–13] and it is well known, that low-frequency spin waves are located at the poles of the onion state whereas in the equatorial regions confined spin waves with higher frequencies are present with nodes either in azimuthal or radial direction, depending on the excitation.

In the real world modes are not true eigenmodes in a sense, that they are not totally decoupled from the environment and from each other. They are weakly coupled to the environment, i.e. to the lattice, and thus they are weakly lossy. So far the problem of dissipation has been rarely addressed. In [8] the issue of finite coherence length of spin waves in a ring structure is discussed.

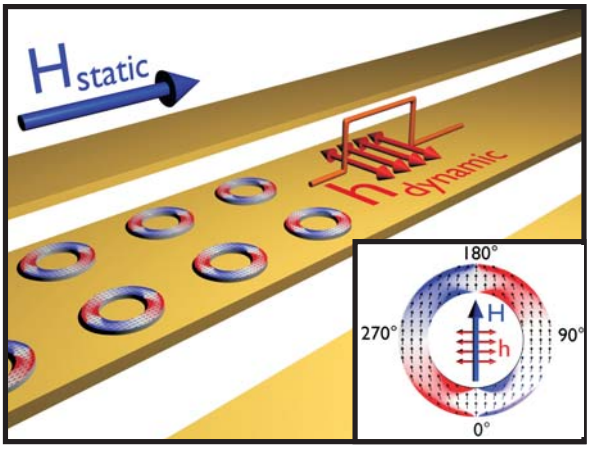

Fig. 1: Magnetic ring structures with a thickness of 30 nm, an outer diameter of $D = 2\,\mu$m and a ring width of $w = 400$ nm are placed on top of a coplanar waveguide made out of Au with a central strip line width of 20 µm and thickness of 200 nm. A static field H_{static} of 330 Oe is applied in the sample plane and perpendicular to the strip line. The inset shows a micromagnetic simulation of the so called onion state of the magnetization. For the particular geometry and applied field transverse domain walls are present at 0° and 180° leading to a strong reduction of the total internal field. In both regions, the poles at 0° and 180°, and the equator at 90° and 270°, the coupling of the dynamic magnetic field $h_{dynamic}$ caused by a microwave current flowing through the coplanar waveguide is most efficient.

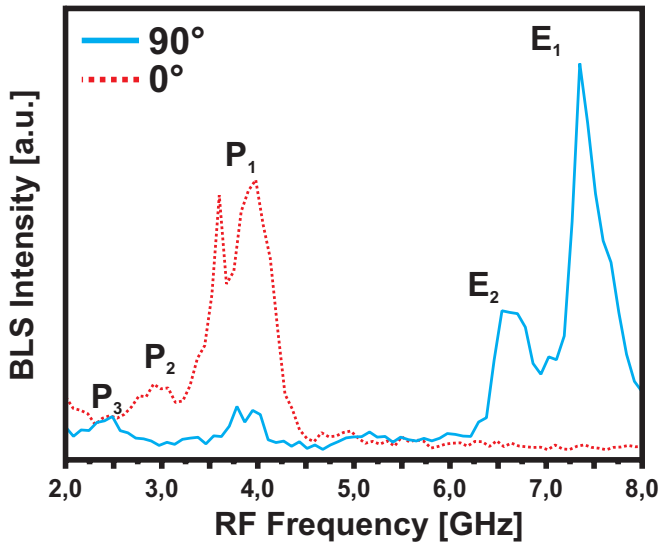

Fig. 2: Spin-wave amplitudes measured with BLS microscopy under the application of a dynamic magnetic field in the plane of the sample caused by a microwave current flowing through the central conductor of the coplanar waveguide. The spectra were acquired in the pole region at 0°, dotted line, and in the equatorial region at 90°, solid line. Five resonances are found, three (P_3=2.5 GHz, P_2=2.9 GHz, P_1=3.9 GHz) located at the pole and two (E_1=6.6 GHz, E_2=7.3 GHz) at the equator.

For a deeper understanding it is of central interest to study the mode dynamics, in particular how fast a mode is relaxing after resonant excitation with a short microwave puls and to identify the channels of dissipation. Since the coupling is weak and can be discussed in a perturbation picture, we address the mode spectrum in the following as the “quasi-eigenmode” spectrum.

Here we report on the investigation of the lifetime of quantized spin waves in a small magnetic ring structure magnetized in the so-called onion state using time-resolved Brillouin light scattering microscopy. For this purpose, permalloy ($Ni_{81}Fe_{19}$) rings with an outer diameter of $D = 2\,\mu m$, a ring width of $w = 400\,nm$, and a thickness of 30 nm were prepared by a combination of molecular beam epitaxy in an UHV system and electron beam lithography, utilizing a lift-off technique. The ring structures are placed on top of a coplanar waveguide as shown schematically in Fig. 1. The waveguide is made out of a 200 nm Au layer and the central strip line has a width of 20 µm, small enough to ensure high excitation fields in the region where the ring structures are placed. The ring to ring spacing was chosen twice the ring diameter to avoid magneto-static and dynamic coupling between neighbouring rings. The geometry of the dynamic and static magnetic fields used in these experiments is illustrated in Fig. 1: a static magnetic field H_{static} of 330 Oe is applied along the direction of the central strip line to induce the onion state of the magnetization. In this case the magnetization is aligned mainly parallel to the axis of the central strip line of the coplanar waveguide and, therefore, the efficiency of the excitation with the dynamic magnetic field $h_{dynamic}$ is optimal.

In order to determine the quasi-eigenmode frequencies in the pole and equatorial regions of the onion state we performed FMR-BLS measurements at 0° and 90°. A microwave current with frequencies between 2 GHz and 8 GHz was sent through the coplanar waveguide to excite the magnetization. The precession amplitude is measured locally by means of BLS microscopy with a spatial resolution of 250 nm. A detailed discussion of this technique can be found in [14, 15]. The results are shown in Fig. 2 where the BLS intensity is plotted as a function of the applied microwave frequency for the pole position at 0° (dotted line) and the equator position at 90° (solid line). Two very strong resonances can be observed at 90°: E_1=7.3 GHz and E_2=6.6 GHz. Two weaker resonances P_3=2.5 GHz and P_1=3.9 GHz with their origin in the pole region, as dicussed in the text below, contribute to the BLS intensity measured at 90°. The measurement at 0° reveals again P_1 and in addition a resonance P_2 at 2.9 GHz.

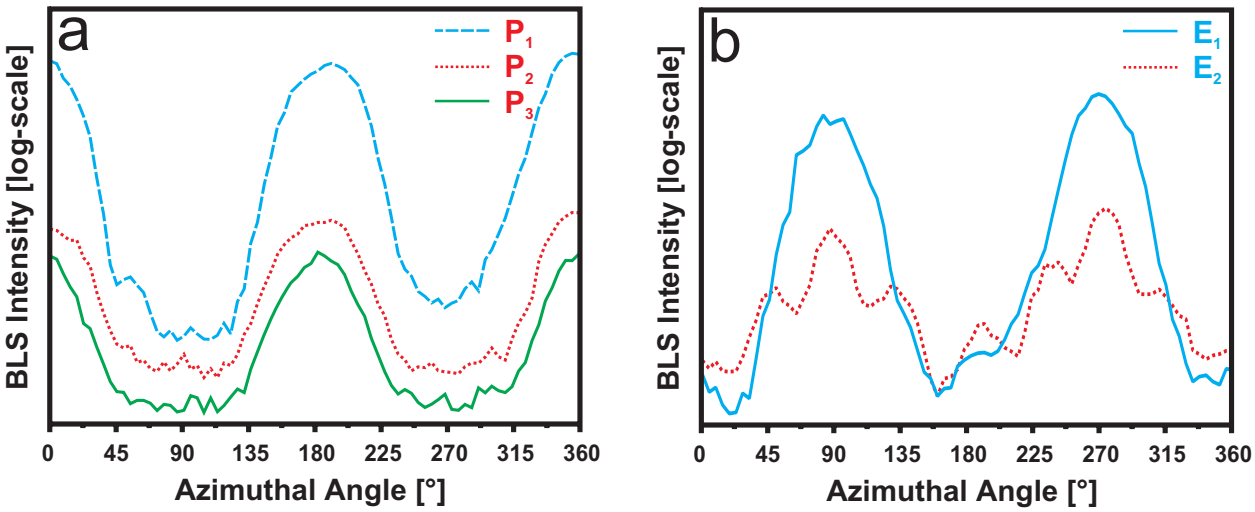

Fig. 3: Spatial distribution of the spin waves resonantly excited in the magnetic ring structure. (a) The spin-wave amplitudes under excitation with the frequencies P_1, P_2, and P_3 of the quasi-eigenmodes found in Fig. 2 are plotted as a function of the position. For clarity the spectra are vertically shifted against each other. A strong confinement of the low frequency modes in the poles of a ring magnetized in the onion state is clearly visible. (b) Spin waves located near the equator regions of the magnetic ring structure under excitation with the frequencies E_1 and E_2 . The quasi-eigenmode with the highest frequency E_1=7.3 GHz has its maximum amplitude at 90°. The next quasi-eigenmode E_2=6.6 GHz at the equator shows two nodes in azimuthal direction.

For a better understanding of the nature of all the observed resonances we performed BLS measurements as a function of the azimuthal angle while exciting the magnetization with the resonance frequencies shown in Fig. 2. The spatial distributions of the low frequency spin-wave modes P_1, P_2, and P_3 are displayed in Fig. 3a where the BLS intensity is plotted as a function of the azimuthal angle. All three modes P_1, P_2, and P_3, observed in Fig. 2, are strongly confined in the poles of the onion state, as expected from previous works [8–10]. The modes E_1 and E_2 with higher frequencies are located in the equatorial region at 90° and 270° as can be seen in Fig. 3b. The quasi-eigenmode E_1 at 7.3 GHz shows one maximum, and the quasi-eigenmode E_2 at 6.6 GHz shows three maxima in each half of the ring. The fact that higher azimuthal quasi-eigenmodes in rings and disks have lower frequencies due to their backward volume mode character is well known and was reported previously [9, 16].

After the determination of the spin-wave frequencies, which can be resonantly excited with an in-plane magnetic microwave field, and the positions of maximum spin-wave amplitudes, the investigation of the temporal evolution of the observed quasi-eigenmodes has been addressed. Therefore, the sample is now excited with microwave pulses with a duration of 50 ns and a repetition period of 128 ns. The rising edge of the pulse starts a counter with a time resolution of 250 ps. From this time on, the arrival time of each inelastically scattered photon is registered together with its frequency – similar to the experiment described in [15]. The full spectral, spatial and temporal information of the investigated spin-wave modes is now accessible.

Figure 4a shows the temporal profile of the spin-wave quasi-eigenmodes P_1, P_2, and P_3 in the pole region of the onion state. The time in which the microwave pulse is applied is indicated in the bottom of the figure. The spin-wave intensities increase drastically within the first few nanoseconds when the pulse arrives and starts to decay when the pulse terminates. The intensities of all three measurements are normalized to the intensity at the time when the excitation pulse terminates in order to emphasize the difference in the relaxation part of the temporal profile. A multiplication

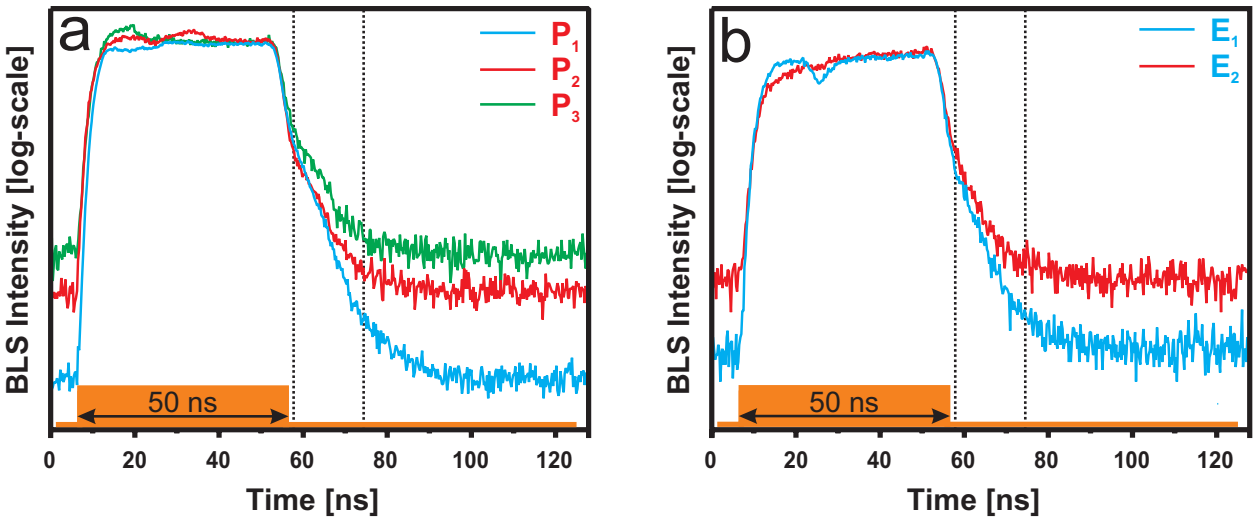

Fig. 4: Temporal evolution of the quasi-eigenmodes of the ring structure under the resonant excitation with a microwave pulse with a duration of 50 ns. The intensity of all temporal profiles is normalized at the time where the excitation pulse terminates. (a) Pole region: The upper curve displays the lowest frequency mode P_3=2.5 GHz and the lowest curve corresponds to the quasi-eigenmode P_1=3.9 GHz. In between the vertical, dashed lines an exponential decay of the quasi-eigenmode amplitudes can be observed with different decay constants for each mode. (b) Equator region: The lower curve displays the behavior of the quasi-eigenmode E_1=7.3 GHz, the upper curve corresponds to the quasi-eigenmode E_2=6.6 GHz

with a constant factor does not change the slope of an exponential decay in a logarithmic plot but it supports the comparison of the decay of the different spin-wave quasi-eigenmodes. It can be seen in the time window between the two vertical dashed lines in Fig. 4 that the decay constant τ, if one assumes an exponential decay $\exp(-\frac{t}{\tau})$, differs for each frequency. The higher the spin-wave frequency is the faster is the relaxation, i.e. the smaller is the decay constant τ. The same qualitative behavior is observed for the spin waves in the equatorial region, see Fig. 4b. The first azimuthal mode with the higher frequency shows a faster relaxation than the third azimuthal mode with lower frequency.

The decay constants for all investigated spin-wave quasi-eigenmodes are summarized in Fig. 5. Here it is evident that the decay constant is decreasing with increasing frequency for the same type of spin waves, but there is a general difference when the character of the spin-wave quasi-eigenmode, i.e. the wavevector and the quantization condition, is changed. We find - despite the fact that the frequencies of the spin waves are much higher in the equatorial region - that the relaxation times are comparable to the relaxation times at the poles of the onion state. Several mechanisms contribute to the dissipation of spin-wave quasi-eigenmodes, for example coupling to the lattice, i.e. magnon-phonon-scattering, and coupling within the spin-wave quasi-eigenmode system, i.e. magnon-magnon-scattering. The first mechanism depends on the magneto-elastic constants of the used material and is, therefore, independent of the lateral position on the ring. The efficiency of energy transfer in the latter mechanism strongly depends on the total internal field, the magnetization distribution within the quantization volume and, since energy conservation has to be fulfilled in the magnon-magnon-scattering process, on the frequencies of the participating spin waves. Hence, a position dependency of the dissipation processes, as we observe it in the ring structure, is obvious and can explain that the decay constants τ are nearly the same at the equator as in the poles - even if the frequencies of the measured spin waves are much higher.

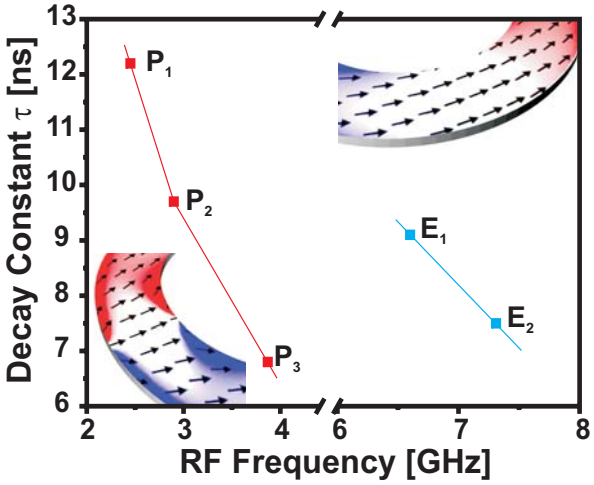

Fig. 5: Decay constants τ for all investigated quasi-eigenmodes as a function of the excitation frequency. In the left part of the figure τ is plotted for the low frequency spin waves confined in the pole region 0° of the onion state. The right part shows τ of the spin waves at the equatorial region 90°. The decay constant is extracted out of the temporal profiles in Fig. 4 in the time windows indicated by the dashed vertical lines where the influence of the microwave pulse is negligible.

In conclusion we have determined the decay constants of all spin wave modes that can be excited with in-plane microwave pulses in a small magnetic $Ni_{81}Fe_{19}$ ring using time-resolved BLS microscopy. Low frequency excitations were observed in the poles of the onion state whereas the spin waves detected at the equatorial position have higher frequencies and were identified as the well-known azimuthal modes of the onion state. The decay constants were extracted from the temporal evolution of the spin wave amplitudes after the end of the exciting microwave pulse. A decrease of the decay constant, i.e. a shorter lifetime of the spin-wave quasi-eigenmodes, was found when the frequency of the quasi-eigenmode is higher. The comparison of the dissipation time of the quasi-eigenmodes confined at the pole and the equatorial region of the onion state is indicating that different dissipation mechanisms are responsible for the relaxation of the magnetization, depending on the position and the quantization conditions of the spin-wave quasi-eigenmodes.

Support by the Priority Program SPP 1133 of the Deutsche Forschungsgemeinschaft and the NEDO International Joint Research Program 2004IT093, Japan, is gratefully acknowledged. The authors acknowledge S. Trellenkamp and S. Wolff from the Nano + Bio Center, University of Kaiserslautern, for technical support.

References

[1] C. Mathieu, J. Jorzick, A. Frank, S.O. Demokritov, A.N. Slavin, B. Hillebrands, B. Bartenlian, C. Chappert, D. Decanini, F. Rousseaux, E. Cambril, Phys. Rev. Lett. **81**, 3968 (1998).
[2] J. Jorzick, S.O. Demokritov, B. Hillebrands, M. Bailleul, C. Fermon, K.Y. Guslienko, A.N. Slavin, D.V. Berkov, N.L. Gorn, Phys. Rev. Lett. **88**, 047204 (2002).
[3] M. Bailleul, D. Olligs, C. Fermon, Phys. Rev. Lett. **91**, 137204 (2003).
[4] S.O. Demokritov, B. Hillebrands, A.N. Slavin, Physics Reports **348**, 441 (2001).
[5] G. Gubbiotti, M. Conti, G. Carlotti, P. Candeloro, E. Di Fabrizio, K.Y. Guslienko, A. Andre, C. Bayer, A.N. Slavin, J Phys-Condens Mat **16**, 7709 (2004).
[6] G. Gubbiotti, G. Carlotti, T. Okuno, M. Grimsditch, L. Giovannini, F. Montoncello, F. Nizzoli, Phys Rev B **72**, 184419 (2005).
[7] G. Gubbiotti, G. Carlotti, T. Okuno, T. Shinjo, F. Nizzoli, R. Zivieri, Phys. Rev. B **68**, 184409 (2003).
[8] H. Schultheiss, S. Schäfer, P. Candeloro , B. Leven, B. Hillebrands, A.N. Slavin, Phys. Rev. Lett. **100**, 047204 (2008).
[9] I. Neudecker, M. Klaui, K. Perzlmaier, D. Backes, L.J. Heyderman, C.A.F. Vaz, J.A.C. Bland, U. Rüdiger, C.H. Back, Phys. Rev. Lett. **96**, 057207 (2006).
[10] G. Gubbiotti, M. Madami, S. Tacchi, G. Carlotti, H. Tanigawa, T. Ono, L. Giovannini, F. Montoncello, F. Nizzoli, Phys. Rev. Lett. **97**, 247203 (2006).

[11] Xiaobin Zhu, Zhigang Liu, Vitali Metlushko, L. Giovannini, F. Montoncello, F. Nizzoli, M.R. Freeman, J. Appl. Phys. **99**, 105 (2006).
[12] F. Giesen, J. Podbielski, T. Korn, M. Steiner, A. van Staa, D. Grundler, Appl. Phys. Lett. **86**, 112510 (2005).
[13] F. Giesen, J. Podbielski, T. Korn, D. Grundler, J. Appl. Phys. **97**, 10A712 (2005).
[14] K. Perzlmaier, M. Buess, C.H. Back, V.E. Demidov, B. Hillebrands, S.O. Demokritov, Phys. Rev. Lett. **94**, 057202 (2005).
[15] V.E. Demidov, S.O. Demokritov, B. Hillebrands, M. Laufenberg, P.P. Freitas, Appl. Phys. Lett. **85**, 2866 (2004).
[16] M. Buess, T.P.J. Knowles, R. Hällinger, T. Haug, U. Krey, D. Weiss, D. Pescia, M.R. Scheinfein, C.H. Back, Phys. Rev. B. **71**, 104415 (2005).
[17] S.O. Demokritov, V.E. Demidov, O. Dzyapko, G.A. Melkov, A.A. Serga, B. Hillebrands, A.N. Slavin, Nature **443**, 430 (2006).

6.4 Modification of the thermal spin wave spectrum in a $Ni_{81}Fe_{19}$ stripe by a domain wall

S.J. Hermsdörfer, C.W. Sandweg, H. Schultheiss, S. Schäfer, P.A. Beck, B. Leven, and B. Hillebrands

The research field of spin waves in confined magnetic structures with controlled inhomogeneous internal field is of fundamental interest for understanding magnetization dynamics (see e.g. [1–3]). Such an inhomogeneous internal field can be caused by the finite size of the magnetic object due to stray field effects at the boundaries [1,4–6] and/or by a magnetic domain structure [3,7–9]. Several investigations of spin-wave spectra in finite elements without and with domain structure have been reported (see e.g. References [9–31]). Here, we report on the modification of the thermal spin-wave distribution by a domain wall. As one main result we report the finding of a spin-wave mode localized to a domain wall region. It is caused by a spin-wave potential well generated by the domain wall. To approach the problem, two main obstacles have to be overcome: firstly and most importantly, a non-destructive measurement technique capable to resolve the dynamic properties with high spatial resolution for resolving the domain pattern is needed. Secondly, domain walls must be created in a reliable and reproducible way.

The structure design of curved wires follows an idea presented by Saitoh [32] and has also been discussed in [33] as the so-called domain wall pendulum. A semi-circular $Ni_{81}Fe_{19}$ structure contains a circular anti-notch located at the pole of the semi-circle acting as a pinning site for the domain wall (see Fig. 1). In particular, the chosen semi-circular sample design allows for a defined nucleation and annihilation of a single domain wall in the vicinity of the anti-notch by applying a magnetic field in transversal or parallel direction, respectively, and subsequent relaxation of the magnetization to remanence.

The samples have been produced using a combination of molecular beam epitaxy and electron beam lithography employing a standard lift-off process. The $Ni_{81}Fe_{19}$ films have a thickness of 10 nm. The $Ni_{81}Fe_{19}$ structures have been prepared using a 120 nm thick PMMA resist layer (polymethylmethacrylate, molecular weight 950 K, solid fraction of 4 %) spun onto a thermally oxidized silicon substrate (500 µm silicon covered with 100 nm silicon oxide). The radii of the structures vary between 5 µm and 50 µm in steps of 5 µm. The wire width is 500 nm and the radius of the anti-notch is 250 nm revealing a total width of 750 nm at the anti-notch position. The patterned structures show a small growth-induced transverse anisotropy. A schematic view of one of the semi-circles is shown in Fig. 1a. Here, the $Ni_{81}Fe_{19}$ structure is displayed in dark color. The bright spots indicate the data acquisition positions. The magnetic field directions used to nucleate a domain wall or to saturate the sample are also defined in Fig. 1a. Fig. 1b shows a scanning electron micrograph of the sample design.

For analyzing the spin-wave modes Brillouin light scattering microscopy (hereafter referred to as BLS microscopy) was employed and BLS investigations were carried out exemplarily for the semi-circle with a radius of 5 µm. For magnetostatic domain analysis and dynamic spin-wave distribution analysis OOMMF [35] simulations are presented to support the interpretation of the experimental results.

An essential prerequisite is a well characterized domain wall, that is reproducibly induced and located near the anti-notch. Since BLS microscopy does not allow for direct in-situ domain imaging, the domain analysis experiments have been made in collaboration with the group of Prof John

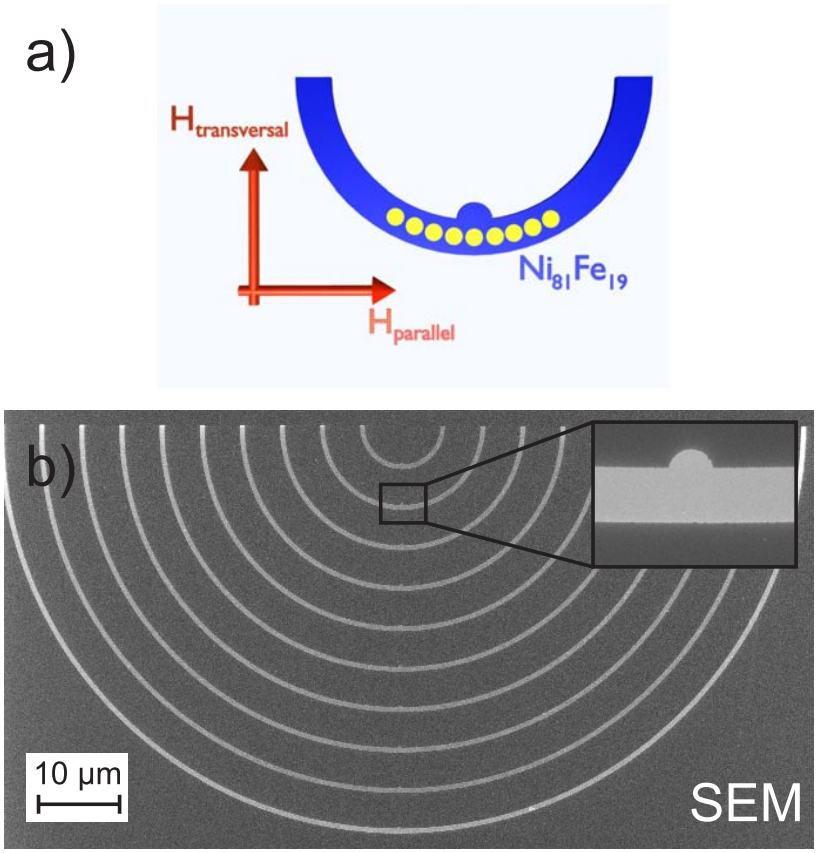

Fig. 1: a) Schematic view of the sample design and data acquisition procedure. Measurements have been carried out along the positions marked by the bright spots. The externally applied magnetic fields are shown as $H_{\text{transversal}}$ and H_{parallel}. b) Scanning electron micrograph of the $Ni_{81}Fe_{19}$ semi-circles each comprising an anti-notch as domain wall pinning site.

Chapman, Glasgow University, using Lorentz microscopy. The results are reported in [34]. In summary: employing standard electron transparent Si_3N_4/Si substrates the domain structure of the $Ni_{81}Fe_{19}$ wires was investigated. It was found that the domain wall induced in the semi-circular structures by applying a defined field sequence exhibit the character of an asymmetric transverse domain wall and can reproducibly be located close to the position of the anti-notch.

To analyze the spin-wave modes present in the $Ni_{81}Fe_{19}$ curved nanowires the spectra of thermally activated spin waves have been investigated. The measured BLS spectra are summarized in a color coded intensity map, where dark colors represent the lowest spin-wave intensity and bright colors the highest intensity. Each vertical line in the color map represents a BLS spectrum taken at the position indicated at the x-axis. The spectra have been taken with a step size of 0.1 µm equidistantly along the central perimeter of 6.1 µm in length in the vicinity of the anti-notch (see Fig. 1a). First, the sample was initialized in *parallel* direction by saturating the sample in a field H_{parallel}= 880 Oe, thus ensuring that no residual domain walls were present. Subsequently the sample was relaxed to remanence. Fig. 2a shows the resulting BLS color map and the corresponding magnetization distribution obtained by OOMMF simulations [35]. For the numerical simulations, the semi-ring with the corresponding radius (inner radius 5 µm, outer radius 5.5 µm) has been simulated. To optimize computation time, only a section of 5.8 µm by 1.4 µm with a thickness of 10 nm was taken into account. The mesh size was 7.5 nm × 7.5 nm × 10 nm and the standard values for $Ni_{81}Fe_{19}$ (exchange stiffness constant A=1.6·10^{-6} erg/cm, gyromagnetic ratio γ=1,76×10^{-2} GHz/Oe, and a

damping constant α=0.01) have been used. A saturation magnetization of only 650 G instead of 860 G has been chosen to take account of a heating effect of the sample by the laser spot during data acquisition [9].

In this remanence case *without* a domain wall two modes of standing spin waves with frequencies of about 2.4 and 3.4 GHz can be clearly identified. These modes exhibit mainly the characteristics of magnetostatic surface waves, the so-called Damon-Eshbach modes, whose direction of propagation is in-plane perpendicular to the magnetization of the structure. They are quantized in transversal direction due to the lateral confinement of the structure and travel forth and back between the stripe boundaries. In this regard no influence of the changing geometric boundary conditions due to the anti-notch is evident in the BLS-spectra.

Next, the change of the thermal spin-wave spectrum due to the presence of the asymmetric transverse domain wall has been analyzed. To do so, the sample has been initialized by applying an external magnetic field in *transversal* direction (see Fig. 1a). After removal of the field an asymmetric transverse domain wall is nucleated in the structure and pinned in the vicinity of the anti-notch [34]. The corresponding BLS intensity map as well as the according magnetization distributions obtained by OOMMF-simulations [35] are shown in Fig. 2b.

By comparing the intensity maps obtained with and without a domain wall, obvious differences in the spectra can be identified: instead of the original modes observed outside the domain wall with frequencies of 2.4 and 3.4 GHz a new mode with a frequency of about 4.8 GHz arises at the position of the anti-notch whereas the other modes vanish in this area (see Fig. 2b).

This behavior can be understood in terms of a change in magnitude and direction of the effective local internal magnetic field $\mathbf{h}_{\mathrm{eff}}$ [5]. Such a local change in the magnetic field caused by the asymmetric transverse domain wall can act as a spin-wave potential well supporting a localized mode [9]. Due to the two-dimensional character of this problem an analytical approach to calculate the mode frequency is impractical - instead dynamical micromagnetic simulations have been

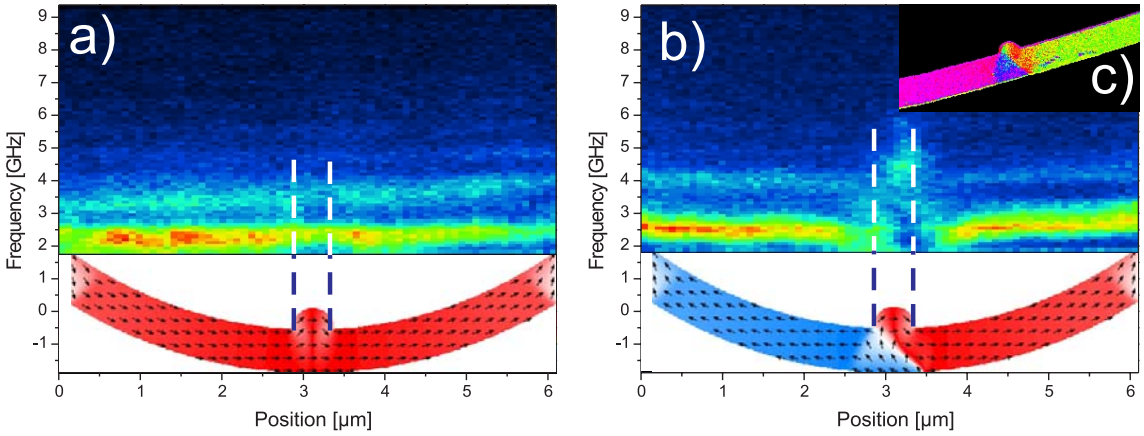

Fig. 2: Intensity map summarizing the spectra of thermally activated spin waves in the semi-circular $Ni_{81}Fe_{19}$ structure of radius 5 µm without an applied external field a) in the absence of domain walls, b) in the presence of a domain wall. The BLS intensity is shown color coded ranging from dark colors (low intensity) to bright colors (high intensity). Each vertical line in the two-dimensional map represents a BLS spectrum taken at the position as indicated on the x-axis. The white dashed lines show the position of the anti-notch. Insets: Corresponding magnetization distributions obtained by OOMMF-simulations. c) Color vector map of the magnetic induction obtained by Lorentz microscopy in cooperation with the group of Prof John Chapman, University of Glasgow [34].

carried out for direct comparison.

The dynamic simulations have been performed by applying a weak out-of-plane Gaussian-shaped magnetic field pulse (amplitude 1 Oe, pulse width 20 ps) to the semi-circle at remanence and, thus, excite the eigenmode spectrum of the magnetic element. These data have been Fourier-transformed point by point to the frequency domain to obtain the spin-wave mode distribution. In comparison to the experiments the simulations show a slight frequency shift as the first mode can be observed at 3.3 GHz whereas in the experiment the frequency of the first mode is 2.4 GHz. This can be observed as well for the second mode which appears in the experiment at 4 GHz and in the simulations at 4.7 GHz. This difference can be understood by a difference between the sample properties and the parameters of the simulation, e.g. possible variations of the effective stripe width of the sample caused by fabrication defects which are not taken into account in the simulation.

In general, the experiment and the simulation show a very good qualitative agreement. Figure 3a-c show the simulated mode distribution of the three modes in the structure exhibiting the transverse domain wall in remanence. In Fig. 3a the first mode without a node can be observed along the whole semi-circle perimeter, suppressed only in the area of the domain wall. The second mode shown in Fig. 3b shows the typical node in the middle of the stripe due to quantization of the spin waves in radial direction. For both modes a clear disturbance is observed in the region of the domain wall. Fig. 3c shows a weakly excited mode at higher frequencies, which is mainly localized in the area of the anti-notch, where the domain wall is pinned. This mode corresponds to the experimentally observed mode localized in the domain wall (see Fig. 2b). For comparison, the simulations have been carried out for the same structure and at remanence but without a domain wall, i.e. in an uniformly magnetized semi-circle (see Fig. 2a). The results are shown in Fig. 3d and e) for the corresponding frequencies. In this configuration no major change in the mode structure in the vicinity of the anti-notch can be observed. This result proofs that the pinned domain wall is the reason for the changes in the mode structure.

To further analyze this new mode localized in the vicinity of the domain wall the behavior of the

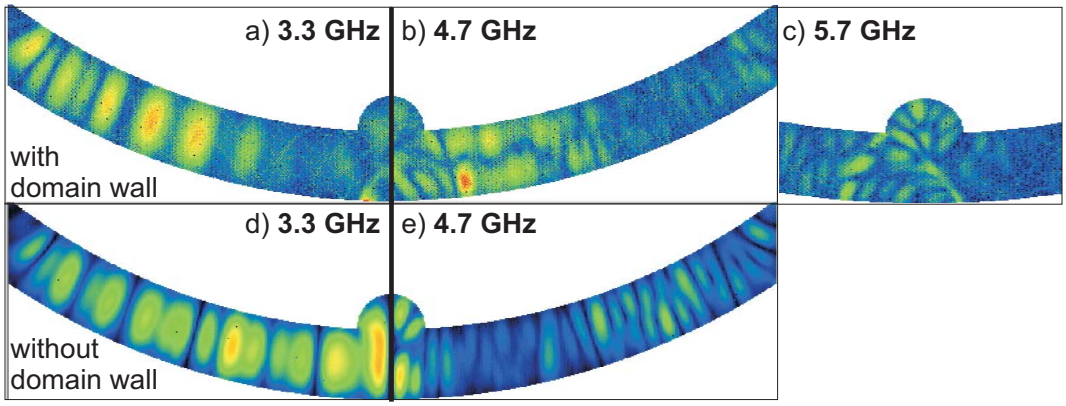

Fig. 3: Spatially resolved Fourier-transformed spin-wave mode distributions obtained by micromagnetic simulations for a frequency of a 3.3 GHz, b 4.7 GHz, and c) 5.7 GHz at remanence. Panel a) shows the first mode along the semi-circle perimeter in the presence of a domain wall. In Panel b) the node due to the quantization in radial direction can be clearly seen. Both mode profiles are strongly disturbed in the region of the anti-notch, where the domain wall is localized. Panel c) shows the weakly excited mode in the area of the anti-notch for high frequencies. Panels d) and e) show the results of the simulation in the absence of a domain wall but at the same frequencies as before. It can be seen that the mode structure does not change significantly in the vicinity of the anti-notch.

spin-wave modes under the influence of an increasing *transversal* as well as an increasing *parallel* magnetic field was investigated. First, the domain wall growth and annihilation expected for an increasing *transversal* magnetic field is discussed. During this procedure the domain wall width is increasing. For a better comparison between the intensity maps at different fields, only the relevant BLS frequencies between 2 to 6 GHz are shown in Fig. 4. Additionally, the results of the corresponding micromagnetic simulations are added for selected fields. As can be seen from the BLS intensity maps and comparison with the micromagnetic simulations, the new mode inside the domain wall is pronounced as long as the asymmetric transverse domain wall exists. The mode starts to vanish when the domain wall width is increasing due to the externally applied transversal field. The asymmetric transverse domain wall loses its character at 109 Oe. For further increase of the transversal field the magnetization follows the external field even in the area of the anti-notch. These results are in agreement with the Lorentz microscopy investigations presented in [34].

Second, the spin-wave distribution with increasing *parallel* magnetic field was investigated. In this measurement geometry the asymmetric transverse domain wall is expected to extend and depin from the pinning site, as has been demonstrated in [34]. This time the domain wall was initialized as before but the sample was rotated afterwards by 90 ° and a parallel, slightly increasing field has

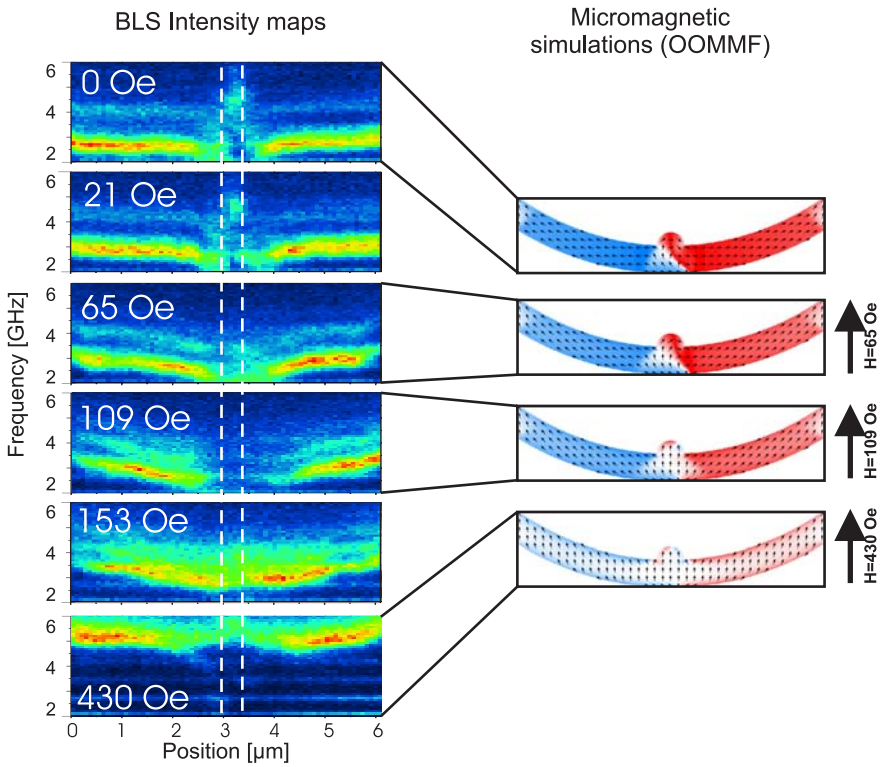

Fig. 4: Experimental intensity map summarizing the spectra of thermally activated spin waves in the semi-circular $Ni_{81}Fe_{19}$ structure of radius 5 µm while applying a transversal field ranging from 0 Oe to 430 Oe. The BLS intensity is shown color coded ranging from dark colors (low intensity) to bright colors (high intensity). Each vertical line in the two-dimensional map represents a BLS spectrum taken at the position as indicated on the *x*-axis. The white dashed lines show the position of the anti-notch. Right side: Corresponding magnetization distributions obtained by OOMMF-simulations. The intensity maps show the disappearance of the original modes at the position of the anti-notch and the appearing new mode in this area. With increasing fields, the modes shift to higher frequencies and the domain wall is broadening. In the last maps, which correspond to high field values, the domain wall vanished and only the effect of the increased stripe width at the position of the anti-notch on the mode frequency can be observed.

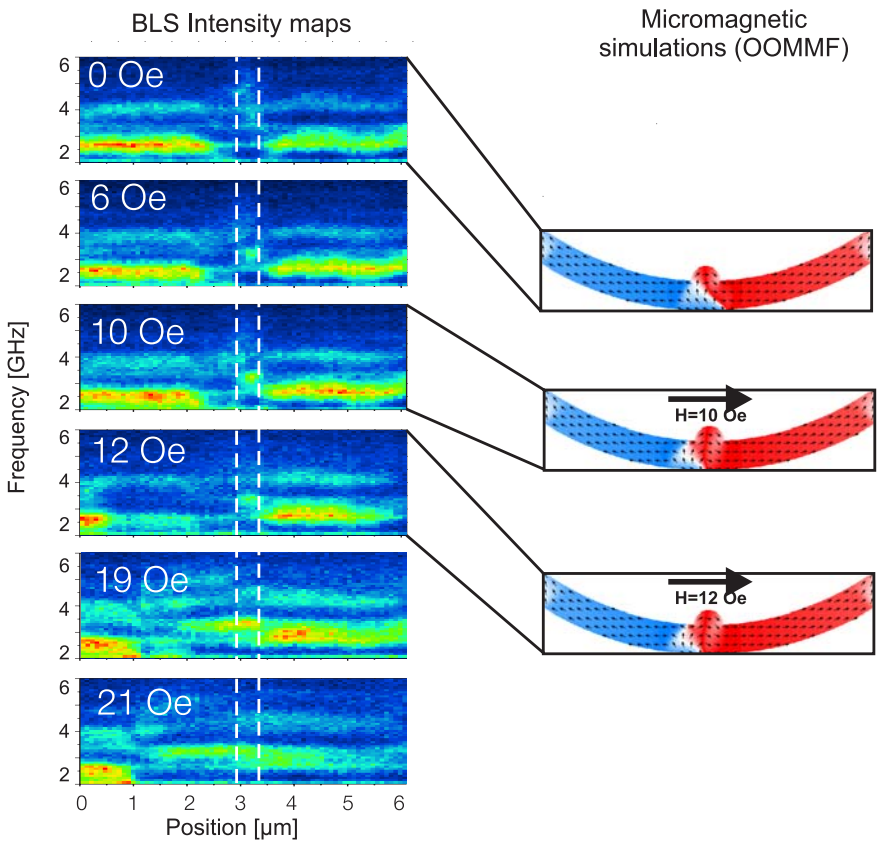

Fig. 5: BLS intensity maps summarizing the spectra of thermally activated spin waves in the semi-circular $Ni_{81}Fe_{19}$ structure of radius 5 µm for different applied parallel fields. For this measurement the domain wall has been nucleated by applying a transversal field and relaxation to remanence, afterwards the sample has been rotated by 90 ° and a parallel field has been applied. Right side: Corresponding magnetization distributions obtained by OOMMF-simulations. The field driven displacement of the domain wall can be seen from the intensity maps as a change in the mode spectrum.

been applied. The results as well as corresponding micromagnetic simulations are presented in Figure 5.

As can be seen from the simulations, the domain wall is depinned already at a field of 10 Oe and driven to the left by the external field. This change in the magnetization distribution can also be observed in the BLS intensity maps. As long as the domain wall is pinned in the vicinity of the anti-notch the eigenmode spectrum with the first mode at 2.5 GHz on the left hand side does not show a significant change. As soon as the domain wall is depinned and starts to move in this direction, the modes existing only outside the domain wall vanish at the position of the wall which can clearly be seen starting from 12 Oe. Consequently, the domain wall displacement also causes a change of the spin-wave mode profile in the area of the anti-notch, as the domain wall is not longer localized at this position. The mode localized in the domain wall disappears at this position as the domain wall moves and the spin-wave mode profile existing in the semi-circle perimeter evolves. Thus, the spin-wave mode localized in the domain wall enables the observation of domain wall displacement by BLS microscopy. These results are in excellent agreement with [34] where the movement of such a domain wall in the same structure has been observed by means of Lorentz microscopy.

Summarizing our results, this article reports on the analysis of the thermal spin-wave mode dis-

tribution in $Ni_{81}Fe_{19}$ semi-circles with defined asymmetric transverse domain walls employing Brillouin light scattering microscopy. The spectra of thermally excited spin waves reveal a clear influence of the presence of the domain wall, which is nucleated and pinned in the vicinity of the anti-notch of the structure. Comparing the spin-wave spectra in the absence and presence of the domain wall it can be observed that the original spin-wave modes quantized in radial direction vanish in the vicinity of the domain wall and new modes are formed located only inside this complex domain wall structure. The experimental results are confirmed by static and dynamic OOMMF simulations. Investigating the field dependence of these new modes it could be proven that the domain wall growth and destruction in a transversal applied field as well as the depinning behavior in a parallel applied field can be monitored by BLS microscopy employing the spatially resolved detection of the mode localized in the domain wall structure.

The authors thank the Nano+Bio Center (Sandra Wolff, Bert Lägel, and Christian Dautermann) of the University of Kaiserslautern for technical support during the sample processing. Financial Support by the DFG within the Priority Programme 1133 “Ultrafast magnetization processes” is gratefully acknowledged.

References

[1] S.O. Demokritov, A.A. Serga, A. Andre, V.E. Demidov, M.P. Kostylev, B. Hillebrands and A.N. Slavin, Phys. Rev. Lett. **93**, 047201 (2006).
[2] S. Tamaru, J.A. Bain, R.J.M. van de Veerdonk, T.M. Crawford, M. Covington, and M.H. Kryder, Phys. Rev. B **70**, 104416 (2004).
[3] T.M. Crawford, M. Covington, and G.J. Parker, Phys. Rev. B **67**, 024411 (2003).
[4] M.P. Kostylev, A.A. Serga, T. Schneider, T. Neumann, B. Leven, B. Hillebrands and R.L. Stamps, Phys. Rev. B **76**, 184419 (2007).
[5] C. Bayer, H. Schultheiss, B. Hillebrands and R.L. Stamps, IEEE Trans. Magn. **41**, 3094 (2005).
[6] Y. Roussigne, S.M. Cherif, C. Dugautier, and P. Moch, Phys. Rev. B **63**, 134429 (2001).
[7] M. Bailleul, R. Höllinger, K. Perzlmaier, and C. Fermon, Phys. Rev. B **76**, 224401 (2007).
[8] M. Bailleul, R. Höllinger, and C. Fermon, Phys. Rev. B **73**, 104424 (2006).
[9] H. Schultheiss, S. Schäfer, P. Candeloro, B. Leven, B. Hillebrands and A.N. Slavin, Phys. Rev. Lett. **100**(4), 047204 (2008).
[10] Y. Ando, Y.M. Lee, T. Aoki, T. Miyazaki, H. Schultheiss and B. Hillebrands, J. Magn. Magn. Mater. **310**(2), 1949 (2007).
[11] V.E. Demidov, S.O. Demokritov, B. Hillebrands, M. Laufenberg and P.P. Freitas, J. Appl. Phys. **97**, 10A717 (2005).
[12] S.O. Demokritov, B. Hillebrands and M. Laufenberg, Appl. Phys. Lett. **85**, 2866 (2004).
[13] A. Barman, V.V. Kruglyak, R.J. Hicken, J.M. Rowe, A. Kundrotaite, A. Scott, and M. Rahman, Phys. Rev. B **69**, 174426) (2004).
[14] Y.S. Gui, N. Mecking, and C.-M. Hu, Phys. Rev. Lett. **98**, 217603 (2007).
[15] M.P. Kostylev, G. Gubbiotti, J.-G. Hu, G. Carlotti, T. Ono, and R.L. Stamps, Phys. Rev. B **76**, 054422 (2007).
[16] Z. Liu, F. Giesen, X. Zhu, R.D. Sydora, and M.R. Freeman, Phys. Rev. Lett. **98**, 087201 (2007).
[17] M. Buess, J. Raabe, K. Perzlmaier, C.H. Back, and C. Quitmann, Phys. Rev. B **74**, 100404(R) (2006).
[18] J. Podbielski, F. Giesen, and D. Grundler, Phys. Rev. Lett. **96**, 167207 (2006).
[19] I. Neudecker, M. Kläui, K. Perzlmaier, D. Backes, L.J. Heyderman, C.A.F. Vaz, J.A.C. Bland, U. Rüdiger, and C.H. Back, Phys. Rev. Lett. **96**, 057207 (2006).
[20] C.H. Back, D. Pescia, and M. Buess, *Top. Appl. Phys.* **101**, 137 (2006).
[21] K. Perzlmaier, M. Buess, C.H. Back, V.E. Demidov, B. Hillebrands and S.O. Demokritov, Phys. Rev. Lett. **94**, 057202 (2005).
[22] J.P. Park and P.A. Crowell, Phys. Rev. Lett. **95** 167201 (2005).
[23] G. Gubbiotti, G. Carlotti, T. Okuno, M. Grimsditch, L. Giovannini, F. Montoncello, and F. Nizzoli, Phys. Rev. B **72**, 184419 (2005).
[24] C. Bayer, J. Jorzick, B. Hillebrands, S.O. Demokritov, R. Kouba, R. Bozinoski, A.N. Slavin , K. Guslienko, D. Berkov, N. Gorn and M.P. Kostylev, Phys. Rev. B **72**, 064427 (2005).
[25] V.V. Kruglyak, A. Barman, R.J. Hicken, J.R. Childress, and J.A. Katine, Phys. Rev. B **71**, 220409 (2005).

[26] R. Hertel, W. Wulfhekel, and J. Kirschner J, Phys. Rev. Lett. **93**, 257202 (2004).
[27] M. Belov, Z. Liu, R.D. Sydora, and M.R. Freeman, Phys. Rev. B **69**, 094414 (2004).
[28] C. Bayer, J.P. Park, H. Wang, M. Yan, C.E. Campbell, and P.A. Crowell, Phys. Rev. B **69**, 134401 (2004).
[29] G. Gubbiotti, G. Carlotti, T. Okuno, T. Shinjo, F. Nizzoli, and R. Zivieri, Phys. Rev. B **68**, 184409 (2003).
[30] K.Y. Guslienko, R.W. Chantrell, and A .N. Slavin, Phys. Rev. B **68**, 024422 (2003).
[31] M. Bailleul, D. Olligs, and C. Fermon, Phys. Rev. B **91**, 137204 (2003).
[32] E. Saitoh, H. Miyajima, T. Yamaoka, G. Tatara, Nature **432**, 203 (2004).
[33] C. Chappert and T. Devolder, Nature **432**, 162 (2004).
[34] C.W. Sandweg , N. Wiese, D.R. McGrouther, S.J. Hermsdoerfer, H. Schultheiss, B. Leven, B. Hillebrands, and J.N. Chapman, J. Appl. Phys. **103**, 093906 (2008).
[35] M.J. Donahue and D.G. Porter, *Oommf user's guide, version 1.0* (Interagency, Report NISTIR 6276, National Institute os Standards and Technology, Gaithersburg, MD, 1999).

6.5 Spin-wave excitation in Permalloy by oscillating pinned domain walls

H. Schultheiss, S.J. Hermsdörfer, C. Rausch, S. Schäfer, B. Leven, and B. Hillebrands

The dynamic properties of ferromagnetic thin films have attracted much attention in the past years due to their huge importance both for basic understanding of new phenomena as well as for technological applications. Especially the possibility to create logic circuits of magnetic features like domain walls [1] or spin-waves [2, 3] is in the focus of research activities. Thus, the excitation and propagation of spin-waves and their interaction with domain walls is of general research interest. To create spin waves, several techniques have been employed so far, in the easiest way by an antenna structure [4]or, to name another example, by vortex-anti-vortex-annihilation [5].

In this section a new mechanism for the spin wave excitation is presented. The basic idea of the mechanism is that whenever a pinned domain wall is displaced from its equilibrium position the pinning potential is driving the wall back towards this position. This relaxation occurs as a damped oscillation with characteristic eigenfrequency. In case that the domain wall is excited by an external field with this eigenfrequency, a “steady-state” oscillation forms out with the eigenfrequency and an amplitude determined by the energy balance between the dissipation processes due to damping and the external triggering by the applied field. The energy pumped into the system by the external field leads not only to the compensation of the damping but also to the radiation of spin waves. As the wall is pinned it will always be driven back towards the equilibrium position. This ensures that the wall itself is not travelling along the structure by the externally applied field but influences the magnetic moments in the stripe in particular in the vicinity of the cross area, i.e. in the area where the arms met and the domain wall is situated. Similar investigations [6] used spin-polarized currents to move the domain wall and did not focus on the creation of spin waves.

Micromagnetic simulations using the LLG-code by Prof Michael Scheinfein have been performed to get a proof of principle [7]. The used material is $Ni_{81}Fe_{19}$ and the standard values for this material (saturation magnetization M_s=800 G, exchange constant A=1.05 µerg/cm^3) have been taken into account. The total length of the simulated volume is 1 µm, the width 400 nm, and the thickness 5 nm with cell sizes of 10 nm for the x- and y-direction and 5 nm for the z-direction, respectively. These small dimensions have been chosen for the sake of calculation time. The geometry is a cross with arm widths of 50 nm for the longer arms along the x-direction and 30 nm for the shorter arms along the y-direction (see Fig. 1). The shape anisotropy forces the magnetic moments to align

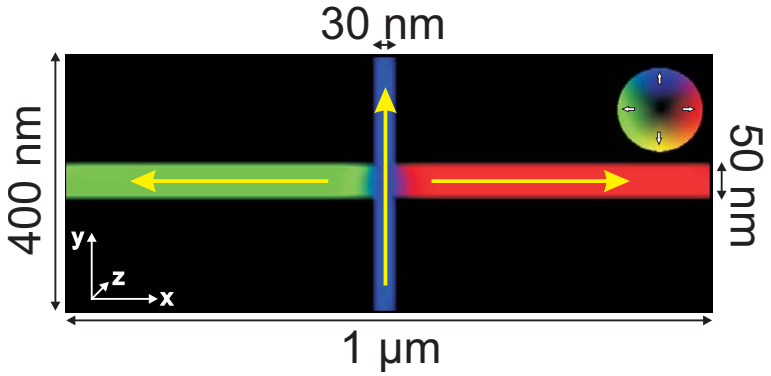

Fig. 1: Domain wall configuration after relaxation. The shape anisotropy fixes the magnetization in the arms in the direction of the arms and forms a tail-to-tail domain wall. The magnetization directions are displayed in the given greyscale code. The denomination of the axes is given in the bottom left corner.

along the direction of the arms. The domain wall along the y-axis arm can be created by saturating the complete structure in this direction and subsequent relaxation to remanence afterwards. This configuration represents a rather steep pinning potential for the domain wall as the wall is pinned at two sides in the cross section area and can therefore not move freely. The starting configuration of the structure after energy relaxation exhibiting a tail-to-tail domain wall is presented in Fig. 1.

The excitation of the domain wall is most efficient in means of creating spin-waves for the resonance frequency of the domain wall. To find this resonance frequency, the complete structure has been excited by a weak magnetic field pulse (amplitude 10 Oe, duration 100 ps, total simulation length 25 ns) in the +x-direction. This excites all magnetic moments which are not aligned along the x-direction, i.e. the moments in the smaller side arms as well as the edge domains which form at the end of the main arms due to the stray field. The pulse shape has been chosen to excite all frequencies and after performing a Fourier transformation (hereafter referred to as FFT), the resonance frequency of the domain wall can be obtained. As already mentioned in the introduction, the later excitation of the domain wall with this resonance frequency leads to a maximum amplitude of the domain wall oscillation and, therefore, to a the most efficient excitation of spin-waves. After performing the Fourier transformation of the pulse, the resonance frequency for the domain wall has been found to be 5 GHz and this frequency has been used as the excitation frequency for the following investigations. By exciting the structure with an external field of this frequency and an amplitude of 10 Oe, the domain wall starts to oscillate and, as explained above, emits spin-waves. The amplitude of the external field is much smaller than the depinning field necessary to drive the domain wall out of its pinning center. This shows that in the case of a resonant excitation of the domain wall even with a small amplitude of the external field (in comparison to the depinning field) a big amplitude of the domain wall oscillation can be achieved.

For evaluating the simulations and visualization of the domain wall motion the simulated structure is cut in the middle of the y-axis. For a consistent study of this motion, the end of the transient phenomenon, i.e. the steady state of the motion has to be reached. Then, the domain wall motion

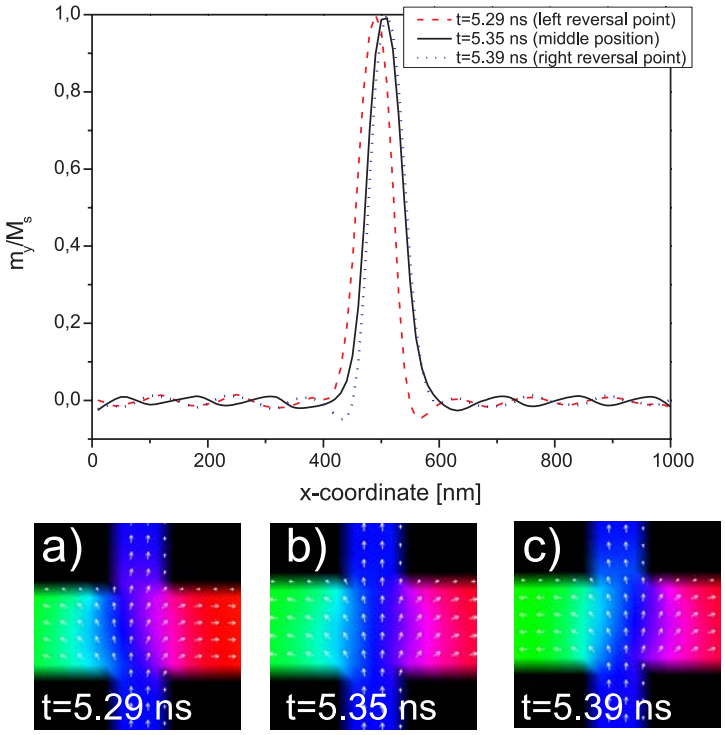

Fig. 2: y-component of the magnetization along the long axis of the stripe at different times. The movement of the domain wall in the middle of the stripe as well as the excitation of spin waves in the outer parts can be clearly seen. The bottom row shows the corresponding domain configuration at a) 5,29 ns, b) 5,35 ns, and c) 5,39 ns. The slight movement of the wall from left to right within this period of time can be clearly identified.

as well as the excited spin waves can be seen by evaluating the magnetization's y-component. Fig. 2 shows the m_y-component along a cut in the middle of the wider arms parallel to the x-axis. The domain wall can be identified in the middle of the graph, its movement is displayed by the two curves taken at different times and the emission of spin waves can be seen as oscillations in the outer regions of the stripe. The curves have been taken at different times after the end of the transient phenomenon in the middle of the structure and show the evolution of the domain wall movement. The corresponding domain configurations have been added to the bottom row of the figure and show the movement of the domain wall from left to right.

From Fig. 2 the wavelength of the emitted spin waves can be obtained by measuring the peak-to-peak distance of the oscillations and yields for a value of 140 nm. A more detailed insight into the observed phenomenon is given in Fig. 3. In this figure, the temporal evolution of all three magnetization components along the x-axis, but for a fixed point in y-direction in the middle of the structure is shown. The first column shows the first few ns of the oscillation. The domain wall can be clearly identified in the middle of each picture. The external applied field needs some time to force the wall to oscillations but after the end of this transient phenomenon after approximately 1.5 ns, a regular oscillation of the wall can clearly be seen. The second row gives an enlarged view of the steady-state oscillation for a period of 1 ns. It clearly shows that the wall oscillates with a frequency of 5GHz.

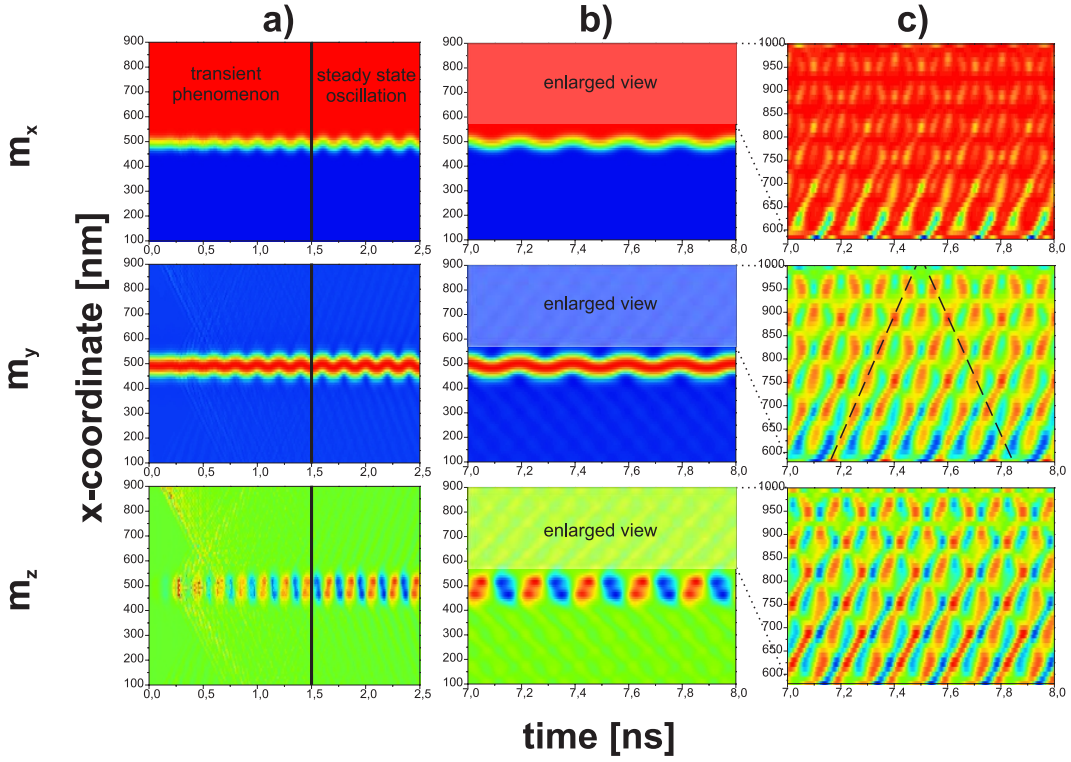

Fig. 3: x-, y-, and z-component of the magnetization along the x-axis of the system mapped over the time at a y-position in the cross area. a) temporal evolution of the system for the first 2.5 ns. The transient phenomenon in the first 1.5 ns as well as the following steady-state oscillation of the domain wall in the middle of the structure can be clearly identified. b) temporal evolution of the system after the end of the transient phenomenon for a time of 1 ns. The resonance frequency of the wall region of 5 GHz can be derived. c) Enlarged view of the arm region of the structure for a duration of 1 ns. The emission of spin-waves from the oscillating domain wall and their propagation as well is shown. The slope of the straight lines given here is used to calculate the spin-wave velocity.

The spin-wave emission in the wider arms can be observed best in the y- and z-component because these directions are perpendicular to the equilibrium orientation of the magnetization and are zero in the initial state. In Fig. 3a the emission starts with the first movement of the wall as can be seen from the z-component. Is is obvious that the m_z-component of the wall changes its sign during the oscillation, as can be seen from the bright and dark areas in the middle of the graph. As the amplitude of the spin-waves is small in comparison with the oscillation of the domain wall itself, the spin-waves are only weakly visible in Fig. 3a and Fig. 3b. Enlarging only one arm of the cross in Fig. 3, the spin wave emission can be seen more clearly in all three components. Additionally, the stripe's edges radiate spin waves as well due to the fact that also the edge domains at the end of the stripe are excited by the external magnetic field. The emission of spin waves from these edge domains can be seen as well in the z-component as the straight lines moving towards the domain walls starting from the edges.

The velocity of the spin waves emitted from the wall can be calculated using the slope of the straight lines shown in Fig. 3c and yields a value of $1.25\,\mu m/ns$.

The interference pattern visible in Fig. 3c results from spin waves created by the oscillating domain wall and propagating along the arm till its end where they are reflected and overlap with the incoming waves. In addition, the spin-waves emitted from the edge domains as described above overlap with the propagating waves, too.

The frequency of the propagating spin-waves can be obtained by a Fourier-transformation. Fig. 4 shows the spatial distribution of the FFT data. It is evident that the frequency of the external field, 5 GHz, is only present in the domain wall whereas the higher harmonics of this mode can also be seen in the arms, too. The highest intensity for the radiated spin-waves is obtained for the mode with 10 GHz, the mode with 15 GHz is still observable in the FFT map but less pronounced.

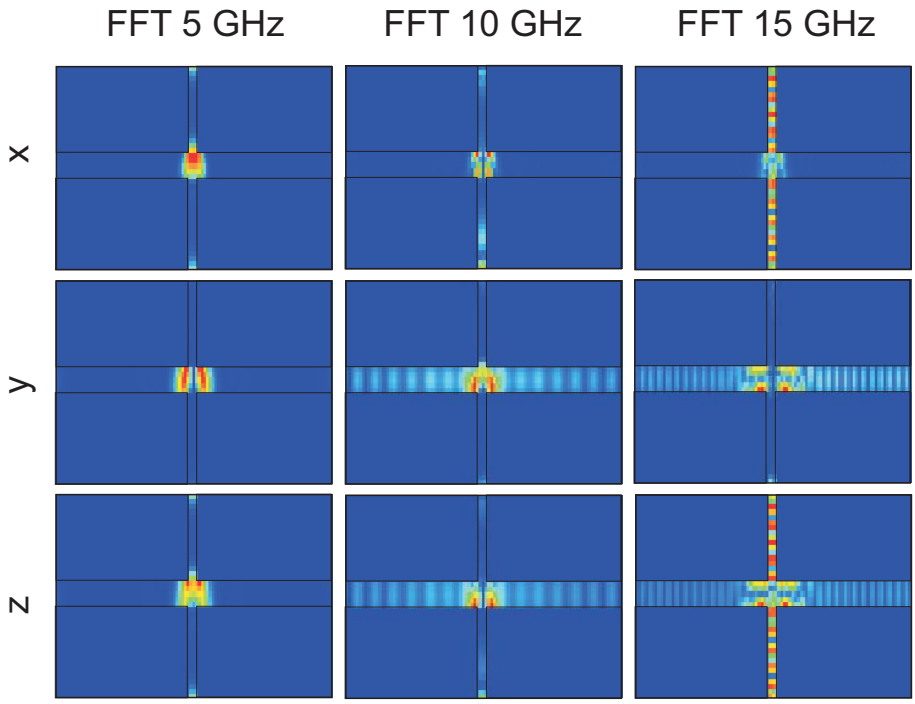

Fig. 4: Spatial distribution of the modes obtained by FFT. The external field with a frequency of 5 GHz excites only the cross area, whereas the higher harmonics are present in the arms. The mode with a frequency of 10 GHz has the highest intensity there. The cross has been added as a guide to the eye.

In summary, micromagnetic simulations reveal the possibility to create spin-waves by the excitation of a pinned domain structure with an external magnetic field. The pinning is necessary to drive the excited domain wall back to its equilibrium position. The properties of the created propagating spin-waves like frequency, wavelength, and velocity can be determined from the simulation data.

Financial Support by the DFG within the Priority Program 1133 is gratefully acknowledged.

References

[1] D.A. Allwood, G. Xiong, C.C. Faulkner, D. Atkinson, D. Petit, R.P. Cowburn, Science **309**, 1688 (2005).
[2] T. Schneider, A.A. Serga, B. Leven, B. Hillebrands, R.L. Stamps, M.P. Kostylev, Appl. Phys. Lett. **92**, 022505 (2008).
[3] K.-S. Lee, S.-K. Kim, J. Appl. Phys. **104**, 053909 (2008).
[4] V. Vlaminck, M. Bailleul, Science **322**, 410 (2008).
[5] K.-S. Lee, S. Choi, S.-K. Kim, Appl. Phys. Lett. **87**, 192502 (2005).
[6] E. Martinez, L. Lopez-Díaz, O. Alejos, L. Torres, Phys. Rev. B **77**, 144417 (2008).
[7] M.R. Scheinfein, LLG Micromagnetic Simulator™, http://llgmicro.home.mindspring.com.

6.6 Breathing domain wall in $Ni_{81}Fe_{19}$ cross structures

H. Schultheiss, S.J. Hermsdörfer, C. Rausch, S. Schäfer, B. Leven, and B. Hillebrands

Previous investigations on the temporal evolution of the magnetization state in $Ni_{81}Fe_{19}$ cross structures have shown that it is possible to generate spin waves with the help of an oscillating, pinned domain wall (see Section 6.5 of this Annual Report). The spin waves have been excited by applying an external field perpendicular to the magnetic moments inside the domain wall. Another possibility to influence the magnetization distribution in this cross structure is the application of a field parallel to the magnetic moments in the domain wall, i.e. in the case discussed in this Section (see Fig. 1). In this case, mainly the magnetic moments at the border of the domain wall will be influenced and can be rotated into the direction of the external field and, thus, enhance the width of the wall [1]. Hence, a periodic change of the external field influences the domain wall width which is increased or decreased depending on the direction of the externally applied field. This results in a kind of “breathing” domain wall. This periodic change in the domain wall width and the denotation as “breathing” has been made earlier [2–4] but in this Section we will focus on the temporal evolution of a system with geometrically pinned domain wall.

For the determination of the temporal evolution of the system, micromagnetic simulations using the LLG-code have been performed [5]. As described in Section 6.5, the simulated structure consists of $Ni_{81}Fe_{19}$ and the standard values for $Ni_{81}Fe_{19}$ have been used (saturation magnetization M_s=800 G, exchange constant A=1.05 µerg/cm^3). The simulated volume is the same as presented in the previous Section (length: 1 µm, width 400 nm, and thickness 5 nm with cell sizes of 10 nm for the x- and y-direction and 5 nm for the z-direction, respectively). The cross shape of the structure is used again, allowing for a steep pinning potential [6]. The starting remanence configuration after relaxation together with the relevant lengths is presented in Fig. 1. This configuration ensures that the domain wall is pinned at a defined position and cannot move freely along the stripe.

The external sinusoidal field is applied in the y-direction as defined in Fig. 1. This enables the magnetic moments in the border area of the domain wall to oscillate periodically with the external field and, thus, make the domain wall breathe. If only the domain wall itself is meant to be influenced by the external field, the frequency has to be chosen not to match any spin-wave resonance conditions for the arms. In the latter case spin waves would be directly excited by the sinusoidal magnetic

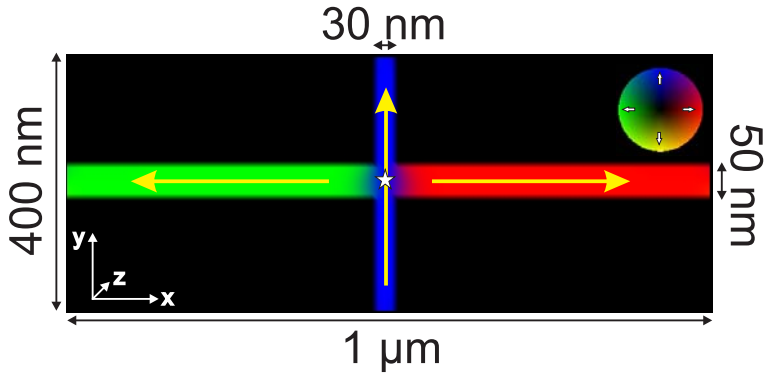

Fig. 1: Domain wall configuration after relaxation. The shape anisotropy fixes the magnetization in the arms in the direction of the arms and forms a tail-to-tail domain wall. The magnetization directions are displayed in the given greyscale code. The denomination of the axes is given in the bottom left corner.

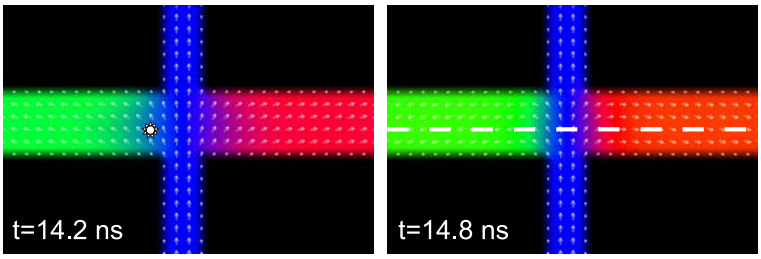

Fig. 2: Changing domain wall width for two different points in time. The change in the width can clearly be observed for a maximum of the oscillation at 14.2 ns and a minimum at 14.8 ns. The white star and the white dashed line mark the points where the data have been evaluated as reported in the main text.

field and would dominate any dynamics created due to the breathing domain wall. For this reason the excitation frequency has then been chosen to 1 GHz. This frequency is far below any spin-wave resonance frequency and acts therefore only on the domain wall (and the edge domains) leaving the arms unaffected. The amplitude of the externally applied field has been set to 300 Oe. Such a high field value is required to overcome the shape anisotropy and to cause a significant tilting of the magnetic moments in the border region of the domain wall. Applying an oscillating field with these parameters, the change in the wall width can clearly be seen in Fig. 2.

The duration of the applied field was 16 ns, the total simulation length 20 ns. Exemplarily, two points in time have been selected showing a maximum domain wall extension of about 70 nm (14.2 ns) and a minimum wall width of about 30 nm (14.8 ns). Fig. 3 shows the temporal evolution

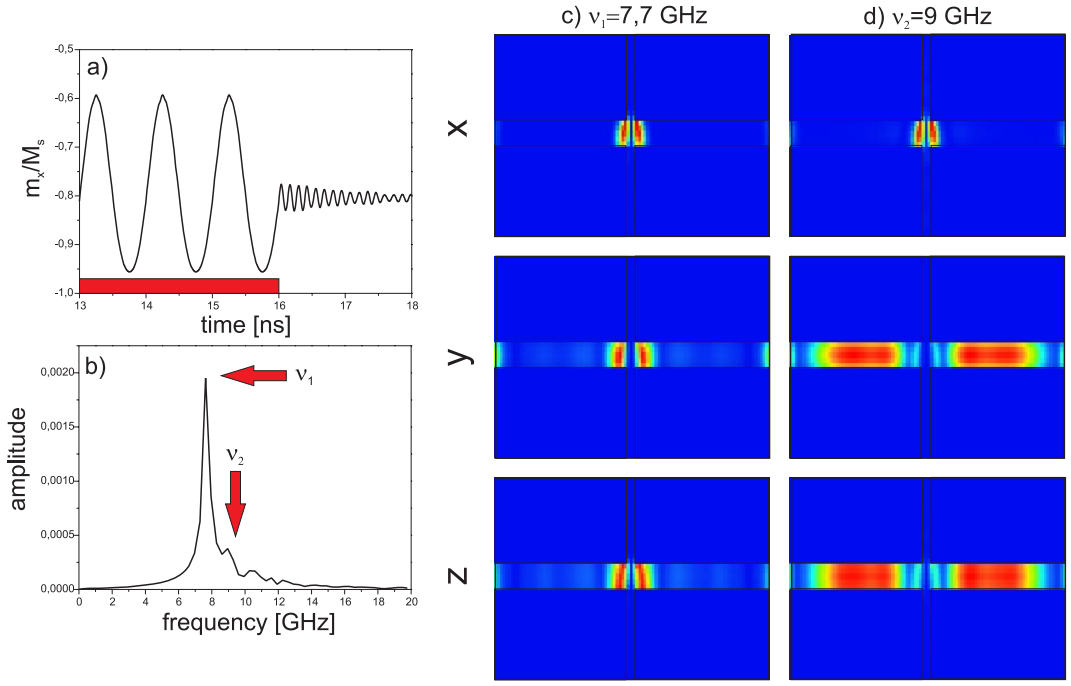

Fig. 3: a) Temporal evolution of the x-component of the magnetization at the end of the applied field pulse (the pulse duration is denoted by the box at the x-axis) at the point marked by the white stripe in Fig. 2. The oscillation with the frequency of 1 GHz as well as the oscillation with the eigenfrequency can be identified. b) FFT of the temporal evolution after the end of the applied field pulse. The triggering frequency is not visible anymore but two main peaks at 7.7 GHz and 9 GHz can be identified. c) spatially resolved FFT for the frequency at 7.7 GHz. It is obvious that this mode is present in the domain wall. d) spatially resolved FFT for the frequency at 9 GHz. In contrary to the mode presented in c) this mode is also present in the wider arms. All graphs have been taken for the point just out of the domain wall as marked in Fig. 2

as well as FFT maps for a position just out of the domain wall which is marked by the white star in Fig. 2. As can be seen from Fig. 3a the magnetic moments are forced by the external field to oscillate with the given frequency until the pulse ends and oscillate with their eigenfrequency afterwards.

As already described, the excitations with an eigenfrequency of the arms is not suitable for studying any possible propagating spin-wave excitation as it will bring the moments situated there to oscillate in resonance and, hence, this oscillation will superimpose any other signal. The FFT presented in Fig. 3b has been taken only for the decaying oscillation after 16 ns and shows that two frequencies determine the behavior of the system: a main oscillation at 7.7 GHz and a weaker one at 9 GHz (Fig. 3b). The FFT maps shown in Fig. 3c and Fig. 3d, respectively, reveal that the 7.7 GHz mode is localized in the vicinity of the domain wall and can thus be interpreted as the

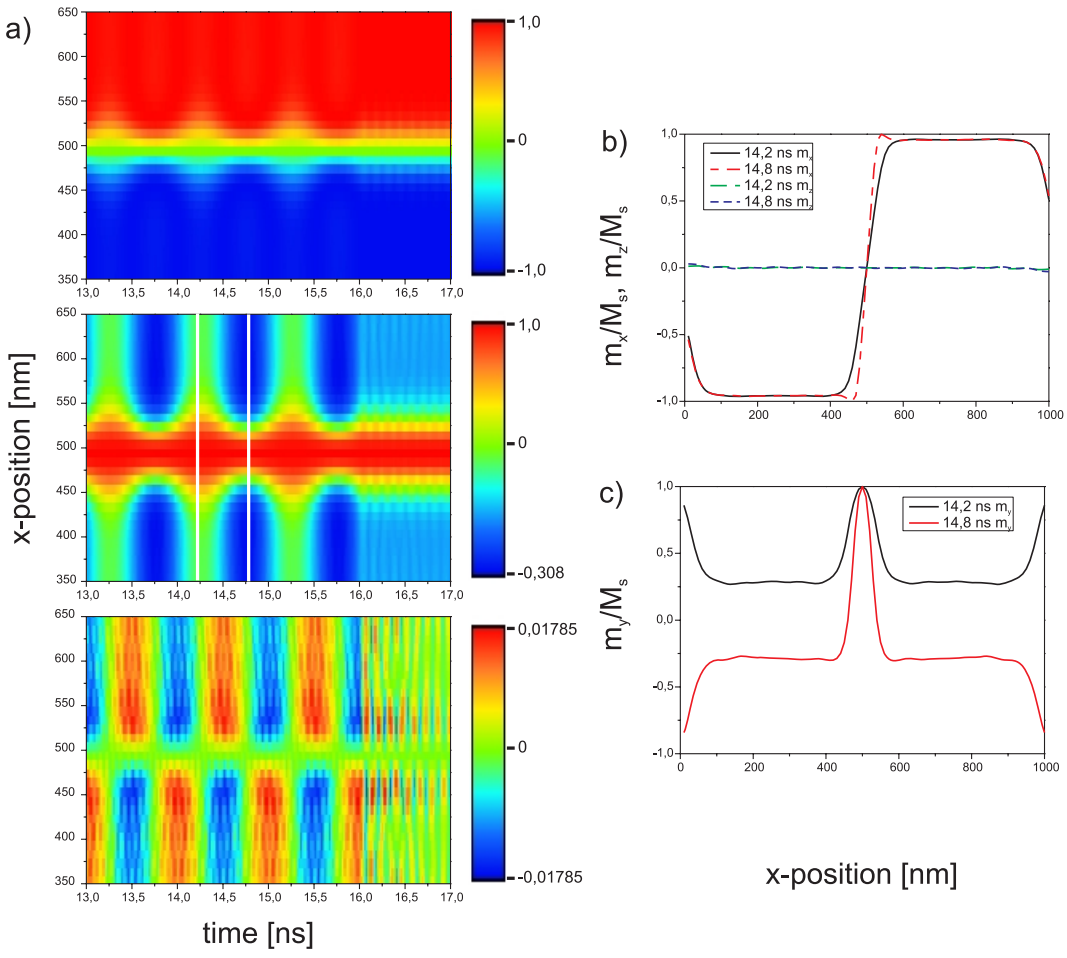

Fig. 4: a) Temporal evolution of the m_x-, m_y-, and m_z-component of the magnetization taken at the dashed line marked in Fig. 2. The position of the domain wall is located in the center of the x-axis and as long as the external field is applied (till 16 ns) a clear oscillation of the domain wall width can be observed. After the end of the external magnetic field pulse the domain wall oscillates with its eigenfrequency but with much lower amplitude. In the z-components the emission of spin-waves from the edge domains can be seen. b) m_x- and m_z-component taken at the two different points in time marked in a) as solid lines in the y-component. The first point is at the maximum of the oscillation at 14.2 ns, the second at the minimum for 14.8 ns. The change in the width can be seen from the x-component whereas the z-component is nearly unaffected from the external field. The edges are excited by the external field as well and emit the already described spin-waves. c) y-component of the magnetization for the same points in time as in b). The changing width of the wall can be identified again. In addition, the periodic changing of the direction of the magnetic moments in the arms can be seen, too.

eigenfrequency of the domain wall, whereas the 9 GHz mode can be identified as a standing wave in the arms.

Fig. 4a shows the temporal evolution along the dotted line marked in Fig. 2 for all three magnetization components. The domain wall can be identified in the middle of each picture and its change in shape and width can clearly be seen. The chosen time window for the graphs is at the end of the external magnetic field pulse. Thus, the left-hand side shows the given frequency of 1 GHz where a clear change in the domain wall width can be observed for a time below 16 ns, i.e., when the field pulse is applied. After the end of the pulse at 16 ns the width oscillates with the domain wall eigenfrequency of 7.7 GHz and does not change significantly anymore. This shows that a large magnetic field is needed to align the magnetic moments at the border region of the domain wall apart from the direction defined by the shape anisotropy. Furthermore, Fig. 4a shows that the external field influences all three components. Fig. 4b and c are obtained by a cut at the positions shown in Fig. 4a and present the x- and z- component (b) and the y-component (c), respectively, at a maximum of the oscillation at 14.2 ns and at a minimum at 14.8 ns (see also Fig. 2). Again the changing domain wall width can be identified clearly. In the y-component given in Fig. 4c also the changing orientation of the magnetic moments in the wider arms can be seen. However, an excitation of spin waves is not observed. In contrary to the x- and y-component, the z-component is only weakly influenced by the external field, as can be seen from Fig. 4b. The amplitude of the oscillation in z-direction is close to zero. As a result, the magnetic moments at the border of the domain wall are periodically changing their direction driven by the external field but are oscillating only in the sample plane as nearly no out-of-plane-component (z-direction) can be observed. As reported in Section 6.5, the latter component is most efficient for the excitation of spin waves. The spin waves visible in the z-component in Fig. 4a result from oscillations of the edge domains, which are excited by the external applied field as well. As these moments can move more freely than those in the pinned domain wall, they are able to generate spin waves which are propagating along the stripe.

To summarize the results, a domain wall pinned in a cross structure has been excited by an oscillating field pulse in y-direction. The frequency and the amplitude have been chosen to fit the resonance requirements for a periodic change of the width of the wall but do not affect the arms. This leads to a periodic change in the width of the domain wall, i.e. a breathing effect, but not to the excitation of spin waves due to the domain wall motion as the z-component remains nearly unaffected.

Financial support by the DFG within the Priority Program 1133 is gratefully acknowledged.

References

[1] M.T. Bryan, T. Schrefl, D. Atkinson, D.A. Allwood, J. Appl. Phys. **103**, 073906 (2008).
[2] J.C. Slonczewski, J. Appl. Phys. **55**, 2536 (1984).
[3] R.L. Stamps, A.S. Carrico, P.E. Wigen, Phys. Rev. B **55**(10), 6473 (1997).
[4] A.L. Dantas, M.S. Vasconcelos, A.S. Carrico, J. Magn. Magn. Mater. **226-230**, 1604 (2001).
[5] M.R. Scheinfein, LLG Micromagnetic Simulator™, http://llgmicro.home.mindspring.com.
[6] D. Petit, A.-V. Jausovec, H.T. Zeng, E. Lewis, L. OBrien, D. Read, R.P. Cowburn, Appl. Phys. Lett. **93**, 163108 (2008).

6.7 Magneto-optic investigations on the switching dynamics of TMR structures

G. Wolf, A. Conca Parra, H. Schultheiss, B. Leven, and B. Hillebrands[1]

In the last years the magnetism community has witnessed the introduction of the first magnetic random access memory (MRAM) devices into the market by Freescale Semiconductors, Toshiba/NEC and Motorola [1–3]. These pioneering products are already substituting static random access memory (SRAM) and FLASH memories. MRAM chips are currently being used in touch-screen products for the automotive industry [4] and in aerospace applications where both hard environment resistant and radiation hardened memories are required [5–7]. One of the main advantages of the MRAM devices in comparison with the widely used SRAM chips lays in the non-volatility of the stored information. This fact allows for a potential reduction of power consumption. This is crucial for mobile devices, which are dependent upon batteries for their energy supply [10]. Solid-state FLASH memories also offer non-volatility but the writing power per bit exceeds in several orders of magnitude of the one needed for MRAM or SRAM devices [8]. Furthermore, FLASH memories suffer a certain degradation with every writing cycle, what constitutes an additional drawback.
However, for MRAM technology, to be successful, a key issue must be addressed. The marketed MRAM products provide writing cycles of 35 ns [9] which are competitive with the much larger values of FLASH but still multiply the ones for SRAM chips. Write power per bit is also larger for MRAM. A reduction of both parameters is only possible with an understanding and control of the switching mechanism in the tunnel magnetoresistance (TMR) elements constituting the MRAM arrays.

Here we present results on the investigation of the dynamic magnetic properties of a TMR element. Time-resolved Kerr-effect gives us direct access to the different components of the magnetization. Using a stroboscopic technique, we are able to study the switching mechanism of the TMR element. A pulsed diode-laser is focused on the sample using a microscope objective . A schematic drawing of the experimental setup can be seen in Fig.1. The laser enters the objective off axis so that the longitudinal Kerr effect can be measured. This gives access to the in-plane components of the magnetization. The resulting size of the laser spot is measured to be smaller than 1 µm. The polarization of the reflected light is analyzed with a Wollaston prism and two photodiodes. The pulsed diode-laser is synchronized with the exciting magnetic field pulses with an electronic delay-generator. Because of the electronic jitter, a total time resolution of less than 60 ps is achieved with a laser pulse width of 36 ps.

The investigated TMR sample consists of a system of two crossed coplanar waveguides (CPWs) and a TMR element placed in the crossing point of the waveguides. The CPWs are used to generate two perpendicular oriented short magnetic field pulses. A deeper lying reset line is used to reset the magnetization of the TMR element to the same state at the beginning of each cycle of the stroboscopic measurement. Each metal layer is insulated by a 3.8 µm thick BCB photoresist. The top CPW is also covered by a BCB photoresist layer in order to provide the very flat surface needed for the growth of the TMR materials. Further details about the sample properties and preparation can be found in [11].

[1] In collaboration with K. Rott, G. Reiss, Fakultät der Physik, Universität Bielefeld, Germany.

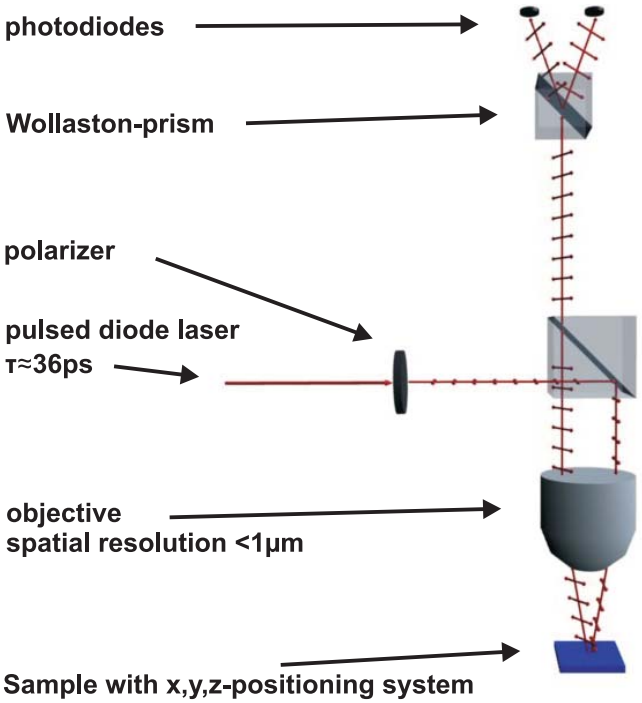

Fig. 1: Schematic drawing of the experimental setup. A pulsed diode laser (pulse length $\tau \approx 36\,\mathrm{ps}$) is focused through a microscope objective on the sample. The polarization of the reflected light is analyzed by a Wollaston prism and detected by two photo diodes. Entering the objective off axis enables to measure the longitudinal Kerr effect. The resulting spacial resolution is better than $1\,\mu\mathrm{m}$.

The TMR stack was deposited and structured by means of rf magnetron sputtering and subsequent electron lithography. The magnetic tunneling junction (MTJ) consists of Ru (7)/ Ta (5)/ IrMn (12)/ CoFeB (3)/ AlO_x (1.8)/ CoFeB (4)/ Ta (10)/ Ru (7), the thicknesses are given in nanometers. An exchange bias is initialized at the interface of the bottom CoFeB layer and the antiferromagnetic IrMn layer, in order to pin the magnetization of the CoFeB layer. The element is elliptically shaped with a size of $6\,\mu\mathrm{m} \times 3\,\mu\mathrm{m}$. Due to the shape anisotropy, the direction of the magnetization points along the long axis of the ellipse in the remanent state. The long axis is oriented perpendicular to the reset line (i.e. the reset magnetic field is parallel to the long axis). We use the so called Savtchenko geometry [12] where the magnetic field of the pulses form an angle of 45° or 135° with the long axis of the ellipse (see Fig. 2). In all figures CPW1 denotes the top waveguide, CPW2 the bottom waveguide.

In Fig. 3 the minor loop (corresponding to the top free ferromagnetic layer) of the sample is shown. The most important feature is the shift of the hysteresis loop from the zero field value due to a

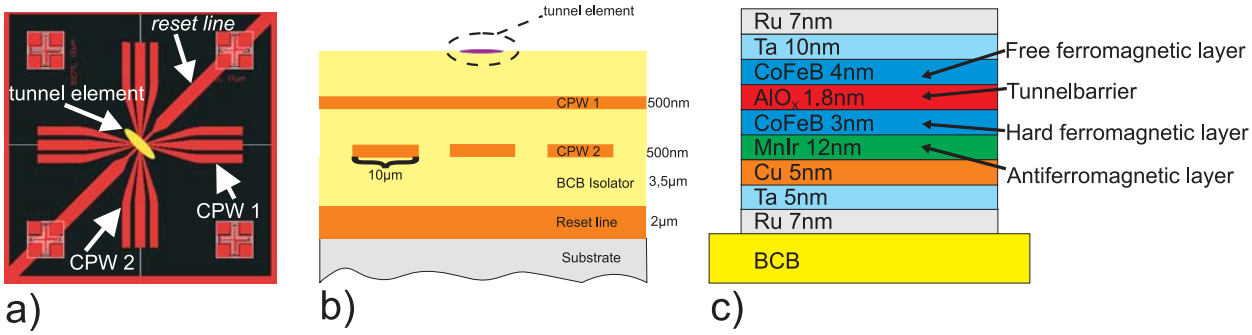

Fig. 2: Schematic description of the sample. a) top view: the long axis of the ellipse is oriented in 45° with respect to the CPWs. b) cross section: The CPWs are isolated from each other by a BCB photoresist layer. c) cross section of the MTJ: CoFeB/AlO_x/CoFeB layers form the tunneling junction. The lower CoFeB layer is exchange biased with the antiferromagnetic IrMn layer.

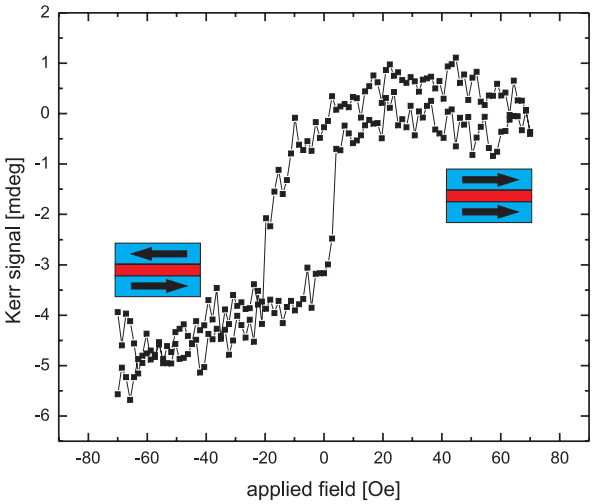

Fig. 3: Minor loop of the TMR element, corresponding to the top free ferromagnetic layer. The asymmetry in the hysteresis curve is due to coupling between the free and the pinned ferromagnetic layer.

magnetic coupling between the top free layer and the bottom pinned layer. The asymmetry in the minor loop is a major problem since only one magnetic state is available at remanence which may prevent a complete switching. The most probable reason for the magnetic coupling between the exchange biased layer and the free layer is orange peel coupling due to interface roughness.

The dynamic response of the MTJ element to two nanosecond magnetic field pulses has been studied. The magnetic field pulse generated in CPW1 excites the magnetization under an angle of 45°. After a time delay, the second field pulse, generated in CPW2, sets in under an angle of 135° with respect to the initial state. This pulse is expected to reverse the magnetization.

Figure 4 shows three measurements of the longitudinal component of the magnetization (plane of incidence is along the long axis of the ellipse). In this measurement series, the duration and magnitude of the pulses remain constant and the relative delay is changed, thereby varying the overlapping of the pulses. The length of the pulses was set to 2 ns. The magnetic field strength at the sample position can be estimated by solving the Biot-Savart law for a rectangular conductor with the given geometrical properties of the CPWs. A 10 V pulse in CPW1 corresponds to a magnetic field of about 80 Oe, a 40 V pulse in CPW2 to 220 Oe. The overlap of the field pulses varies from no overlap to 0.5 ns to 1 ns. In all cases a similar situation is observed, the magnetization tilts out of the initial state while the pulses are applied. When the last pulse is switched off, the magnetization relaxes back to the initial state, instead of relaxing to a state with opposite orientation. The reason for this behavior may be related to the shift of the hysteresis loop of the free layer as shown in Fig. 3. Only one magnetic state is stable at zero field.

Some numerical calculations have been performed, solving the Landau-Lifshitz and Gilbert equation for the experimental situations:

$$\frac{d\mathbf{M}}{dt} = -\frac{|\gamma|}{1+\alpha_G^2}\mathbf{M}\times\mathbf{H_{eff}} + \frac{\alpha_G}{M_s}\left[\mathbf{M}\times(\mathbf{M}\times\mathbf{H_{eff}})\right] \quad . \tag{1}$$

$\mathbf{H_{eff}}$ includes uniaxial and unidirectional anisotropy fields, demagnetizing fields as well as the dynamic pulsed fields $\mathbf{H_{pulse1}}$ and $\mathbf{H_{pulse2}}$. The anisotropy fields were taken from the quasi-static magneto-optic characterization (not shown here). The corresponding component of the magnetization is plotted in the graphs (solid line) along with the experimental results (dots). The numerical calculations show a behavior similar to the experimental results. The magnetization relaxes to the initial state after the pulses end. However it can be noted that the relaxation process is slower in the measurements compared to the simulations.

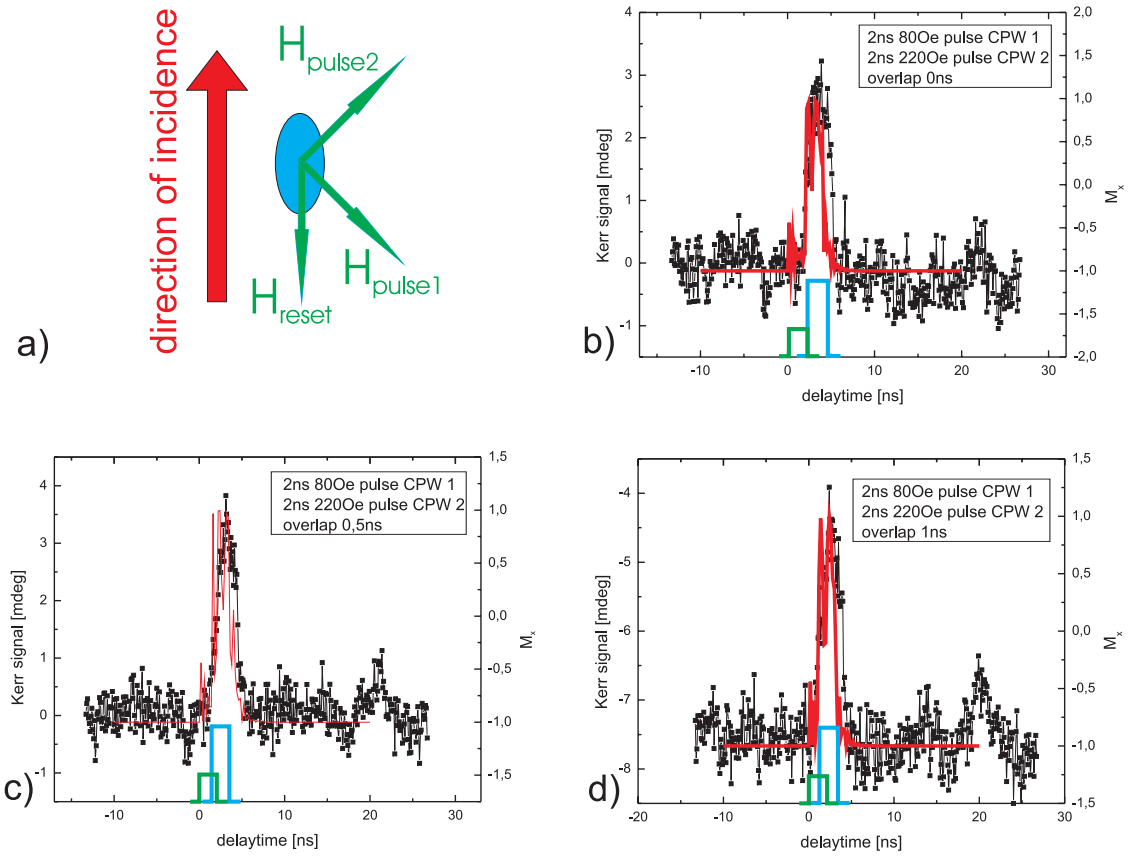

Fig. 4: Time-resolved measurement of the longitudinal component of the magnetization (parallel to the long axis of the ellipse) under the influence of two orthogonal magnetic field pulses with different pulse overlap. a) Schematic description of the measurement geometry. b) - d) The points represent the measured Kerr signal, while the solid line represents the numerical calculation, solving the Landau-Lifshitz and Gilbert equation. The overlapping of the pulses varies from 0 ns, 0.5 ns to 1 ns.

In order to gain further insight into the switching dynamics of the element, additional measurements of the transversal component of the magnetization were taken (plane of incidence is perpendicular to the long axis of the ellipse). In Fig. 5 a measurement series is shown, where again the duration and intensity of the pulses is kept constant and the relative delay is changed. In this case the pulses do not overlap. In comparison the numerical calculations again show a similar behavior. Magnetization returns back to its initial state after the pulses end. In the Kerr signal it is possible to observe a relaxation of the magnetization on the order of 10 to 15 ns. This is contrary to the numerical calculation (solid line) where the magnetization follows a damped trajectory back to the initial state on the order of 5 ns. This points out that the behavior of the magnetization can not be fully described by a macro spin approximation. It can be assumed that the relaxation process is influenced by a complicated domain movement.

In conclusion we analyzed the dynamic response of a TMR element to varying sequences of two magnetic field pulses. However, as expected, due to the shift of the static hysteresis no switching of the free ferromagnetic layer has been observed. However, the measured data can be described at least qualitatively by the numerical calculations solving the Landau-Lifshitz and Gilbert equation. We demonstrated that the combination of dynamic Kerr microscopy and numerical calculations is a good approach to optimize the switching process of TMR elements in order to get faster writing times for MRAM devices.

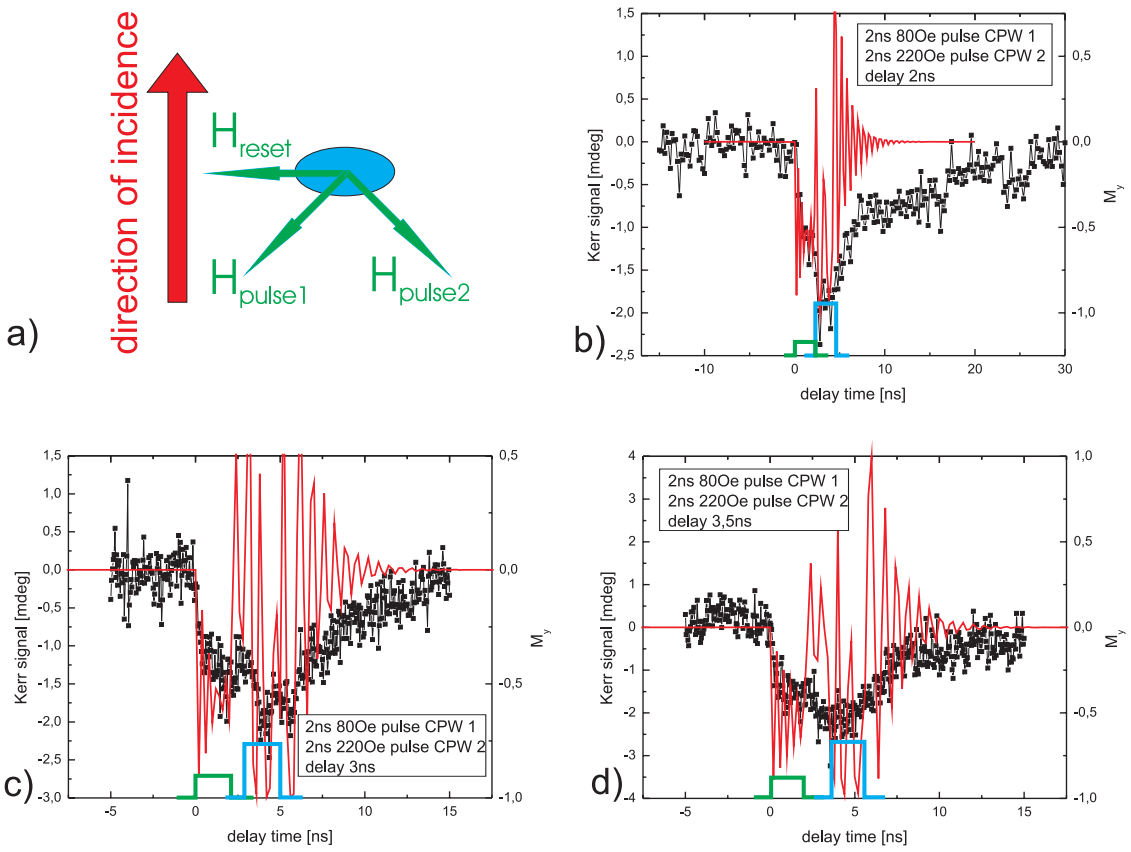

Fig. 5: Time-resolved measurement of the transversal component of the magnetization (parallel to the short axis of the ellipse) under the influence of two orthogonal magnetic field pulses. a) Schematic description of the measurement geometry. b) - d) The points represent the measured Kerr signal, the solid line the numerical calculation solving the Landau-Lifshitz and Gilbert equation. The delay between the magnetic field pulses is varied from 2 ns, 3 ns to 3.5 ns.

We acknowledge the EU-STREP project MAGLOG FP6-50021 for financial support.

References

[1] Freescale Semiconductors, *Freescale Leads Industry in Commercializing MRAM Technology 4 Mbit MRAM Memory Product Now in Volume Production*, press release (2006).
[2] Toshiba and NEC corporation, *Toshiba and NEC Develop World's Fastest, Highest Density MRAM 16-megabit Memory also Realizes Low Voltage Operation for Mobile Application* , press release (2006).
[3] Motorola, *Motorola Produces Worlds First 4 Mbit MRAM Chip*, press release (2006).
[4] Embedded Computing, *Siemens selects Freescale MRAM for industrial automation touch-screen products* (2008).
[5] Motorola, *Honeywell Licenses Motorola's MRAM Technology to Develop Non-Volatile Aerospace Memory Component* , press release (2003).
[6] Scientific American, *Japanese Satellite First to Use Magnetic Memory* (2008).
[7] Freescale Semiconductors, *Angstrom Aerospace - MRAM provides unique high temperature and high reliability capabilities for rugged system designs*, press release (2008).
[8] W.J. Gallagher, S.S.P. Parkin, IBM J. RES. a. DEV. **50** 1 (2006).
[9] Freescale Semiconductors, *Fast Non-Volatile RAM Products* MRAM fact sheet (2007).
[10] NEC corporation, *Toshiba and NEC Develop World's Fastest, Highest Density MRAM 16-megabit Memory also Realizes Low Voltage Operation for Mobile Application* , press release (2006).
[11] P. Martín Pimentel, S.J. Hermsdoerfer, H.T. Nembach, B. Leven, B. Hillebrands, Appl. Phys. Lett. **88**, 122510 (2006).
[12] L. Savtchenko, U.S. Patent 6,545,906, B1 (2003).

B. Nonlinear Spin Waves and Magnonic Crystals

6.8 Investigation and optimization of one-dimensional ferrite-film based magnonic crystals

A.V. Chumak, A.A. Serga, and B. Hillebrands[1]

Magnonic crystals are artificial media with periodic lateral variation of their magnetic properties. They are the magnetic analogue to photonic and sonic crystals that are suitable for operation in the microwave frequency range. Spectra of spin-wave excitations in magnonic crystals are considerably modified with respect to uniform media and exhibit features such as full band gaps, where spin waves are not allowed to propagate. Due to the wide tunability of their characteristic properties these periodic structures offer excellent potential for the investigation of linear and nonlinear spin-wave dynamics. As the spin-wave properties are strictly determined by the wave propagation direction relative to the bias magnetic field, the one-dimensional crystals allowing for operation at only one spin-wave eigenmode are especially interesting for basic research.

Here we present experimental and theoretical results on propagation of backward volume magnetostatic spin waves (BVMSW) in a one-dimensional magnonic crystal. The crystal was produced by etching a groove array in to the surface of single-crystal yttrium-iron-garnet (YIG) ferrite film. We have focused our attention on the backward spin-wave mode due to its potential and special benefits both for the study of non-linear spin-wave dynamics [1, 2], and applications [3, 4]. The YIG film was chosen due to the extremely small damping of magnetic excitations in this material.

To fabricate the magnonic crystals, two YIG films of thicknesses of 5.5 µm and 14 µm were used. Both films were epitaxially grown in (111) crystallographic orientation on gadolinium-gallium garnet substrates. Hot orthophosphoric acid etching and photolithography techniques were utilized to make the grooves. Our lithography was based on a standard photoresist AZ 5214E baked by UV irradiation, which is stable against hot 160 °C orthophosphoric acid. The mask had $N = 20$ parallel lines $w_g = 30$ µm in width and spaced at 270 µm from each other, so the lattice constant was $\alpha = 300$ µm. Groves were perpendicularly oriented with respect to the presumed spin wave propagation direction. In order to study the dependence of crystal characteristics on the groove depth δ the grooves were etched in 100 nm steps from 100 nm to 2 µm. The grooves depth was controlled

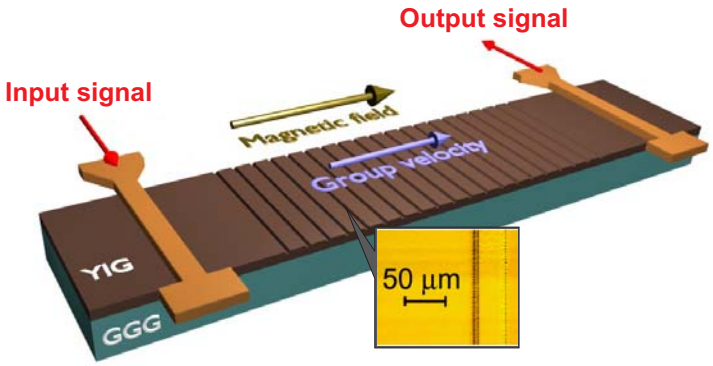

Fig. 1: Structure under investigation.

[1] In collaboration with M.P. Kostylev, School of Physics, University of Western Australia, Crawley, Australia.

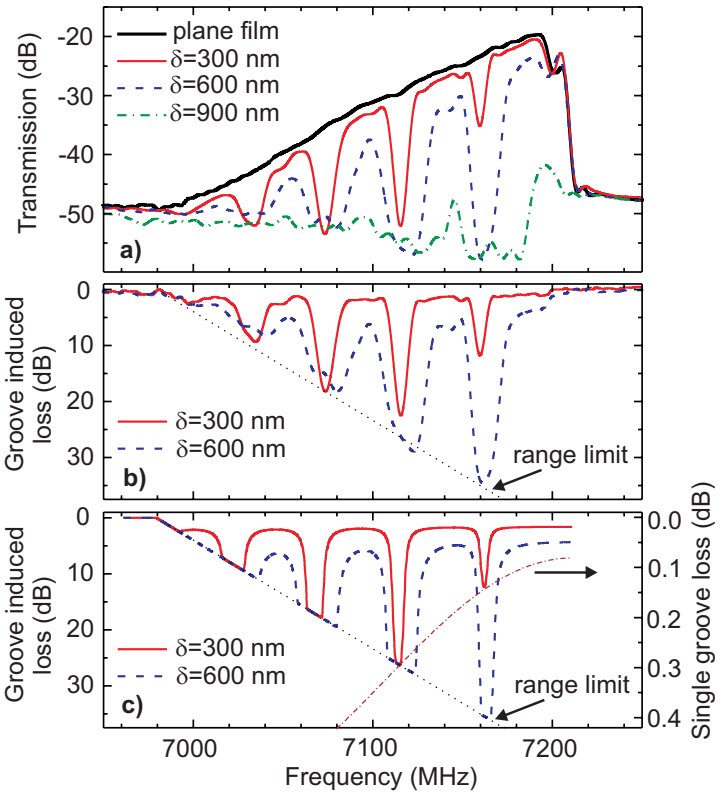

Fig. 2: (a) - measured BVMSW microwave transmission characteristics for an unstructured film (bold line) and for a magnonic crystal with different groove depth δ; (b) - experimental insertion loss caused by crystal structure; (c) - calculated insertion loss; dash-dotted line shows the calculated insertion loss for one groove of 300 nm in depth. (Parameters of calculation: grooves number $N = 20$, groove width on bottom $w_g = 30\,\mu$m, lattice constant $\alpha = 300\,\mu$m, film thickness $d_0 = 5.5\,\mu$m, saturation magnetization $M_0 = 1750\,$G, bias magnetic field $H_0 = 1845\,$Oe, efficiency coefficient $\eta = 5$, resonance line width $\Delta H = 0.5\,$Oe, surface damage coefficient $\zeta = 30$.)

by etching time and measured using a profilometer. Anisotropic chemical etching caused by the YIG crystallographic structure was observed: the speed of etching parallel to the film plane was approximately 10 times higher than in the perpendicular direction, so the final groove depth profile along the direction of wave propagation had a trapezoidal shape. The inset in Fig. 1 shows a microscope photo of the grooves of the magnonic crystal with $\delta = 500\,$nm and $w = 30\,\mu$m.

In order to excite and receive the dipole-dominated spin waves two microstrip antennae were placed 8 mm apart, one in front of the grating, and one behind it (see Fig. 1). A bias magnetic field of 1845 Oe was applied in the plane of the YIG film stripe along its length and parallel to the direction of spin wave propagation. Thus the conditions for BVMSW propagation were given.

The experimental BVMSW transmission characteristics measured for the unstructured (reference) film of 5.5 μm thickness as well as for magnonic crystals with $\delta = 300, 600$ and 900 nm are shown in Fig. 2a. The transmission characteristics for the reference film (bold black line online) is typical for BVMSW: it has the maximum at the point of ferromagnetic resonance, a steep slope towards higher frequencies and a weak slope towards the lower frequencies. Figure 2b shows the losses inserted by the groove structure. To obtain these plots one needs to remove contributions from the antennae insertion losses and of the spin-wave intrinsic spatial damping from the raw data in Fig. 2a. We do this by subtracting the transmission characteristic of the reference film from those of the magnonic crystals. The dotted straight line indicates the approximate limit of the dynamic range of the experimental setup.

From Fig. 2b one sees that the grooves as shallow as 300 nm result already in the appearance of a set of rejection bands (or transmission gaps), where spin-wave transmission is highly reduced. According to the condition for Bragg reflection, higher-order rejection bands correspond to larger wave numbers. In the case of BVMSW the latter correspond to smaller frequencies. From the depths and the frequency widths Δf of the gaps one sees that efficiency of the rejection increases

with increase in the order of Bragg reflection. This suggests that the backward volume waves with smaller wavelengths are more sensitive to the introduced inhomogeneities.

Both Fig. 2a and 2b demonstrate that an increase in δ leads to an increase in the rejection efficiency and in the frequency bandwidth of rejection bands Δf. Additionally a small frequency shift of the minima of transmission towards higher frequencies is observed, as well as an increase in insertion losses in the transmission (i.e., allowed) bands. For $\delta = 900\,\text{nm}$ the insertion loss in the whole spin-wave band is so important that almost no spin wave propagation is observed for the film of $5.5\,\mu\text{m}$ thickness (see Fig. 2a).

The results of our numerical computation of the magnonic crystal microwave characteristics are shown in Fig. 2c. In this work, instead of solving the rigorous direct scattering problem [5], we modeled the grating as a periodical sequence of sections of regular transmission lines with different propagation constants (different spin-wave wave numbers) for the same carrier frequency. We neglect the fact that the groove edges are oblique and model the groove cross-section as a rectangle with the same depth and having the same area. The T-matrix $T^{(1)}$ for a section of unstructured film of the length $a-w$ has only diagonal components: $\mathrm{T}_{11}^{(1)} = 1/\mathrm{T}_{22}^{(1)} = e^{(-ik+k_0'')(a-w)}$, where k is the spin-wave wave number in the unstructured film, $k_0'' = \gamma\Delta H/(2v_{\mathrm{gr}})$ is the rate of spin-wave spatial damping, γ is the gyromagnetic ratio, ΔH is the ferromagnetic resonance linewidth, and v_{gr} is the spin-wave group velocity. Similarly, the T-matrix $T^{(3)}$ for a regular spin-wave film waveguide with the thickness $d = d_0 - \delta$ is $\mathrm{T}_{11}^{(3)} = 1/\mathrm{T}_{22}^{(3)} = e^{(-ik+k_{\mathrm{g}}'')wd_0/d}$; $\mathrm{T}_{12}^{(3)} = \mathrm{T}_{21}^{(3)} = 0$, where k_{g}'' is the spin-wave damping rate for the groove. Here we used the fact that the BVMSW dispersion law for small wave numbers $kd \ll 1$ is practically linear, therefore the spin-wave wave number in the grooves is kd_0/d. To describe the increase of the pass band loss with increase of the groove depth we introduce an empirical parameter ζ which accounts for larger contribution of two-magnon scattering processes in the areas which underwent anisotropic etching. Then the damping rate in the grooves can be expressed as $k_{\mathrm{g}}'' = k_0''(1+\zeta\delta/d_0)$.

There are reflections from the junctions of the consecutive sections. The T-matrix for the front edge of the groove is $T^{(2)}$ and that for the rear edge is $T^{(4)}$. Therefore the T-matrix for one period of the structure is as follows: $\mathrm{T} = [\mathrm{T}^{(1)} \cdot \mathrm{T}^{(2)} \cdot \mathrm{T}^{(3)} \cdot \mathrm{T}^{(4)}]$. To obtain the T-matrix for the whole groove sequence, one has to raise T to the N-th power. The reflection coefficient for a junction of two sections of regular waveguides is Γ. Following [6], the transmission coefficient through the junction is $1-\Gamma$. Then one obtains: $\mathrm{T}_{11}^{(2)} = \mathrm{T}_{22}^{(2)} = (1-\Gamma)^{-1}$; $\mathrm{T}_{12}^{(2)} = \mathrm{T}_{21}^{(2)} = \Gamma(1-\Gamma)^{-1}$, and $\mathrm{T}_{11}^{(4)} = \mathrm{T}_{22}^{(4)} = (1+\Gamma)^{-1}$; $\mathrm{T}_{12}^{(4)} = \mathrm{T}_{21}^{(4)} = -\Gamma(1+\Gamma)^{-1}$.

Now one has to specify the form of the reflection coefficient Γ. Here we use the analogy of the change in the film waveguiding properties to a change of characteristic impedance of a microwave transmission line [7]. We assume that the change of the characteristic impedance of a spin-wave waveguide, because of change in YIG-film thickness, is due to a change of the film effective inductance. Then the characteristic impedance is linearly proportional to the propagation constant (to the spin-wave wave number in our case), and from Eq. (3) in [6] we arrive at a formula for the reflection coefficient for the wave incident onto the edge of the groove from the unstructured section of the film: $\Gamma = \eta\delta/(2d_0-\delta)$. The phenomenological parameter $\eta > 1$ is introduced in this formula to account for eventual factors not taken into account in this simplistic model.

The results of our numerical computation of T^{mc} are shown in Fig. 2. One sees that this model is in qualitative agreement with all the tendencies we see in the experiment. In particular, it shows an increase in the rejection efficiency with an increase in k, and the correct behavior of all characteristics of the rejection bands as functions of δ. It shows that the formation of transmission gaps is due

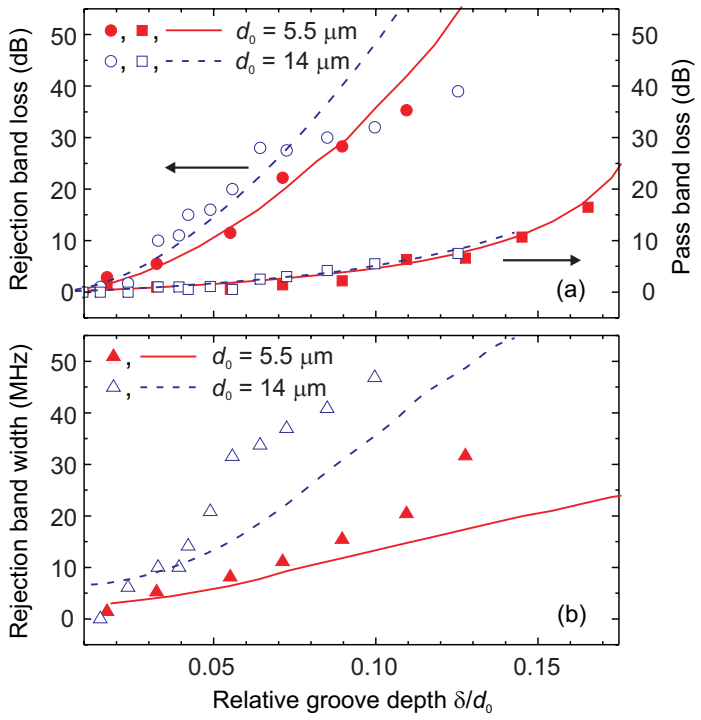

Fig. 3: (a) - measured insertion loss in rejection band (circles) and pass band (squares) as a function of the relative groove depth δ/d_0; lines show corresponding calculated dependencies. (b) - experimental (triangles) and theoretical (lines) values for the width of the first rejection band as a function of the relative grooves depth. Filled red symbols and solid red lines online are for the film thickness $d_0 = 5.5\,\mu m$; opened blue symbols and dashed blue lines online are for $d_0 = 14\,\mu m$. Number of grooves $N = 20$; lattice constant $a = 300\,\mu m$; groove width $w = 30\,\mu m$.

to multiple reflections from edges of all grooves, which form partial standing waves in the space between these grooves. The strength of these reflections is entirely determined by transmission and reflection of a single groove. The latter is shown (in a suitable scale) in Fig. 2c for $\delta = 300\,nm$ by a dash-dotted continuous line. One sees that the peaks of rejection for the 20-grove structure follow this line. However, the quantitative agreement of this model is poor, unless one introduces a value of η considerably larger than 1. In particular, for $\eta = 1$, when the reflection from a grove edge is entirely due to transformation of wavenumber, the model considerably underestimates the depth of transmission gaps. This suggests that other effects such as transformation of modal distribution of dynamic magnetization and eventual generation of other thickness modes (and, possibly, back-transformation) through 2-wave scattering processes give more important contributions to Γ. For this reason the correct depth of transmission gaps is obtained using $\eta = 5$.

The depth of the grooves has a large impact on the characteristics of the fabricated magnonic crystals (see Fig. 2). In order to investigate this effect the rejection efficiency and the bandwidth were studied together with the parasitic losses in the transmission bands inserted by the film structuring. The latter were measured for the second transmission band (i.e., between the first and the second rejection bands). These characteristics were investigated for YIG films of different thicknesses and for different groove depths.

Figure 3 represents the insertion loss (upper panel) and the frequency width Δf_1 measured for the first transmission gap (the central frequency of the gap is 7160 MHz. The horizontal axis is the relative groove depth δ/d_0. In Fig. 3a the insertion loss for the rejection band (left axis) and the transmission band (right axis) are presented for the films 5.5 μm (filled red symbols online) and 14 μm (opened blue symbols online) in thickness. Solid lines are the respective theoretical curves. From Fig. 3a one sees that the rejection efficiency quickly grows with increase in the relative groove depth. Growth of parasitic loss in the transmission bands is also observed. By comparing the losses in the rejection and transmission bands we can determine an optimal relative groove depth. We define as the optimum the situation where rejection is highly efficient but the parasitic loss is still small (less than 3 dB). For both films we find that in the optimum $\delta/d_0 \approx 0.1$.

This corresponds to the rejection efficiency in the minimum of the rejection band of 32 dB and the parasitic loss in the first transmission band of 5 dB.

Both the experimental and theoretical results for different film thicknesses demonstrate that parasitic losses in transmission bands are determined by the relative groove depth only. The functional dependence of the rejection efficiency is more complicated. From Fig. 3a one sees that the dependencies are slightly different for different film thicknesses. If one compares two crystals with the same δ/d_0, the rejection efficiency is higher for the thicker-film based one. However, one observes that with increase in the groove depth the experimental dependencies start to collapse. Thus the relative groove depth is the leading factor for determination of the optimal geometry of the groove array. This more complicated behavior is not seen in the theoretical curves. This suggests that the proposed model is too simplistic to account for this relatively small effect. It also suggests that this theory works best for small groove depths. Apparently, with increase in the groove depth, processes, which have not been taken into account in our model, start playing the dominant role in the spin wave scattering from the grooves.

Figure 3b shows the experimental (symbols) and calculated (lines) dependencies of the width of the first rejection band on δ/d_0. The frequency bandwidth was calculated as the frequency distance between two points at opposite slopes of the transmission gap where the transmitted signal intensity is decreased twice. Bragg reflection condition for both magnonic crystals is fulfilled for the same spin-wave wave numbers, as the lattice constant is the same 300 µm in both cases. As the slope of the dispersion curves increases with increase in the film thickness, this results in different rejection band bandwidths for crystals with the same relative groove depth. One sees that the widths of the first rejection band for the optimal relative groove depth $\delta/d_0 = 0.1$ are 15 MHz and 45 MHz for the films 5.5 µm and 14 µm in thickness, respectively. This provides more flexibility in designing magnonic crystals with required parameters. A required rejection band width can be obtained by properly choosing the absolute groove depth. Then one obtains the required rejection efficiency by choosing a proper value for the relative groove depth.

In conclusion, we experimentally demonstrated that in the BVMSW configuration a one-dimensional magnonic crystal showed excellent spin-wave signal rejection of more than 30 dB. It was found that the optimal groove depth (ensuring that the loss in the transmission band inserted by the lattice is smaller than 5 dB) is approximately 10 % the film thickness. For larger groove depths the parasitic loss in the transmission bands grows faster than the rejection efficiency. The width of the rejection bands exceeded the values for the other spin wave configurations [8, 9], and could be controlled by the groove depth. A simple model was proposed which is in qualitative agreement with the experimental results.

Support by the Deutsche Forschungsgemeinschaft within SE 1771/1-1 is gratefully acknowledged.

References

[1] A.A. Serga, B. Hillebrands, S.O. Demokritov, A.N. Slavin, P. Wierzbicki, V. Vasyuchka, O. Dzyapko, A. Chumak, Phys. Rev. Lett. **94**, 167202 (2005).
[2] S.O. Demokritov, A.A. Serga, V.E. Demidov, B. Hillebrands, M. Kostylev, B.A. Kalinikos, Nature **426**, 159 (2003).
[3] Yu.V. Kobljanskyj, G.A. Melkov, A.A. Serga, V.S. Tiberkevich, A.N. Slavin, Appl. Phys. Lett. **81**, 1645 (2002).
[4] M.P. Kostylev, A.A. Serga, T. Schneider, B. Leven, B. Hillebrands, Appl. Phys. Lett. **87**, 153501(2005).
[5] M.P. Kostylev, A.A. Serga, T. Schneider, T.Neumann, B. Leven, B. Hillebrands, R.L. Stamps, Phys. Rev. B **76**, 184419 (2007).
[6] W. Berry, IEEE Trans. Microwave Theory Tech., **MTT-34**, 80-84 (1986).
[7] B.A.Kalinikos, private communication.
[8] K.W. Reed, J.M. Owens, R.L. Carter, Circ Syst. Signal Process **4**, 157-180 (1985).
[9] M. Kostylev, P. Schrader, R. L. Stamps, G. Gubbiotti, G. Carlotti, A. O. Adeyeye, S. Goolaup, N. Singh, Appl. Phys. Lett. **92**, 132504 (2008).

6.9 Theory of parametric recovery of a microwave signal using standing spin-wave modes of a magnetic film

A.V. Chumak, A.A. Serga, and B. Hillebrands[1]

Recently [1–3], we have reported experimental results on storage and recovery of a microwave signal using a single standing spin-wave mode belonging to the discrete spin-wave spectrum, which is caused by the spatial confinement of the magnon gas in a thin yttrium-iron-garnet (YIG) ferrite film. The storage effect was realized through the conversion of the input microwave signal into a propagating magnetostatic wave (or dipolar spin wave), and, then, into an exchange-dominated standing spin-wave modes (or thickness modes) of the film. The recovery of the signal was performed by means of frequency-selective parametric amplification. The mechanism of such a restoration is highly non-trivial. Therefore, in our previous report [2] (see also [3]) we used an approximate empirical theoretical model to explain this rather complicated restoration process.

In our present report we give a detailed theoretical explanation of the restoration effect. This explanation is based on the general theory of parametric interaction of spin waves (so-called "S-theory") [4] and takes into account interactions between different groups of spin waves existing in a ferrite film. Using the developed theory we calculate parameters of the restored pulse (power, duration, and delay with respect to the input pulse) as functions of the power of the input and pumping pulses, and compared these calculated parameters with experimental data.

The experimental investigation of the effect of microwave signal restoration was described in detail in previous reports [1, 2] (see also [3]). Here we would like just to repeat shortly the main steps of the experiment. The input electromagnetic microwave pulse having a duration of 100 ns and carrier frequency of $f_{\text{in}} = 7.040\,\text{GHz}$ was converted by the input microstrip transducer into dipolar spin waves, that propagate in a long and narrow, 5 µm thick yttrium iron garnet (YIG) film. The other transducer, used to receive the output microwave signals, is placed at a distance of $l = 8\,\text{mm}$ from the input one. A bias magnetic field of $H_0 = 1706\,\text{Oe}$ is applied in the plane of the YIG film waveguide, along its width and perpendicular to the direction of the spin wave propagation, so the conditions for magnetostatic surface waves (MSSW) propagation were fulfilled. The propagating MSSW excited in the ferrite film standing (thickness) spin-wave modes that continued to exist in the film long after the propagating MSSW signal reach the output transducer. In order to recover the microwave signal stored in these standing spin-wave modes the external parallel pumping mechanism was used. To supply this double-frequency pumping pulse an open dielectric resonator was placed in the middle of the YIG waveguide. Then, during the action of the pumping pulse the restored signal appears after a certain delay at the output transducer [3] through the reversal conversation of the energy from standing spin-wave modes to the propagating MSSW.

Typical experimental oscillograms demonstrating the normalized waveforms of the restored output pulse measured for different values of the pumping power are presented in Fig. 1a. It is evident from Fig. 1a that the increase of the pumping power P_{p} leads to a significant variation of the restored pulse parameters: decrease of the recovery time t_{r} and decrease of the restored pulse duration Δt_{r}.

The mechanism governing the observed storage-and-recovery effect of a microwave signal in a ferrite film is based on existence of the crossing points of the MSSW and higher-order standing

[1] In collaboration with Prof. G.A. Melkov, National Taras Shevchenko University of Kiev, Kiev, Ukraine.

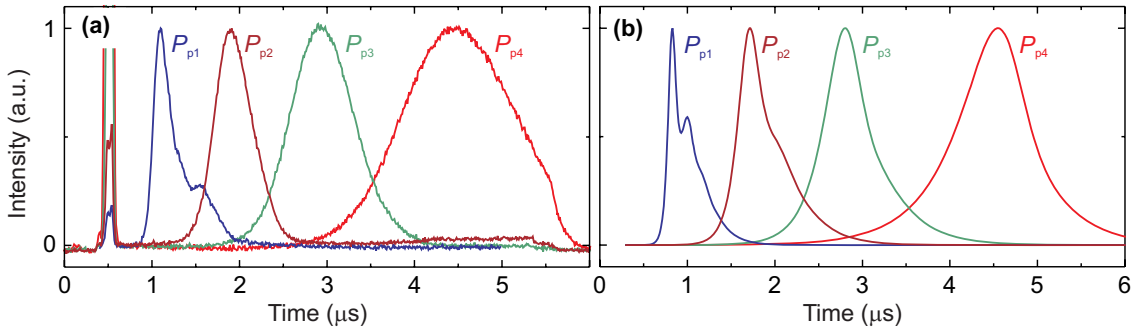

Fig. 1: Experimental (a) and calculated (b) waveforms of the delayed and recovered pulses for different values of the pumping power P_p: $P_{p1} = 3.67\,\mathrm{W}$, $P_{p2} = 1.28\,\mathrm{W}$, $P_{p3} = 0.52\,\mathrm{W}$, $P_{p4} = 0.34\,\mathrm{W}$. Waveforms are normalized to the maximum intensity of each of the recovered pulses.

spin-wave modes. Thus the dipolar hybridization of the spin-wave spectrum appears and the so-called "dipolar gaps" in the spin-wave spectrum of the film are formed [5]. As a result forward and back conversion of the propagating MSSW into a quasi-standing spin-wave mode takes place in the frequency interval near the "dipole gap".

In order to understand the signal restoration effect a qualitative model of interaction of two magnon groups with parametrical pumping was proposed in [3]. In this model we analyzed the interaction between the electromagnetic parametric pumping with effective amplitude Vh_p and frequency ω_p (where h_p is a variable pumping magnetic field, V is the parametrical coupling coefficient), standing spin-wave mode with effective amplitude characterized by the magnon number N_s and, the so-called, "dominating" spin-wave group with effective amplitude characterized by the magnon number N_κ and frequency $\omega_p/2$. The initial amplitude of standing spin-wave modes is determined by the amplitude of the applied microwave pulse and by the efficiency of energy transformation from MSSW to standing modes. So at the initial time point, when the pumping is switched on, the signal-induced standing spin-wave mode has an amplitude that is larger than the amplitude of the noise-induced dominating spin-wave group. During the period of linear amplification, the amplitudes of both wave groups exponentially increase due to the parametric amplification: the amplitude of the dominating group increases with time t as $\exp[(h_pV - \Gamma_\kappa)t]$, while the amplitude of the signal-induced standing wave group increases as $\exp[(h_pV - \Gamma_s)t]$, where $\Gamma_\kappa < \Gamma_s$ are the relaxation parameters of the dominating and standing wave groups correspondingly. Then, at some time the amplitude of the dominating wave group becames larger than the amplitude of the standing mode and reaches a certain critical value after which it starts to renormalize the effective pumping, which leads to saturation of parametric amplification. The effective pumping amplitude $h_p^{\mathrm{eff}}V$ at the saturation point becomes equal to the relaxation parameter of the dominating waves with the smallest relaxation [4]. Since $h_p^{\mathrm{eff}}V < \Gamma_s$, the amplitude of the signal-induced standing wave group starts to decrease beyond the point of pumping saturation, what results in the restored pulse generation.

In order to understand the above described effect we use the general theory of parametric interaction of spin waves (so-called "S-theory") [4]. The equation for the amplitude of a spin wave interacting with the parametric pumping can be written in the form (see also [6]):

$$\left[\frac{d}{dt} + \Gamma - i(\tilde{\omega}_k - \omega_p/2)\right] c_k - iP_k c^*_{-k} = 0 \quad , \tag{1}$$

where c_k and c^*_{-k} are the amplitudes of the signal and idle waves of frequency ω_k and wave number

k; Γ is the spin-wave relaxation parameter; $\omega_p = 2\pi f_p$ is the pumping frequency; $\tilde{\omega}_k = \omega_k + 2\sum_{k_1} T_{kk_1}|c_{k_1}|^2$ is a spin-wave frequency with account of nonlinear frequency shift, T_{kk_1} is the corresponding nonlinear parameter; $P_k = h_p V + \sum_{k_1} S_{kk_1} c_{k_1} c_{-k_1}$ is the effective internal amplitude of parametric pumping, and S_{kk_1} is the nonlinear coefficient describing four-wave interaction of spin-wave pairs.

The spin-wave formalism is substantially simplified if, instead of the individual complex amplitudes of the signal and idle waves, we introduce new variables characterizing combined amplitudes (or magnon densities per unit volume for a given wave number k) and phases of the spin-wave pairs, following [4]:

$$n_k = M_0/2(\gamma\bar{h}/)c_k c_{-k} e^{-i\psi_k}, \qquad \psi_k = \varphi_k + \varphi_{-k} \quad , \tag{2}$$

where $\gamma = 2.8\,\mathrm{MHz/Oe}$ is the gyromagnetic ratio, $\bar{h}$ is the Planck constant, and M_0 is the saturation magnetization.

In our model we analyze the existence of two magnon groups (or two effective magnon pairs): the dominating group with magnon density n_κ (note, that index κ is used to mark this dominating spin-wave group) and the signal-induced quasi-standing group of spin waves with magnon density n_s [3]. Below, we shall assume for simplicity that the coefficient of four-wave pair interaction for all the wave groups has approximately the same value $S_{kk_1} = S_{00}$, and that the effective pair phase is approximately equal for both spin-wave groups (dominating and standing) involved in the parametric interaction with pumping. Under these assumptions we can substantially simplify the expression for the amplitude of the effective pumping $P_k = h_p V + S(\sum_\kappa n_\kappa + \sum_s n_s)e^{i\psi} = h_p V + S(N_\kappa + N_s)e^{i\psi}$. Here $N_\kappa = \sum_\kappa n_\kappa$ and $N_s = \sum_s n_s$ are the total number of magnons per unit of volume for the dominating and standing spin-wave groups, correspondingly, $S = 2(\gamma\bar{h}/M_0)S_{00}$ is the renormalized coefficient of pair interaction, and $\psi = \psi_k$ is the effective phase of the collective magnon pairs. Another simplification of our model is the assumption that all the wave groups participating in the parametric interaction with pumping are always in exact parametric resonance with it (i.e. $\tilde{\omega}_k = \omega_p/2$) independently of the effective amplitude of a particular wave group.

Using all the above described simplifying assumptions, we can write the equations for the magnon densities N_i of the two wave groups (where $i = \kappa$ for the dominating spin-wave group and $i = s$ for the standing spin-wave group) and their common phase ψ in the form

$$\begin{aligned}
\frac{1}{2}\frac{dN_\kappa}{dt} &= N_\kappa[-\Gamma_\kappa + V h_p \sin\psi] \\
\frac{1}{2}\frac{dN_s}{dt} &= N_s[-\Gamma_s + V h_p \sin\psi] \\
\frac{1}{2}\frac{d\psi}{dt} &= V h_p \cos\psi + S(N_\kappa + N_s)
\end{aligned} \tag{3}$$

where $\Gamma_\kappa/(2\pi) = 0.6\,\mathrm{MHz}$, $\Gamma_s/(2\pi) = 0.69\,\mathrm{MHz}$ are the relaxation parameters for dominating and standing spin-wave groups, correspondingly. The physical meaning of the magnon densities N_κ and N_s is simple – they characterize the effective amplitude of all the spin waves that belong to a corresponding wave group.

To obtain detailed information about the temporal behavior of the magnon densities of two magnon groups we solved the system of equations (3) numerically, assuming that at the initial moment the phase ψ is the same as in the quasi-linear case $\psi = \psi^0 = \pi/2$. The initial value of the magnon density of the dominating spin-wave group is determined by the level of thermal noise existing at a

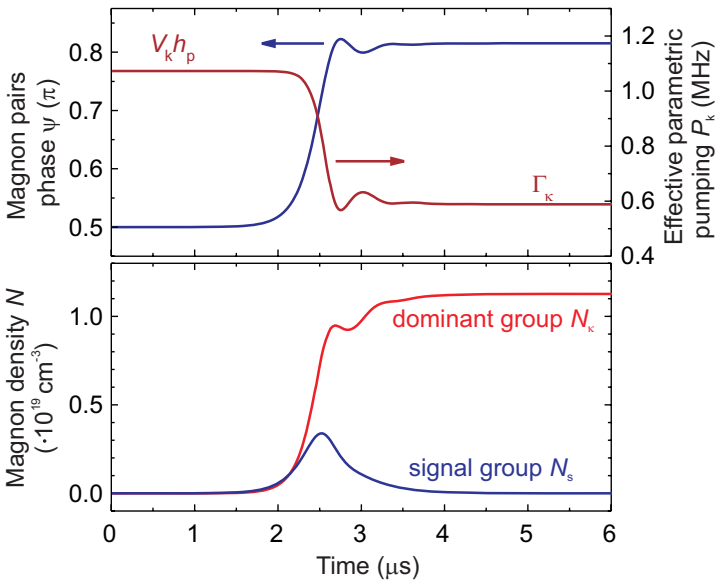

Fig. 2: Temporal evolution of the spin-wave effective phase ψ and amplitude of the renormalized effective pumping (upper frame) and temporal evolution of the magnon densities N_κ and N_s of the dominating and standing spin-wave groups (lower frame).

given temperature in a ferrite film, and can be estimated using standard methods [4]: $N_{\kappa T}|_{T=300\mathrm{K}} \approx 10^{12}\,1/\mathrm{cm}^3$. The estimation of the initial magnon density for the standing spin-wave group N_s^0 turns out to be a rather complicated task, but it is clear, that the initial magnon density N_s^0 in the standing spin-wave group must be proportional to the power of the input microwave signal $N_s^0 = K_s P_{s0}$. For the conditions of our experiment $N_s^0 = 3.6 \cdot 10^{13}\,1/\mathrm{cm}^3$.

Under the conditions of our experiment the effect of two-magnon scattering leads to partial transfer of energy from the standing spin-wave group to the dominating spin-wave group. This heating-up effect was investigated in a previous report [7] (see also [8]), where nonresonant signal restoration was investigated. Below, we shall use an approach similar to [8], and we will introduce a phenomenological coefficient β which accounts for this heating-up: $N_\kappa^0 = N_{\kappa T} + \beta N_s^0$, where $\beta = 4 \cdot 10^{-2}\,\mathrm{cm}^3$ is a phenomenological parameter describing the efficiency of two-magnon scattering. Another important feature of our model is the account of nonlinear dissipation in the standing (signal-generated) spin-wave group: $\Gamma_s = \Gamma_{s0}(1 + \eta(N_\kappa + N_s))$. The coefficient of nonlinear damping η for the conditions of our experiment was evaluated as $\eta = 1.7 \cdot 10^{-20}\,\mathrm{cm}^3$. The coefficient S of the nonlinear four-wave interaction between the pairs of excited spin waves was calculated using the expressions presented in [6] to give $S \approx 5 \cdot 10^{-13}\,\mathrm{cm}^3/\mathrm{s}$.

The results of the numerical solution of the system of equations (3) for the above specified parameters are presented in Fig. 1, Fig. 2, Fig. 3 and Fig. 4. We shall discuss below each of these figures. The temporal dynamics of parametric interaction of the two excited spin-wave with constant-amplitude pumping that was switched on abruptly at time $t = 0$ is illustrated by Fig. 2. The upper frame demonstrates the evolution of the collective spin-wave phase ψ and the amplitude P_k of the renormalized effective parametric pumping, while the lower frame of Fig. 2 illustrates the evolution of the magnon densities N_κ and N_s of the dominating and standing spin-wave groups, respectively.

The numerical results presented in Fig. 2 clearly confirm the qualitative picture of the parametric interaction describer above. In the initial time interval ($0 < t \lesssim 2.2\,\mu\mathrm{s}$) a quasi-linear parametric amplification of the both spin-wave groups takes place. In this quasi-linear regime, where the effective spin-wave phases $\psi = \pi/2$, the effective pumping is not significantly renormalized and is practically equal to Vh_p. In the stationary regime ($t \gtrsim 3.5\,\mu\mathrm{s}$) the effective pumping P_k is strongly renormalized by the excited spin waves, and is stabilized at the value $P_k = \Gamma_\kappa < Vh_p$, at which it

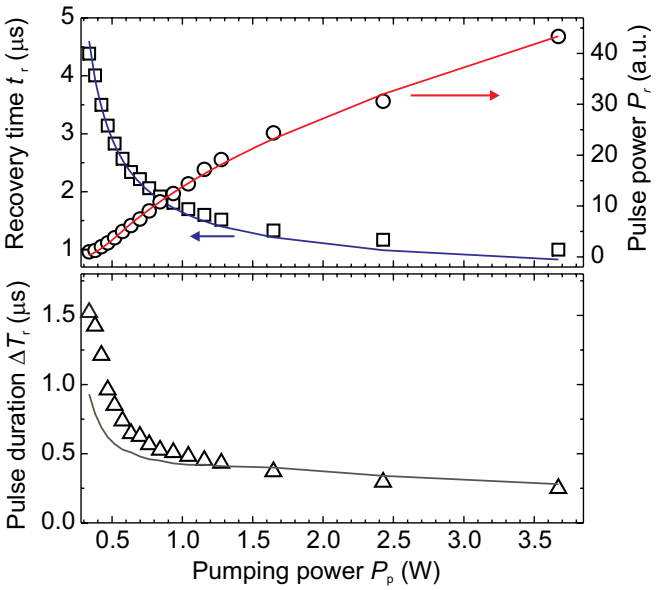

Fig. 3: Delay time (squares), peak power (open circles), and duration (triangles) of the restored pulse as functions of the pumping power. Solid lines: results of calculation. Input signal power $P_{s0} = 10\,\mu$W.

just compensates the losses of the dominating spin-wave group. In the transitional region ($2.2\,\mu s \lesssim t \lesssim 3.5\,\mu s$) the amplitude N_s of the standing spin-wave group first increases, and then begins to decrease, which results in the appearance of a finite-duration restored pulse at the output of the system. The theoretically calculated profiles of the restored output microwave pulse shown in Fig. 1b practically repeat the temporal profile of the magnon density $N_s(t)$ of the standing spin-wave group shown in the lower frame of Fig. 2.

The experimental (symbols) and theoretical (solid lines) dependencies of the peak power P_r, recovery time t_r, and duration Δt_r of the restored pulse on the pumping power P_p are shown in Fig. 3. It is evident that the increase of the pumping power P_p leads to a decrease of t_r and Δt_r, and, at the same time, to an increase of the peak power P_r of the restored signal. The above shown behavior of the restored pulse peak power can be explained by that fact that with increasing pumping power the amplification rates $\exp[(h_p V - \Gamma_\kappa)t]$ and $\exp[(h_p V - \Gamma_s)t]$ become closer and the difference in the peak amplitudes of the standing and dominating spin-wave groups becomes smaller. Thus, the amplitude of the restored pulse becomes larger. It is clear from Fig. 3 that the theoretical results for the restoration time and power of the restored pulse are in good agreement with experiment.

Using our theoretical model we also calculated the influence of the input signal power P_{s0} on the parameters of the restored microwave pulse. According to the simple analytical model presented in [3] where the increase of the input signal power results in a linear increase of the power of the restored pulse, while the recovery time should remain constant. At the same time, our experiments (see Fig. 4) clearly demonstrate that the increase of the input signal power P_{s0} leads to a decrease of the recovery time t_r and to an increase of the restored pulse power P_r, with the experimentally

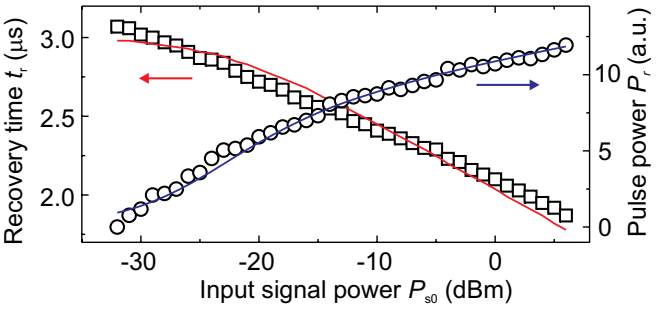

Fig. 4: Delay time (squares) and peak power (open circles) of the restored pulse as functions of the input signal power. Solid lines: results of calculation. Pumping power $P_p = 0.52\,$W.

observed increase being not linear. It is evident from Fig. 4 that our new theoretical model (3) describes the experiment rather well and, therefore, significantly improves the simple analytical model presented in [3].

In conclusion, we investigated the effect of storage and recovery of a microwave signal in a ferrite film having a discrete dipole-exchange spin-wave spectrum. An approximate (mean field) theoretical model, taking into account the competition of two spin-wave groups interacting with parametric pumping, and involving a nonlinear phase mechanism of limitation of parametrical amplification was used to describe the experimental results. The developed model provides a good qualitatively description of the experimentally observed effect of storage and recovery of microwave pulses in ferrite films.

Support by the Deutsche Forschungsgemeinschaft within the SFB/TRR 49 is gratefully acknowledged.

References

[1] A.A. Serga, A. André, S.O. Demokritov, B. Hillebrands, AG Magnetismus Annual Report, 38 (2004).
[2] A.A. Serga, A.V. Chumak, B. Hillebrands, AG Magnetismus Annual Report, 21 (2007).
[3] A.A. Serga, A.V. Chumak, A. Andre, G.A. Melkov, A.N. Slavin, S.O. Demokritov, B. Hillebrands Phys. Rev. Lett. **99**, 227202 (2007).
[4] V.S. L'vov, *Wave Turbulence under Parametric Excitations. Applications to Magnetics.* (Springer-Verlag, 1994)
[5] B.A. Kalinikos, A.N. Slavin, J. Phys. C **19**, 7013 (1986).
[6] A.G. Gurevich, G.A. Melkov, *Magnetization oscillations and waves* (CRC Press, New York, 1996).
[7] S. Schäfer, A.A Serga, A.V. Chumak, B. Hillebrands, AG Magnetismus Annual Report, 27 (2007).
[8] S. Schäfer, A.V. Chumak, A.A. Serga, G.A. Melkov, B. Hillebrands, Appl. Phys. Lett. **92**, 162514 (2008).

6.10 Probing of a parametrically pumped magnon gas with a non-resonant packet of traveling spin waves

T.M. Neumann, A.A. Serga, and B. Hillebrands

Parallel parametric pumping of spin waves is a widely used and established technique to control the magnon density in different areas of the spin-wave spectrum. It is used both in experiments on fundamental properties of magnetic excitations and for the amplification and processing of microwave signals [1–3].

Parametric pumping amplifies many different spin-wave groups simultaneously. In the process the density of spin waves is increased initially at half the pumping frequency $f_p/2$. These amplified spin waves form an overheated region of the magnon gas, which then thermalizes spreading its energy over the whole spin-wave spectrum [4]. For sufficiently long pumping, a quasi-stationary magnon gas state is created, which obeys a Bose-Einstein distribution with a concentration of magnons near the bottom of the spin-wave spectrum.

Due to the high overall density of the magnon gas spatially localized in the pumping area, the static magnetization in this region is decreased and a magnetic inhomogeneity is formed. From this *magnon barrier* [5] propagating spin waves can scatter similarly to the scattering of spin waves on a dc-current induced local magnetic inhomogeneity [6, 7]. As a consequence, the experiments performed so far on the interaction of traveling spin waves with parametric pumping had to take into account two competing effects: the pumping field, which tends to increase the spin-wave amplitude, and the magnon barrier, which decreases it via scattering.

We investigate the effects of the magnon barrier on the amplitude of a traveling spin-wave by using *non-resonant* spin-wave pulses with a frequency $f_s \neq f_p/2$ in order to eliminate any direct interaction with the applied external pumping field.

In addition, we measure the spin-wave phase. It is known that this phase shift is of crucial importance for the amplification by non-adiabatic localized parametric pumping [5, 8]. Our measurements have shown that the additionally accumulated phase is more sensitive to the barrier characteristics than the amplitude at intermediate to high pump power. Since these regimes are of interest both for applied and fundamental studies (e.g. for the generation of Bose-Einstein condensates), a major part of the work is devoted to the investigation of the spin-wave phase.

By measuring the pure scattering of the spin-wave amplitude on the magnon barrier as well as the phase accumulation of the spin wave when propagating through the pumped region, physically relevant characteristic properties of the magnon barrier can be obtained. We illustrate the potential of probing a parametrically generated magnon gas with non-resonant propagating spin-wave packets by estimating the magnon density in the pumped area based on a simple model.

A schematic view of the experimental setup is shown in Fig. 1a. The microwave source “1” generates a cw-signal at $f_s = 6.82\,\mathrm{GHz}$. A triggered microwave switch transforms this signal into a $8\,\mu\mathrm{s}$ long microwave pulse, which is sent to an input transducer placed across a $7.8\,\mu\mathrm{m}$ thick and $1.5\,\mathrm{mm}$ wide yttrium-iron-garnet (YIG) sample. Due to the chosen geometry, the microwave signal excites a packet of so called backward volume spin waves, which propagate with a wave vector $k = 150\,\mathrm{cm}^{-1}$ parallel to the applied bias magnetic field $H = 1750\,\mathrm{Oe}$. An output antenna $8\,\mathrm{mm}$ away from the input antenna picks up the spin-wave pulse after it has passed through the film.

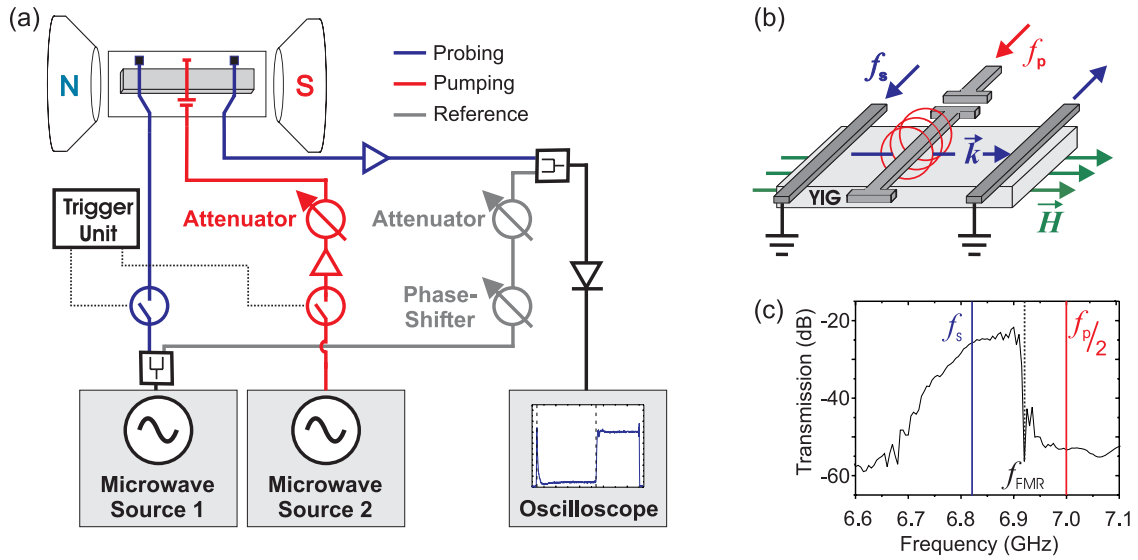

Fig. 1: (a) Sketch of the experimental setup. (b) Experimental section. (c) Microwave transmission characteristics.

A 50 µm-wide microstrip resonator half-way between the two microstrip transducers (see Fig. 1b) allows effective, local parametric pumping. The microwave source "2" drives the resonator with a 5 µs long pump pulse at a frequency $f_p = 14.00\,\mathrm{GHz}$. Note that there is a discrepancy of $\delta f = f_p/2 - f_s = 180\,\mathrm{MHz}$ by which the resonance condition for direct amplification of the propagating spin waves is *not* fulfilled. The applied pump power P can be varied up to 80 W. In order to avoid overheating of the sample at such high powers a repetition rate of 2 ms is chosen.

The transmission characteristics presented in Fig. 1c show that the frequency of the pump pulse is above the frequency of ferromagnetic resonance f_{FMR}, which makes sure that, first, the pumping threshold is low [9] and, second, no propagating backward volume spin waves are amplified. Simultaneously, the carrier frequency of the traveling spin-wave packet is slightly below f_{FMR}, which guarantees good excitation and detection properties via the microstrip antennas. The signal received at the output antenna can interfere with a phase-locked reference signal before detection and observation in order to reconstruct its phase [10].

The measured pulse shapes for different applied pump powers are shown in Fig. 2a. We note three things: First of all, no signal amplification takes place since the propagating spin wave is non-resonant with the external pumping. Secondly, the spin-wave signal is suppressed when the pump pulse is applied. Thirdly, the suppression increases monotonically with increasing pump power. In particular, almost complete signal suppression is achieved already at intermediate pump powers of 20 W. This suppression does not happen instantaneously when the pump pulse is switched on, but takes up to 2 µs to reach a stationary regime.

The observed suppression is understood as the result of scattering on the magnon barrier. With increasing pump power, the scattering increases together with the magnon barrier. As the magnon barrier is created during the thermalization of magnons excited at half the pumping frequency, a relatively slow passage into the stationary regime is expected.

Figure 2b shows the measured phase profiles of the output pulse relative to the reference pulse. As for the transmitted intensity, the accumulated phase slowly approaches a stationary value. This stationary phase depends monotonically on the applied pumping power. However, if we compare the corresponding curves we note that the phase does not seem to saturate even at high powers.

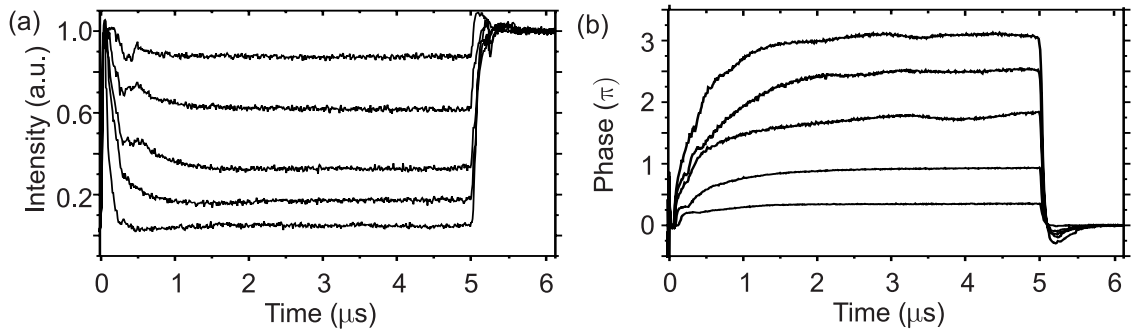

Fig. 2: (a) Transmitted signal shapes for different pump powers. (b) Phase profiles for different pump powers.

We give a very simple, phenomenological model to describe the observed phase of the propagating spin-wave in the stationary regime:

Due to the pumping, the magnon density in the area around the pumping resonator is increased. This leads to a small reduction δM of the magnetization M from its initial value $M_s$which changes the wave vector of the propagating spin wave. The difference between the undisturbed and disturbed wave vector integrated over the spin-wave propagates distance gives the accumulated phase observed in the experiment.

We start by simplifying the problem as follows: First of all, the interaction is assumed to be confined to a region of length l around the central pumping resonator labeled II in Fig. 3a. Outside of this region we suppose that no additional phase is accumulated. Moreover, let us take the magnetization reduction δM in region II as constant and independent of the position. As a consequence we get

$$\phi = \int \Big(k(M_s) - k(M) \Big) dx = \Big(k(M_s) - k(M) \Big) \cdot l. \tag{1}$$

In the first-order approximation, the dependence of wave vector on the magnetization of the sample is given by

$$k(M) = k(M_s) + c_1 \cdot \delta M, \tag{2}$$

where $c_1 > 0$ is a constant which can be calculated from the dispersion law. For the experimental conditions considered here, $c_1 = 18.3\,(\mathrm{cmOe})^{-1}$.

The change in magnetization δM is due to the increased magnon density. Every single parametrically generated magnon decreases the magnetization by the product of the spin Landé g-factor and one Bohr magneton $g \cdot \mu_B$, so that the overall reduction is given by

$$\delta M = -g \cdot \mu_B \cdot \frac{N}{V} \quad , \tag{3}$$

where N denotes the number of magnons created by the pump and $V = l \cdot w \cdot d$ is the volume of the pump region.

Combining Equations (1), (2) and (3) yields

$$\phi = \frac{c_1 \cdot g \cdot \mu_B \cdot l}{V} \cdot N \quad , \tag{4}$$

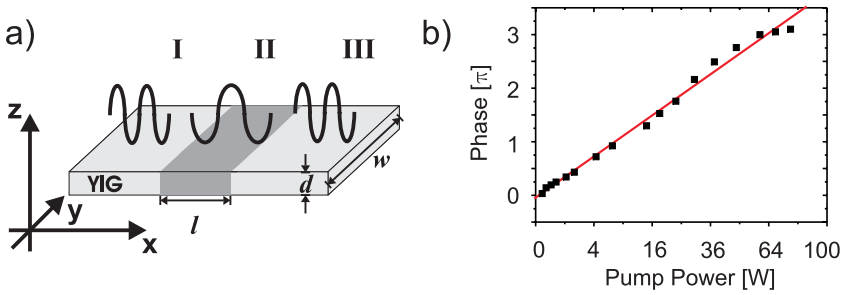

Fig. 3: (a) Illustration of the presented model of a confined, homogeneous pumping region. (b) Black dots indicate the experimental results, the red line shows the fit obtained with the presented model.

which means that in this linear model the accumulated phase is directly proportional to the number of excited magnons. In particular, we note that the length l of the pump region II drops out of the equation.

To complete the analysis let us consider the dependence of N on the applied pump power. Note that in first-order approximation, an applied pumping field above the threshold value should lead to an exponential increase of the spin-wave amplitude with time. The fact that a stationary amplitude is observed is due to limiting mechanisms, most notably the phase mechanism which reduces the effective coupling of the pumping field with the parametric magnons.

According to [11], the stationary spin-wave number for a given wave vector including the phase mechanism is given by

$$\begin{aligned} N &= \frac{1}{S}\sqrt{(h_x V_{coupl})^2 - \omega_r^2} \\ S &= \frac{1}{4}\left(\frac{\omega_M}{\omega_P}\right)^2\left(\sqrt{\omega_P^2+\omega_M^2} - \omega_M + \gamma N_x M_s\right) \\ \omega_M &= \gamma\, 4\pi M_s \end{aligned} \tag{5}$$

where h_x is the pumping magnetic field in the direction of the bias magnetic field, V_{coupl} is the coupling coefficient, ω_r is the relaxation frequency and N_x the demagnetization factor. The pumping magnetic field is proportional to the square root of the pumping power

$$h_x \sim \sqrt{P} \quad , \tag{6}$$

where the proportionality factor depends on the geometrical properties of the pumping resonator.

Combing Equations (4), (5) and (6) finally yields

$$\phi = \frac{c_1 \cdot g \cdot \mu_B \cdot l}{V \cdot S}\sqrt{c_2 P - \omega_r^2} \approx \frac{c_1 \cdot g \cdot \mu_B \cdot l}{V \cdot S}\sqrt{c_2 P}$$

with c_2 a constant depending on the properties of the resonator and the coupling of the spin waves to the external pumping field. The last approximation is justified for pump powers not too close to the pumping threshold, which is the case in our experiments.

As Fig. 3b shows, the presented model with the single free parameter c_2 fits the experimental data well.

From the experimentally observed accumulated phase we can calculate

$$N = 2.7 \cdot 10^{13} \cdot \phi, \qquad \frac{N}{V} = 1.2 \cdot 10^{19}\ \mathrm{cm}^{-3} \cdot \phi$$

where we have estimated $l = 0.2\,\mathrm{mm}$ [12] to obtain the density of parametrically pumped magnons. We note, that the later value agrees well with expected values for the magnon density of $10^{18} - 10^{19}\,\mathrm{cm}^{-3}$ [9, 13].

In conclusion, we have measured the transmission and phase accumulation of non-resonant spin waves propagating through a parametrically generated magnon barrier. From the accumulated phase the absolute number of magnons constituting the barrier was deduced and the total magnon density was estimated.

Overall, the method of probing the total density of a parametrically controlled magnon gas by the phase of a non-resonant traveling spin wave possesses great potential due to its time-resolution and high sensitivity. It is applicable to thin magnetic materials, e.g. thin magnetic films, where techniques based on other physical effects fail.

Financial support by the Matcor Graduate School of Excellence and the DFG within the SFB/TRR 49 is gratefully acknowledged.

References

[1] C. Patton, M. Wu, K. R. Smith, V. I. Vasyuchka, Ferroelectrics **342**, 101 (2006).
[2] G. A. Melkov, V. I. Vasyuchka, A. V. Chumak, A. N. Slavin, J. Appl. Phys. **98**, 074908 (2005).
[3] S. O. Demokritov, V. E. Demidov, O. Dzyapko, G. A. Melkov, A. A. Serga, B. Hillebrands, A. N. Slavin, Nature **443**, 430 (2006).
[4] V. E. Demidov, O. Dzyapko, S. O. Demokritov, G. A. Melkov, A. N. Slavin, Phys. Rev. Lett. **99**, 037205 (2007).
[5] A. A. Serga, T. Schneider, B. Hillebrands, M. P. Kostylev, A. N. Slavin, Appl. Phys. Lett. **90**, 022502 (2007).
[6] M. P. Kostylev, A. A. Serga, T. Schneider, T. Neumann, B. Leven, B. Hillebrands, R. L. Stamps, Phys. Rev. B **76**, 184419 (2007).
[7] V. E. Demidov, U. H. Hansen, S. O. Demokritov, Phys. Rev. B **78**, 054410 (2008).
[8] S. O. Demokritov, A. A. Serga, V. E. Demidov, B. Hillebrands, M. P. Kostylev, B. A. Kalinikos, Nature **426**, 159 (2003).
[9] A. G. Gurevich G. A. Melkov, *Magnetization Oscillation and Waves* (CRC Press, Inc., 1996).
[10] A. A. Serga, T. Schneider, B. Hillebrands, S. O. Demokritov, M. P. Kostylev, Appl. Phys. Lett. **89**, 063506 (2006).
[11] V. E. Zakharov, V. S. L'vov, S. S. Starobinets, Sov. Phys. Usp. **17**, 6 (1974).
[12] G. A. Melkov, A. A. Serga, A. N. Slavin, V. S. Tiberkevich, A. N. Oleinik, A. V. Bagada, JETP **89**, 1189 (1999).
[13] G. A. Melkov, Yu. V. Kobljanskyj, O. Dzyapko, Ukr .Fiz. Zhurn. **50**, A5 (2005).

6.11 Generation of dipolar spin-waves due to disintegration of a condensate of photon coupled exchange magnons

V.I. Vasyuchka, C.W. Sandweg, A.A. Serga, and B. Hillebrands[1]

The recent discovery of Bose-Einstein condensation in a parametrically driven magnon gas [1] stimulates the growing interest to different aspects of interaction of electromagnetic parametric pumping with magnetic media (see e.g. [2, 3]). Questions concerning the behavior of the medium after the pumping is switched off define the especially interesting problem of pumping-free evolution of a non-equilibrium magnon gas [4].

It is known that in the process of first-order parametric interaction, which is realized in the case of longitudinal parametric pumping when pumping and bias magnetic fields are collinear, one photon of frequency 2ω generates two magnons of frequency ω [5]. The phase-correlated groups of the magnon pairs having equal frequency and magnitude, but antiparallel wave vectors $\mathbf{q}' = -\mathbf{q}$ constitute a condensate of photon coupled magnon pairs. In such a condensate the interactions between magnon pairs (rather than the interaction between individual magnons) play an important role in the collective behavior. The strength of this interaction grows with increasing pair density during the pumping action. Four-magnon nonlinear processes satisfying the following condition

$$\omega(\mathbf{q}_1) + \omega(-\mathbf{q}_1) = \omega(\mathbf{q}_2) + \omega(-\mathbf{q}_2) \tag{1}$$

without taking the spin waves out of parametric resonance are crucial here. Such processes retain phase correlations within each parametrically excited pair of magnons and lead to a self-consistent change of the total phase of magnons in each pair. As a result, a phase shifted longitudinal microwave magnetic field generated by the magnon condensate partially compensates the external pumping. This decreases the energy flux from the pumping source to the spin-wave system and leads to the limitation on the condensate density [6]. Moreover, in the case of moderate pumping powers the net pumping field can support only one magnon pair group in the condensate. It is the so called dominating group having the lowest damping [2].

Disintegration of the condensate after switching off the external pumping is accompanied by an instantaneous rise of the internal longitudinal magnetic field of frequency 2ω [7]. Here, we present the first observation of the energy transfer in the magnon gas caused by this internal pumping.

The schematic diagram of the microwave experimental setup is shown in Fig. 1. The experiment was performed using an yttrium-iron-garnet (YIG) film sample ($30 \times 2.5\,\mathrm{mm}^2$) of $5\,\mu\mathrm{m}$ thickness. The sample was placed near the end of a shorted microstrip transmission line of $50\,\mu\mathrm{m}$ width. A bias magnetic field $\mathbf{H}_0$ was applied in plane of the YIG film across the microstrip. The microstrip was simultaneously used as a pumping field inductor and as a spin-wave antenna.

A rectangular pumping pulse of $15\,\mu\mathrm{s}$ duration with carrier frequency of $2\omega = 2\pi \cdot 14\,\mathrm{GHz}$ was supplied to the microstrip line through a frequency splitter. A stub tuner was used to maximize the amplitude of the external pumping field. Rise and fall times of the pumping pulse were about $4\,\mathrm{ns}$.

Microwave signals, which could be potentially irradiated by the YIG sample in a frequency range from 2 to $8\,\mathrm{GHz}$, were picked up by the same microstrip and redirected by the frequency splitter to the receiving part of the setup. It consists of a precise attenuator, low noise amplifier, resonant

[1] In collaboration with Prof. G.A. Melkov, National Taras Shevchenko University of Kiev, Kiev, Ukraine.

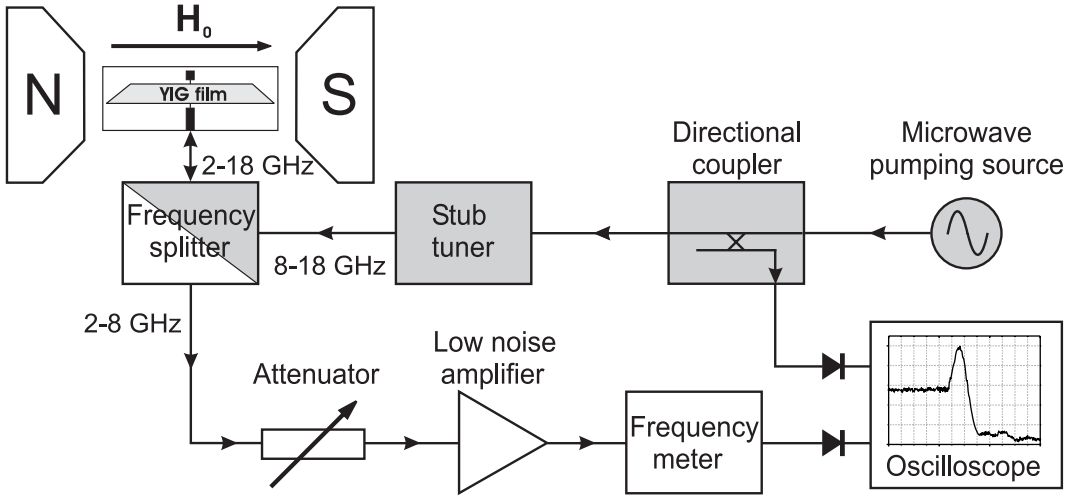

Fig. 1: Schematic diagram of the microwave experimental setup.

frequency meter, and microwave detector. The time profile of the irradiated signal was visualized with an oscilloscope.

The normalized signal waveform observed for $H_0 = 1748\,\mathrm{Oe}$ at half of the pumping frequency is shown in Fig. 2. In this case the pumping power of $P_\mathrm{p} = 63\,\mathrm{mW}$ is three times higher than the threshold of parametric instability. Note that the minimal threshold of parametric instability $P_\mathrm{p} = 3.2\,\mathrm{mW}$ was reached for $H_0 = 1738\,\mathrm{Oe}$ when frequency ω was equal to the frequency of ferromagnetic resonance.

The waveform in Fig. 2 can be divided into two parts. The first one includes the initial increase and saturation of the irradiated signal in the course of the pumping action. Since the signal profile here corresponds well with the theoretically predicted behavior of the magnon pair condensate this signal part can be directly associated with the dominant magnon group. Because the relatively wide and long microstrip antenna cannot receive the spin waves with $k \sim 10^5\,\mathrm{cm}^{-1}$ [5] one can assume that dipole-exchange magnons of the dominating group are coupled with long-wave spin-wave modes by means of two-magnon scattering.

The second and most interesting signal part is the sharp peak at the end of the signal. This peak appears *after* the pumping pulse is switched off. It is clear that it is not caused by an increase of the absolute number of magnons. Thus, only energy redistribution between different parts of the

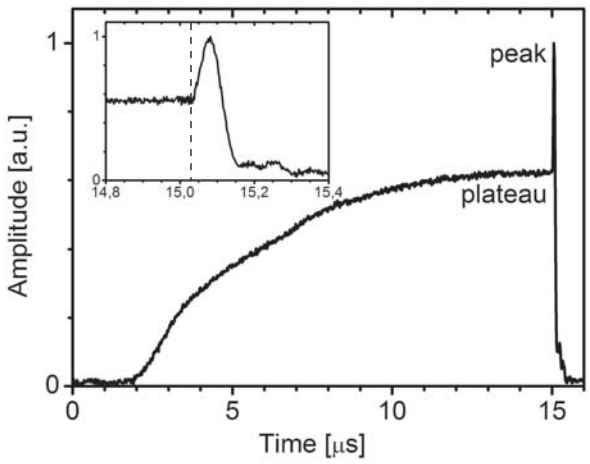

Fig. 2: Time profile of the signal irradiated from the YIG film at half of the pumping frequency $\omega/2\pi = 7\,\mathrm{GHz}$. The bias magnetic field and applied pumping power are 1748 Oe and 63 mW, respectively. The vertical dashed line indicates the moment when pumping is switched off.

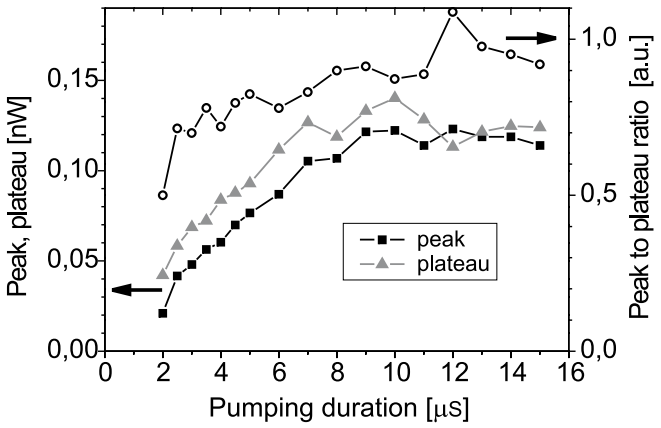

Fig. 3: Dependencies of the plateau power (see Fig. 2) and the difference between peak and plateau powers on pumping duration. The circles indicate the ratio between the above curves.

magnon spectrum can occur. We interpret the appearance of the peak as a result of the parametric generation of long-wave spin-wave modes by a non-compensated internal field, which acts as a pump. The dipolar spin waves have a higher threshold of parametric instability in comparison to magnons from the dominating group [5]. Therefore, at the time when the pumping pulse is being applied, the value of the effective net pumping is smaller then it is necessary for generation of the dipolar spin waves. However, a much larger internal pumping field appears immediately after the external pumping is switched off. Due to the fast thermalization [4] of the dominating group this field exists during a small time interval and is able to generate only a short macroscopic signal. Its relaxation frequency calculated from the time profile of the peak is around 3 MHz. This value is in good accordance with the relaxation frequency of longitudinal magnetization reported in Ref. [7].

Assuming the above interpretation we conclude that the amplitude of the non-compensated internal field and therefore the intensity of the peak should correlate with intensity of the dominating group. Such correlation is clearly visible in Fig. 3. One can see the saturation of the peak power after 10 μs because the phase limits the density of the magnon pair condensate.

Support by the Deutsche Forschungsgeminschaft within the SFB/TRR 49 is gratefully acknowledged.

References

[1] S.O. Demokritov, V.E. Demidov, O. Dzyapko, G.A. Melkov, A.A. Serga, B. Hillebrands, A.N. Slavin, Nature **443**, 430 (2006).
[2] A.A. Serga, A.V. Chumak, A. Andre, G.A. Melkov, A.N. Slavin, S.O. Demokritov, B. Hillebrands, Phys. Rev. Lett. **99**, 227202 (2007).
[3] A.A. Serga, T. Schneider, B. Hillebrands, M.P. Kostylev, A.N. Slavin, Appl. Phys. Lett., **90**, 022502 (2007).
[4] V.E. Demidov, O. Dzyapko, S.O. Demokritov, G.A. Melkov, A.N. Slavin, Phys. Rev. Lett. **100**, 047205 (2008).
[5] A.G. Gurevich, G.A. Melkov, *Magnetization oscillations and waves*, CRC Press, New York (1996).
[6] V.S. L'vov, *Wave Turbulence under Parametric Excitations. Applications to Magnetics.*, Springer-Verlag, (1994).
[7] V.S. Zhitnyuk, G.A. Melkov, Sov. Phys. JETP **48**, 884 (1978).

C. Magnetic Films of Heusler Compounds

6.12 Exchange constant in Co_2-based Heusler compounds

J. Hamrle, O. Gaier, S. Trudel, B. Hillebrands[1]

The exchange constant describes the strength of the exchange interaction inside a ferromagnetic material. It is therefore an important parameter from both fundamental and application points of view. For example, the knowledge of the exchange constant is needed in *ab-initio* and micromagnetic calculations. Here, we present the exchange constant of various Co_2-based Heusler compounds, which we have determined using Brillouin light scattering (BLS) spectroscopy. In the following, we first present the results of BLS studies performed on Co_2FeSi thin films, and highlight the determination of the exchange constant of this compound. Then, we provide an overview of the exchange constant of various Co_2-based Heusler compounds. In particular, a comparison between our determined values for Co_2-based Heusler compounds and the exchange constants of 3*d* metals and alloys (such as Fe_xCo_{1-x}) is presented.

The Co_2FeSi samples investigated here consists of an Al(4 nm)/Co_2FeSi(*d*)/Cr(30 nm)/ MgO(001) epitaxial structure. Co_2FeSi films with thicknesses *d* of 20 and 60 nm were deposited by pulsed laser deposition using an excimer laser with a wavelength $\lambda = 248$ nm. The same technique was also used for the deposition of the Cr buffer and the protective Al capping layers. Following deposition, the films were annealed at 450°C. Analysis of x-ray diffractograms indicates that Co_2FeSi adopts $L2_1$ atomic ordering, as is confirmed by the observation of $\{111\}$ reflections. The BLS measurements were performed in the magneto-static surface mode geometry, *i.e.* the magnetic field *H* was applied parallel to the film surface and perpendicular to the plane of light incidence. A diode pumped, frequency doubled Nd:YVO_4 laser with a wavelength $\lambda = 532$ nm was used as the light source.

Figure 1 summarizes BLS spectra collected for the Co_2FeSi sample with 60 nm thickness. The Damon-Eshbach (DE) and two perpendicular standing spin-wave (PSSW) modes are clearly re-

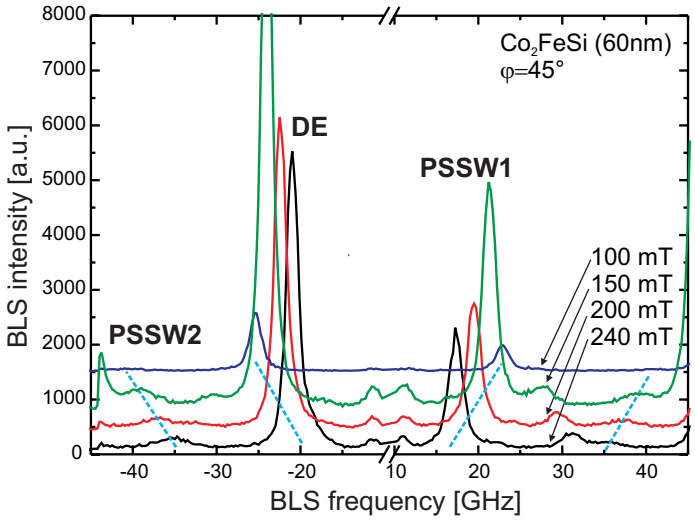

Fig. 1: (color) BLS spectra of a Co_2FeSi film with 60 nm thickness recorded at a transferred wave vector $q_{\parallel} = 1.73 \cdot 10^7\,\mathrm{m}^{-1}$ ($\vartheta = 45°$) and different magnetic fields.

[1] In collaboration with M. Jourdan, H. Schneider, G. Jakob, G. Fecher, C. Felser, Johannes-Gutenberg-Universität Mainz, Germany; J. Kübler, Technische Universität Darmstadt, Germany; T. Kubota, Y. Sakuraba, M. Oogane, Y. Ando, Tohoku University, Japan.

solved. Note that the peak appearing at approximately 30 GHz in Fig. 1, whose frequency decreases with increasing magnetic field, does not correspond to a spin-wave mode. It is rather a second-order transmission artefact peak of the Damon-Eshbach mode which arises due to the finite finesse of the Fabry-Perot interferometer.

The results of numerical calculations performed for Co_2FeSi samples are shown in Fig. 2. The BLS frequencies were calculated as a function of (a) the external magnetic field H, (b) the film thickness d, and (c) the angle of incidence φ. In all cases, the best agreement between the experimental data and the calculations was achieved with a value for the exchange constant of $A = 31.5 \pm 1.0$ pJ/m (exchange stiffness $D = 715 \pm 20$ meV Å^2). The corresponding values of the saturation magnetization and the Landau g-factor are $\mu_0 M_S = 1.28$ T ($M_S = 1020$ kA/m, $\mu = 4.93\,\mu_B$/f.u.) and $g = 2.0$, respectively. As is discussed in the following, the exchange stiffness of Co_2FeSi is extraordinarily large. In particular, it is larger than the exchange stiffness of Fe and Co metals, and nearly as large as the exchange stiffness reported for $Co_{47}Fe_{53}$ (800±50 meV Å^2) [1], which is (to the best of our knowledge), the largest exchange stiffness constant known.

Figures 3 and 4 provide a comparison between several properties (saturation magnetization M_S, exchange stiffness D, exchange constant A, Curie temperature T_C, and the number of valence electrons per atom N_v) associated to a variety of Co_2-based Heusler compounds, 3d-metals, and intermetallic alloys (a particular emphasis is put on Fe_xCo_{1-x} compounds). Note that these are experimental data collected from our own work and various third-party publications. Therefore, the investigated parameters (*i.e.* T_C, M_S, A, and D) were determined by different research groups, on different sample sets, with no common preparation method. Not surprisingly, this results in some scattering of the data. However, some clear trends emerge, which will be discussed below.

Figure 3a shows the dependence of M_S on N_v. As expected, the curve follows the well known Slater-Pauling rule. It reaches a maximum saturation magnetization 2.5 μ_B/atom, obtained for Fe_xCo_{1-x}, where x is approximately 65–70% [2]. The saturation magnetization of Heusler compounds linearly scales with N_v. Note that this trend has previously been observed (see, for example, Ref. [3]).

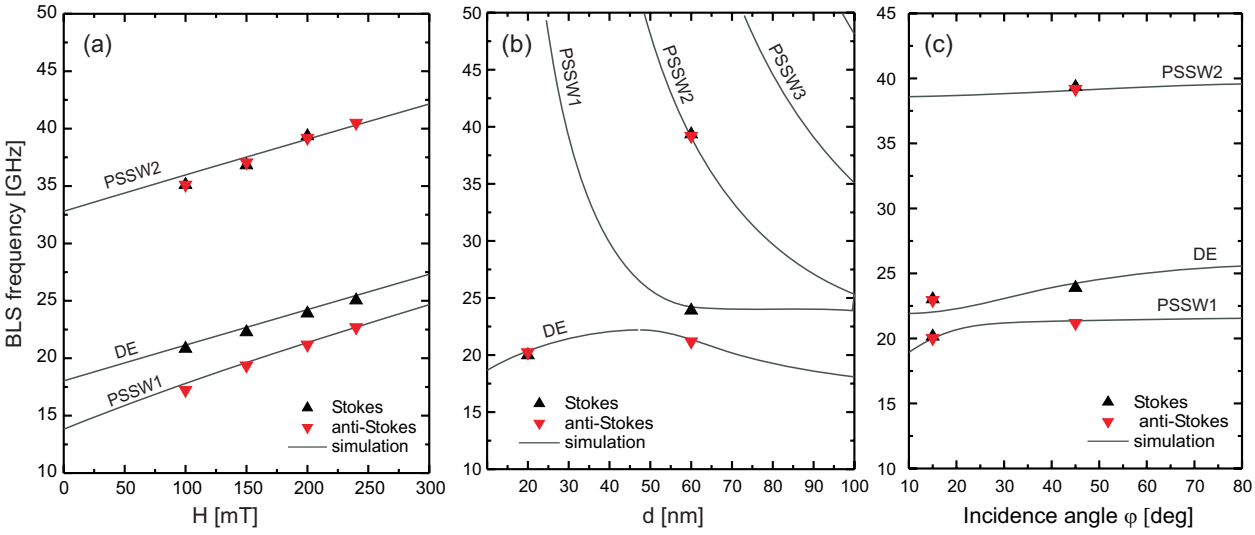

Fig. 2: Numerical simulations (solid lines) of experimental BLS frequencies (triangles up and down) collected for Co_2FeSi calculated for exchange constant $A = 31.5$ pJ/m, saturation magnetization $\mu_0 M_S = 1.28$ T and Landau g-factor $g = 2.0$, respectively. (a), (b) and (c) show the dependence of BLS frequencies on the external magnetic field H, the angle of incidence φ, and the film thickness d, respectively.

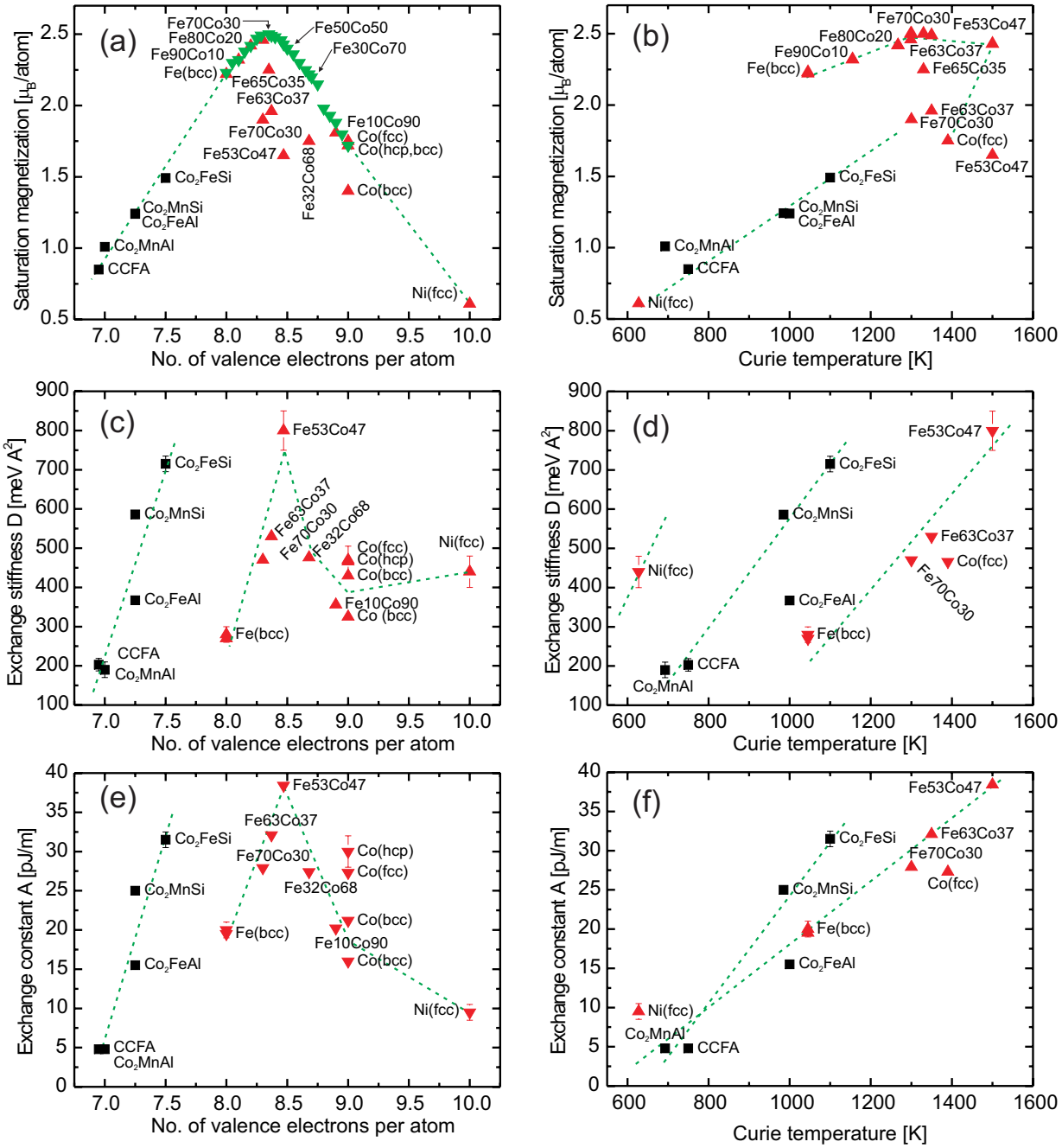

Fig. 3: Saturation magnetization M_S in bulk, exchange stiffness D and exchange constant A as a function of number of valence electrons N_v and Curie temperature T_C for investigated Co_2-based Heusler compounds and some 3*d*-metals, particularly Fe_xCo_{1-x} compounds. Values of M_S and N_v are averages given per atom. Straight lines are guides to the eye.

The dependence of M_S on T_C is shown in Fig. 3b, which constitutes an update to a previously published compilation [3]. This figure shows that the M_S of Co_2-based Heusler compounds scales linearly with T_C. The saturation magnetization of Fe_xCo_{1-x} (for $x \geq 70\%$) also scales linearly with T_C, with a maximum T_C of 1500 K reached at $x \sim 50\%$ [2]. Note that this value is determined by the extrapolation of $M(T)$, as $Fe_{50}Co_{50}$ undergoes a $\gamma \rightarrow \alpha$ phase transformation before reaching the Curie temperature [4]. Also note that for Fe_xCo_{1-x}, the composition related to the maximal Curie temperature ($Fe_{70}Co_{30}$) does not correspond to the composition providing the maximal value of the saturation magnetization ($Fe_{50}Co_{50}$).

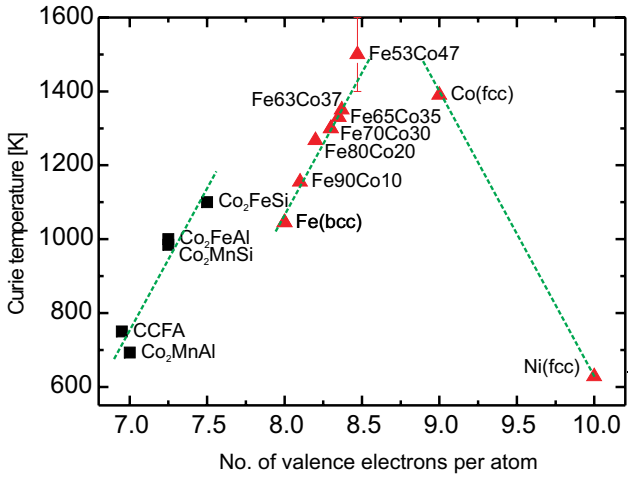

Fig. 4: Dependence of the Curie temperature on the number of valence electrons per atom for the investigated Co_2-based Heusler compounds and some 3-d metals and compounds. The dashed lines are guides to the eye.

The dependence of the exchange stiffness D on N_v and on T_C is shown in Fig. 3c, 3d. In both cases, Co_2-based Heusler compounds exhibit a roughly linear dependence of D on both N_v and T_C, reaching its maximum value for Co_2FeSi ($D = 715 \pm 20\,\text{meV Å}^2$). Also note the very large change in D between Co_2FeSi and $Co_2Cr_{0.6}Fe_{0.4}Al$ and Co_2MnAl (both $\sim 200\,\text{meV Å}^2$). Such a large change is associated with the introduction of only 0.5 valence electron per atom. Fe_xCo_{1-x} also provides a roughly linear dependence between D and N_v in the x range of 50–100%, reaching its maximum value of $D = 800 \pm 50\,\text{meV Å}^2$ with $Fe_{53}Co_{47}$ [1]. This shows that our determined value for Co_2FeSi is extraordinarily large. It is larger larger than D of pure Fe or Co, and nearly as large as the maximum value of D obtained for the Fe_xCo_{1-x} series. To the best of our knowledge, the exchange stiffness of Co_2FeSi is only surpassed by $Fe_{53}Co_{47}$. Such an extraordinary value of Co_2FeSi is very surprising, taking into account that one quarter of the constituent atoms is a non-magnetic element (Si). Finally note that the slopes of $D(N_v)$ for both Co_2-based Heusler compounds and for Fe_xCo_{1-x} are the same, but the linear curves are shifted by one valence electron per atom in N_v. This is probably due to the fact that the non-magnetic atom serves as a donor of an electron for Fe or Mn in the Co_2-based Heusler compounds, thereby increasing the strength of the exchange interaction in the compound [3].

The dependence of the exchange stiffness D on T_C (Fig. 3d) also shows a linear dependence for both Co_2-based Heusler and Fe_xCo_{1-x} compounds. In the case of Fe_xCo_{1-x}, compounds throughout the x range fall roughly on the same line. Furthermore, it seems that both linear trends (for the Heusler and Fe_xCo_{1-x} compounds) roughly intersect at $T_C = 0\,\text{K}$. Such an observation would be consistent with the expected linear dependence between D and T_C [5].

Figures 3e, 3f show the dependence of the exchange constant A on N_v and on T_C. Since A is proportional to D ($A = DM_S/(2g\gamma_0\hbar)$, where g is the Landau g factor, $\hbar$ is the reduced Plank constant and $\gamma_0 = e/(2m_e)$ is the gyromagnetic ratio [6]), the behavior of A is very similar to that of D, as already discussed in the previous paragraphs. The values of A for Heusler compounds differ by a factor of 6 between Co_2MnAl and Co_2FeSi. For Fe_xCo_{1-x}, the maximal value of A is again obtained for $Fe_{50}Co_{50}$, and is greater than for Co_2FeSi. Also, for $A(N_v)$, the shift between the linear dependence for Co_2-based Heusler compounds and for Fe_xCo_{1-x} is now found to be about 0.8 valence electrons per atom. In the case of $A(T_C)$, we again observe a linear increase of A on T_C for both systems. However, the slope for Heusler compounds is much larger than in the case of Fe_xCo_{1-x}.

Finally the relationship between T_C and N_v is shown in Fig. 4. We again bind a linear dependence between T_C and N_v for both Heusler compounds and Fe_xCo_{1-x}. In this case, the shift between both linear dependence is about 0.5 valence electrons per atom.

In conclusion, we have found an extraordinary large exchange stiffness in Co_2FeSi, which is nearly as high as the record exchange of $Fe_{47}Co_{53}$. The careful comparison between exchange strength in Co_2-based Heusler compounds shows several similar features, such as a linear dependence of D on N_v or T_C. On the other hand, those dependencies are shifted in N_v, reflecting different electronic states of Fe and Co in the Co_2-based Heusler compounds compared with 3*d* metals.

References

[1] X. Liu, R. Sooryakumar, C.J. Gutierrez, G.A. Prinz, J. Appl. Phys. **75**, 7021 (1994).
[2] J.M. MacLaren, T.C. Schulthess, W.H. Butler, R. Sutton, M. McHenry, J. Appl. Phys. **85**, 4833 (1999).
[3] G.H. Fecher, H.C. Kandpal, S. Wurmehl, C. Felser, G. Schönhense, J. Appl. Phys. **99**, 08J106 (2006).
[4] T. Fukuda, M. Yuge, T. Terai, T. Kakeshita, J. Phys: Conf. Ser. **51**, 307 (2006).
[5] J. Stöhr, H.C. Siegmann, *Magnetism – From fundamentals to nanoscale dynamics*, Springer, Heidelberg, (2006).
[6] J. Hamrle, O. Gaier, S.-G. Min, B. Hillebrands, Y. Sakuraba, Y. Ando, submitted to J. Phys: Condens. Matter, (2008), arXiv:0810.0834.

6.13 Tailoring of structural, magnetic, and electronic properties of Co_2MnSi thin films by He^+-irradiation

O. Gaier, J. Hamrle, and B. Hillebrands[1]

Both theoretical and experimental investigations show that a high degree of order in Heusler compounds is an essential precondition in order to obtain the desired 100 % spin polarization of these materials [1, 2]. For fabrication of thin Heusler films, annealing at high temperatures is a conventional way to introduce a well-ordered phase. The high temperature annealing, however, very often results in the interdiffusion at interfaces deteriorating the half-metallic property. This problem might be overcome using the irradiation with keV He^+ ions to evoke the ordered state. A successful application of the He^+ ion irradiation has been previously reported for the binary FePt system [3, 4]. The present work is devoted to the question of whether the ion irradiation technique is also applicable to the much more complex Heusler compounds.

The irradiation experiments have been carried out on the (001)-oriented Co_2MnSi films of 30 nm thickness. To ensure equal initial conditions for all irradiation experiments a single $1\,in^2$ Co_2MnSi sample was prepared, which was cut into $5 \times 5\,mm^2$ pieces before the irradiation. The fabricated sample consisted of an epitaxial Al(1.3 nm)/Co_2MnSi(30 nm)/Cr(40 nm)/MgO(001) structure and was deposited at the Tohoku University, Japan by means of inductively coupled plasma assisted magnetron sputtering. The Co_2MnSi samples were exposed to different fluences of 30 keV He^+ ions which were varied between 10^{14} and $10^{16}\,ions/cm^2$. The irradiation was carried out at ambient temperature at the Forschungszentrum Dresden-Rossendorf. The effect of 30 keV He^+ irradiation on the ordering properties of the Co_2MnSi thin films was studied by X-ray diffraction (XRD) in combination with X-ray absorption and circular magnetic dichroism (XAS/XMCD) and photoemission spectroscopy at high energies (HAXPES). The XRD measurements were carried out at the Tohoku University, Japan, whereas both the XAS/XMCD and HAXPES investigations were performed in collaboration with the Johannes Gutenberg University of Mainz at BESSY II, Berlin and SPring-8, Japan, respectively.

The results of XRD investigations are summarized in Fig. 1. The insets (a) and (b) show the θ-2θ-scan and the pole figure of the fundamental (220) reflections of the as-deposited Co_2MnSi film. The four-fold symmetry of the (220) equivalent reflections (inset (b)) demonstrates the epitaxial growth of the Co_2MnSi layer. A clear (200) peak in the θ-2θ diffraction pattern (inset (a)) and absence of the (111) reflections in the corresponding pole figure scan (not shown here) suggest the B2 order of the prepared film. A detailed analysis of the recorded θ-2θ diffraction pattern reveals furthermore that the ratio of the (200) and (400) integrated intensities is lower compared to the results of simulations performed under the assumption of a complete B2 structure. Therefore, it is concluded that a certain amount of the A2 type of disorder was present in the fabricated Co_2MnSi film. After the ion bombardment, the values of I_{200}/I_{400} increase for the fluences of $1 \cdot 10^{14}$ and $5 \cdot 10^{14}\,ions/cm^2$. This result clearly suggests a qualitative improvement of the B2 order in the Co_2MnSi samples irradiated with He^+ ions at these particular fluences. However, the transition to the $L2_1$ ordered phase could not be induced by the exposure of the films to the ion beam.

[1] In collaboration with H. Schneider, M. Kallmayer, P. Pörsch, G. Schönhense, H.J. Elmers, Institut für Physik, Johannes Gutenberg-Universität Mainz; J. Fassbender, Forschungszentrum Dresden-Rossendorf, Dresden; A. Gloskovskii, C.A. Jenkins, G.H. Fecher, C. Felser, Institute of Inorganic and Analytical Chemistry, Johannes Gutenberg-Universität, Mainz; E. Ikenaga, SPring-8 JASRI, Hyogo, Japan; Y. Sakuraba, S. Tsunegi, M. Oogane, Y. Ando, Tohoku University, Sendai, Japan.

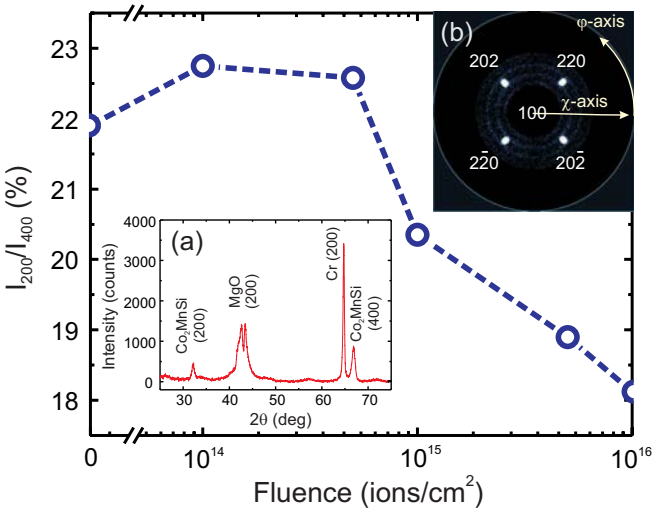

Fig. 1: Ratio of the (200) and (400) integrated XRD intensities in dependence of the applied ion fluence. An increase at $1 \cdot 10^{14}$ and $5 \cdot 10^{14}$ ions/cm^2 is clearly visible. The insets show (a) the θ-2θ-scan of the as prepared MgO / Cr(40 nm) / Co_2MnSi(30 nm) / Al(1.3 nm) film and (b) the corresponding pole figure of the fundamental (220) reflections.

The improvement of chemical order inside the Co_2MnSi layer introduced by the irradiation with He^+ ions is further supported by the XAS/XMCD results, which are summarized in Fig. 2. Figure 2a shows XAS data recorded at the Co $L_{2,3}$ edge for irradiated and non-irradiated samples. This figure reveals a satellite peak at 3.8 eV above the L_3 absorption edge, whose intensity directly correlates with the degree of ordering inside the Co_2MnSi layer [5]. Subtracting the linear background and fitting the peaks (inset of Fig. 2a), the intensity of this feature was determined for samples irradiated with He^+ ions at different fluences. The results are presented in Fig. 2b and show that at fluences of $1 \cdot 10^{14}$ and $5 \cdot 10^{14}$ ions/cm^2 the intensity of the satellite peak increases with respect to the non-irradiated sample. This suggests, in agreement with the results of XRD characterization, that in this particular range of applied fluences the local order in the bulk of Co_2MnSi films is increased after the irradiation. For higher fluences, however, the intensity of the satellite decreases indicating an increasing level of disorder introduced by the ion bombardment beyond 5×10^{14} ions/cm^2.

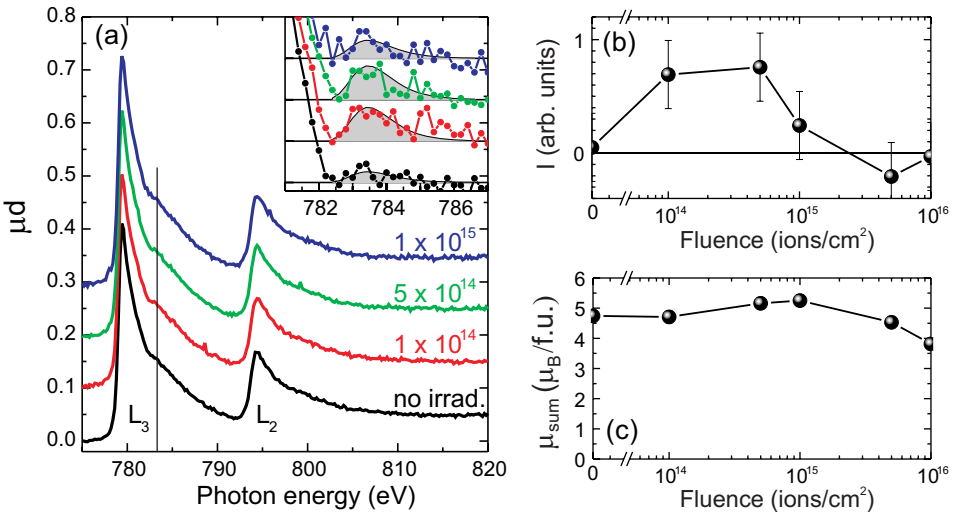

Fig. 2: (a) Transmission XAS spectra at the Co $L_{2,3}$ absorption edge from Co_2MnSi films irradiated with 30 keV He^+ ions at the indicated fluences. The inset shows the energy range of the Co satellite peak after linear background subtraction together with a fit of the peak area. (b) Dependence of the intensity of the satellite peak on the He^+ ion irradiation. (c) Saturation magnetization of Co_2MnSi films irradiated with 30 keV He^+ ions at different fluences.

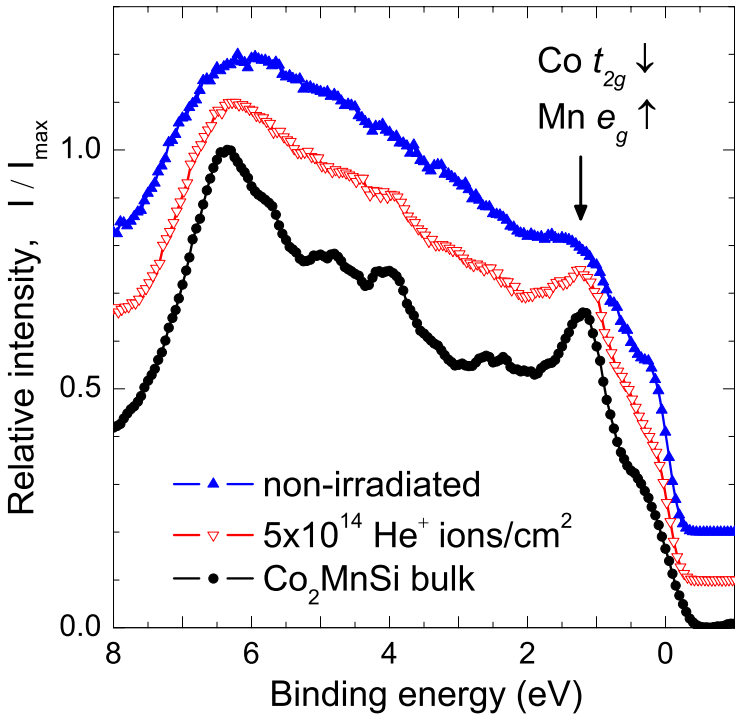

Fig. 3: HAXPES ($h\nu = 7.94$ keV) spectra of Co_2MnSi films irradiated with 30 keV He^+ ions in comparison to a non-irradiated sample and a cleaved Co_2MnSi bulk sample. The enhanced intensity of Co and Mn *d*-states at about 1.3 eV, characteristic for bulk Co_2MnSi, is marked by an arrow.

Using a sum rule analysis, the element-specific magnetic moments per 3*d*-hole were determined from the XAS/XMCD spectra, and the saturation magnetization of the investigated Co_2MnSi films was calculated. The latter results are presented in Fig. 2c as a function of the applied ion fluences. The saturation magnetization increases up to a fluence of $1 \cdot 10^{15}$ ions/cm^2 and reaches the value of $5\,\mu_B$/f.u., which is theoretically predicted for the well-ordered Co_2MnSi bulk. The magnetization decreases for fluences beyond $1 \cdot 10^{15}$ ions/cm^2. This behavior is confirmed by the results of SQUID measurements (not shown here) and provides a further hint for the improvement of chemical order effected inside the Co_2MnSi layer by the irradiation with He^+ ions.

The HAXPES valence band spectra are shown in Fig. 3, comparing the non-irradiated film and the bulk reference sample with the sample irradiated at the optimum fluence of $5 \cdot 10^{14}$ ions/cm^2. The valence band spectrum of the non-irradiated film has a wide maximum in the energy range from about 7 eV to 0 eV without distinct features. The pronounced peak of the *d*-states at about 1.3 eV below the Fermi level, which is well resolved in the valence spectrum of the bulk sample, is largely smeared out, pointing to the presence of disorder in the sample. After irradiation, the valence band spectrum of the thin film resembles much more closely that of the bulk material, providing clear evidence of the structural improvement of the Co_2MnSi film after the irradiation.

In summary, the above results of XRD, XMCD and HAXPES investigations demonstrate that the He^+ irradiation technique has the potential to create local chemical order in Co_2MnSi and other related half-metallic Heusler compounds without the need of high-temperature annealing. Further studies are in progress combining the irradiation with a mild annealing, which avoids the problem of interdiffusion.

The project was financially supported by the Research Unit 559 *"New materials with high spin polarization"* funded by the Deutsche Forschungsgemeinschaft and by the NEDO International Joint Research Grant Programm 2004/T093.

References

[1] S. Picozzi, A. Continenza, A.J. Freeman, Phys. Rev. B **69**, 094423 (2004).
[2] Z. Gercsi, K. Hono, J. Phys.: Condens. Matter **19**, 326216 (2007).
[3] D. Ravelosona, C. Chappert, V. Mathet, H. Bernas, Appl. Phys. Lett. **76**, 236 (2000).
[4] H. Bernas, J.Ph. Attané, K.-H. Heinig, D. Halley, D. Ravelosona, A. Marty, P. Auric, C. Chappert, Y. Samson, Phys. Rev. Lett. **91**, 077203 (2003).
[5] N.D. Telling, P.S. Keatley, G. van der Laan, R.J. Hicken, E. Arenholz, Y. Sakuraba, M. Oogane, Y. Ando, T. Miyazaki, Phys. Rev. B **74**, 224439 (2006).

D. Applied Research and Technology

6.14 New approach to the k-vector sensitivity of the BLS technique

C.W. Sandweg, V.I. Vasyuchka, A.A. Serga, and B. Hillebrands

An important step towards the understanding of the behavior of magnon gases and condensates in thin magnetic films requires the information of the exact spectral positions of spin-wave excitations through the simultaneous experimental recognition of their frequencies and wave vectors. For the investigation and characterization of energy transfer processes initiated in a magnon gas by parametric excitation an instrument is needed that can detect and resolve the whole range of magnon wave vectors from $10^2\,\mathrm{cm}^{-1}$ to $10^5\,\mathrm{cm}^{-1}$. It has been demonstrated in [1] that this range is accessible by means of Brillouin Light Scattering (BLS) spectroscopy. However, despite a wide-range wave-vector sensitivity no wave vector resolution was possible in this work.

Several approaches have been developed in recent years for the measurement of wave numbers in BLS experiments. In most of these efforts diaphragms placed in the beam of inelastically scattered light were used to select the appearing wave vectors components. The upper limit of the in-plane wave vector component that has been detected in these attempts is about $4 \cdot 10^4\,\mathrm{cm}^{-1}$ [2–4].

However, the detection of spin waves with higher wave vectors is crucial for the study of topics of current interest, such as the observation of strongly correlated magnon states. A promising approach is to vary the angle of incident light with respect to the orientation of the sample. Wave vectors up to $2 \cdot 10^5\,\mathrm{cm}^{-1}$ can be detected in such a configuration when probing light with a wavelength of 532 nm is used. The feasibility of such a technique for the characterization of spin-wave modes, where the wave vectors are oriented perpendicular to the bias magnetic field in a laterally structured ferromagnetic film has already been shown [5].

Here we report on a distinct improvement of this approach through its expansion from one to two dimensions. With our new setup spin-wave wave vectors oriented both parallel and perpendicular to the external field can be resolved and measured.

Figure 1 shows the experimental setup. In order to satisfy the demands of long-term stability of the bias magnetic field, and of a strong bias field in a relatively large gap between its poles we have used two permanent magnets (“NdFeB”) mounted on each side (hatched area) of the yoke, which is prepared from specially treated iron (“vacofer S1”). In addition, a brass frame has been made to stabilize the yoke and allow one to attach small iron bars parallel to the poles. These iron bars partially redirect the magnetic flux and effectively control the magnetic field in the gap.

A holder positions the sample between the two poles of the yoke. For precise positioning of the sample, a small x-y-z stage is used. This sample is mounted on a freely pivotable lever. The angle between the lever and the incident beam of light may be set by two different methods. In the first, the lever is manually turned and affixed to a wheel marked with an angle scale. Alternatively, a stepper motor mounted on the other side of the lever can be used for positioning. For both methods, the resolution is 0.5° or better. The control of this angle allows us to investigate the in-plane components of wave vectors oriented perpendicular to the biased field.

The main advantage of this setup is the possibility to investigate magnetic excitations with the wave vectors oriented parallel to the bias magnetic field. For this reason the whole setup (including the magnet) is placed on top of a rotation stage (resolution is better than 0.1°). By changing the

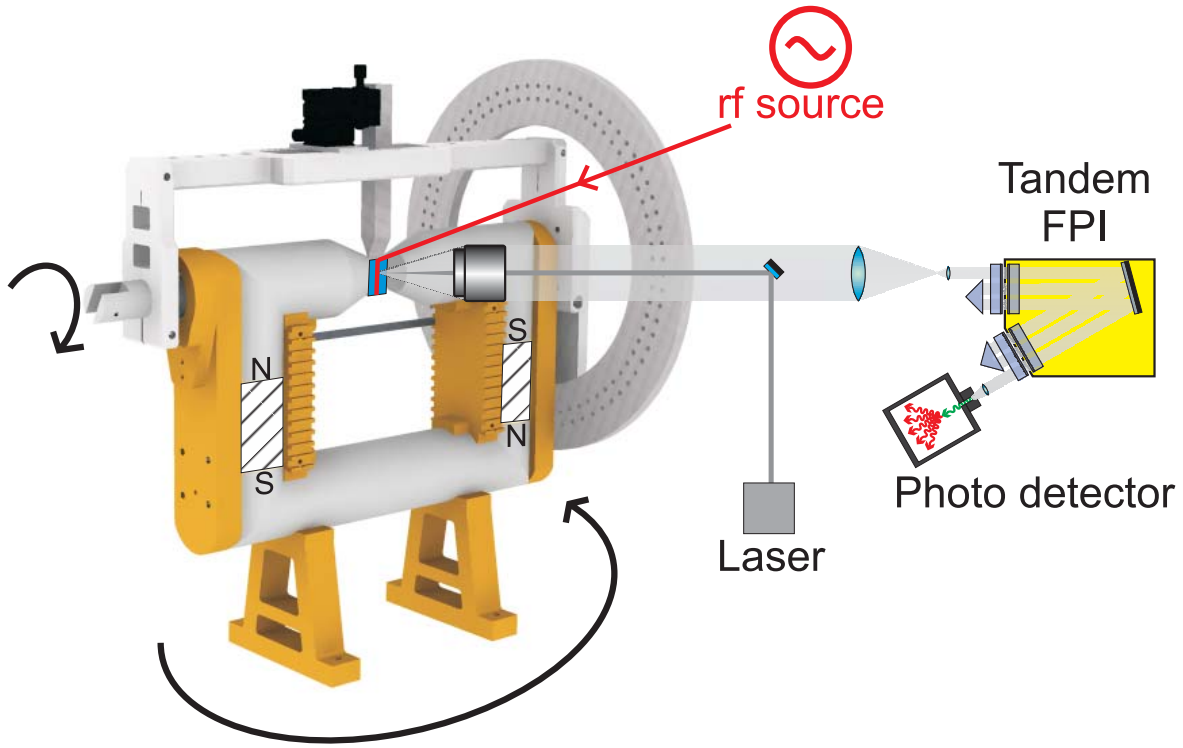

Fig. 1: Experimental setup. The yoke is composed of two permanent magnets (hatched area) and specially treated iron in order to create a high magnetic field between the poles. The sample is positioned using a sample holder on a fully pivotable lever. The spin-wave wave vectors oriented perpendicular and parallel to the bias field can be selected by turning the lever and by rotating the whole setup, respectively.

horizontal angle between the setup and the probing light beam the parallel wave vector components can be measured without changing the magnetization of the sample.

The inelastically scattered light is directed to the tandem Fabry-Perot Interferometer (FPI) and after frequency selection detected by the photodetector.

In order to evaluate the wave-vector selectivity of this setup we have measured both longwave dipolar dominated backward volume magnetostatic spin waves (BVMSW) excited near ferromagnetic resonance frequency, and short-wave dipolar-exchange magnons at the lowest energy state of the magnon gas.

The BVMSW were directly excited by a 200 µm wide microstrip antenna located under a 7.4 µm thick ferrite film sample. The antenna was driven by a microwave signal with a frequency of 7.36 GHz. The bias magnetic field was 1980 Oe. As one sees in Fig. 2a, in the BVMSW case the maximum value of intensity of the inelastically scattered light can be clearly identified at $0\,\mathrm{cm}^{-1}$. This is due to the fact that the chosen frequency is near the ferromagnetic resonance and a consideration of the dispersion relation (see Fig. 2b) suggests that only spin waves with very small wave vectors are excited.

Figure 2 also shows the first measurement of wave numbers of the magnons at the lowest energy state, i.e. at the bottom of the spin-wave spectrum (see the gray dots). The magnons were injected to the lowest energy state at 5.65 GHz, due to the effect of kinetic instability when the energy of the parametrically pumped magnon group, having frequency near the half of the pumping frequency, is transmitted to the bottom of the spin-wave spectrum as a result of four magnons conversion [6]. In order to satisfy the energy and momentum conservation laws for this process, a parametric pump-

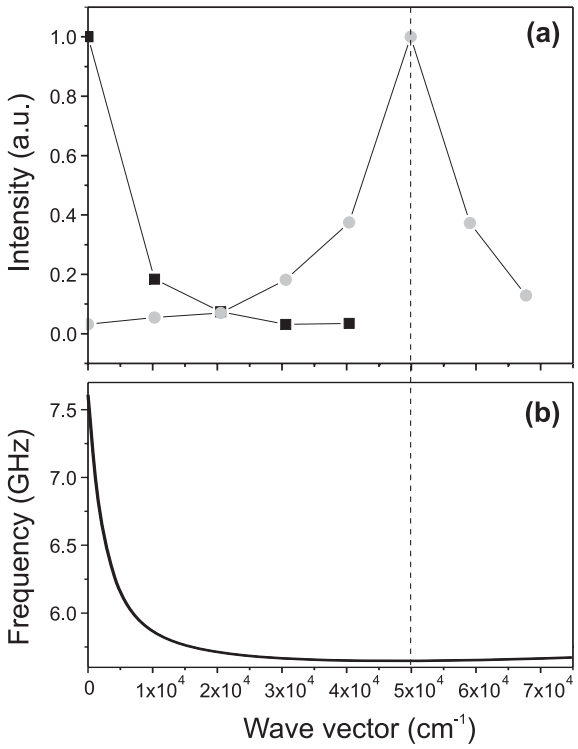

Fig. 2: (a) - Measured BLS intensities as a function of the wave number. The investigated YIG film has a thickness of 7.4 µm. The squares show the results for directly excited spin waves at 7.36 GHz near the ferromagnetic resonance, and the gray dots correspond to the lowest energy states of the parametrically driven magnon gas. (b) - Dispersion relation of spin waves with wave vector oriented parallel to the applied field of 1980 Oe.

ing frequency of 14 GHz was chosen. The magnetic pump field, oriented along the direction of the bias field, was induced in the yttrium iron garnet film by the same 200 µm wide microstrip antenna, mentioned above. It is clearly visible that in perfect accordance with theoretical predictions, the highest intensity of inelastically scattered light coincides with the minimum of the spin-wave dispersion curve at $5 \cdot 10^4\,\mathrm{cm}^{-1}$.

Support by the Deutsche Forschungsgemeinschaft within the SFB/TRR49 is gratefully acknowledged.

References

[1] S.O. Demokritov, V.E. Demidov, G.A. Melkov, A.A. Serga, B. Hillebrands, A.N. Slavin, Nature **443**, 430 (2006).
[2] V.N. Venitskiĭ, V.V. Eremenko, E.V. Matyushkin, JETP Lett. **27** 239 (1978).
[3] W.D. Wilber, W. Wettling, P. Kabos, C.E. Patton, W. Jantz, J. Appl. Phys. **55**, 2533 (1984).
[4] C. Mathieu, V. Synogatch, C.E. Patton, Phys. Rev. B **67**, 8 (2003).
[5] S.O. Demokritov, B. Hillebrands, A.N. Slavin, Phys. Rep. **348**, 442 (2001).
[6] S. Lutovinov, G.A. Melkov, A.Yu. Taranenko, V.B. Cherepanov, Sov. Phys. JETP **95**, 760 (1989).
[7] V.S. L'vov *Wave Turbulence under Parametric Excitations. Applications to Magnetics.* Springer (1994).
[8] A.G. Gurevich, G.A. Melkov *Magnetization Oscillations and Waves.* CRC Press (1996).

6.15 Phase sensitive BLS spectroscopy with magneto-optical modulator

F. Fohr, A.A. Serga, J. Hamrle, and B. Hillebrands

Space- and time-resolved Brillouin light scattering (BLS) spectroscopy is a well established technique to investigate the spin-wave dynamics in thin magnetic films. However, this method is based on a simple counting of inelastically scattered photons and thus only allows for the spatial and temporal mapping of spin-wave intensities. No phase information about magnetic excitations is accessible by conventional BLS technique. At the same time the phase information is crucial to answer questions concerning problems such as formation of coherent states in a magnon gas and evolution of nonlinear spin-wave eigenmodes [1] as well as nonlinear phase accumulation [2], peculiarities of spin-wave excitation process [3], 2-dimensional phase structure of spin-wave beams in magnetically anisotropic media, etc..

Moreover, the implementation of phase resolution into Brillouin light spectroscopy not only leads to a complete picture of the underlying physical processes by combining space-, time- and phase-resolution into the measurement, but also improves the BLS dynamical range as reported in this article. Especially phase-sensitive BLS microscopy can be interesting for the investigation of small magnetic structures, such as lateral structures.

The first realization of a phase-sensitive BLS setup as well as the results obtained by means of phase-sensitive BLS spectroscopy have been presented by us in Ref. [2–4]. Here we report on a further improvement of this technique by implementation of a new type of optical modulator, based on Brillouin light scattering in a thin ferrite film.

To understand the principle of phase sensitivity it is important to notice that the inelastically scattered light, which is used in the BLS measurements, contains both amplitude and phase information of the scattering spin wave. However, the phase information is lost when the photon is received by a photo-detector. To access this information we use interference between two portions of inelastically scattered light created in the process of propagation of probing laser beam through an magneto-optical modulator and the investigated sample. The mode of operation is shown in Fig. 1. The modulator is driven by the same microwave signal which is used to excite the spin waves. This guarantees not only that the reference light has exactly the same frequency as the inelastically scattered light but also the necessary phase coherence between both signals. Amplitude and phase of the reference signal can be influenced by using a microwave attenuator and a phase shifter. Since the signal and the reference channel share the same spatial path, thermal and mechanical stability is ensured.

The resulting interference picture allows us to visualize the phase fronts and to calculate the phase profiles (i.e. the time-dependent phase difference between the exciting microwave signal and the spin wave at any given point) of the investigated spin waves from measured interference maps with different additional phase shifts between reference and signal. For a more detailed description of the underlying analysis procedure and the phase-sensitive BLS setup see Refs. [3, 4].

The magneto-optical modulator used here was produced on the base of an yttrium-iron-garnet (YIG) ferrite film. As one can see in Fig. 1 the laser beam is initially focused on a 10 µm thick in-plane magnetized YIG film stripe in magneto-optical modulator. The bias magnetic field is oriented parallel to the spin-wave propagation direction, and thus a backward volume magnetostatic spin wave (BVMSW) is excited in the film. As a result of nonelastic light scattering by this wave a

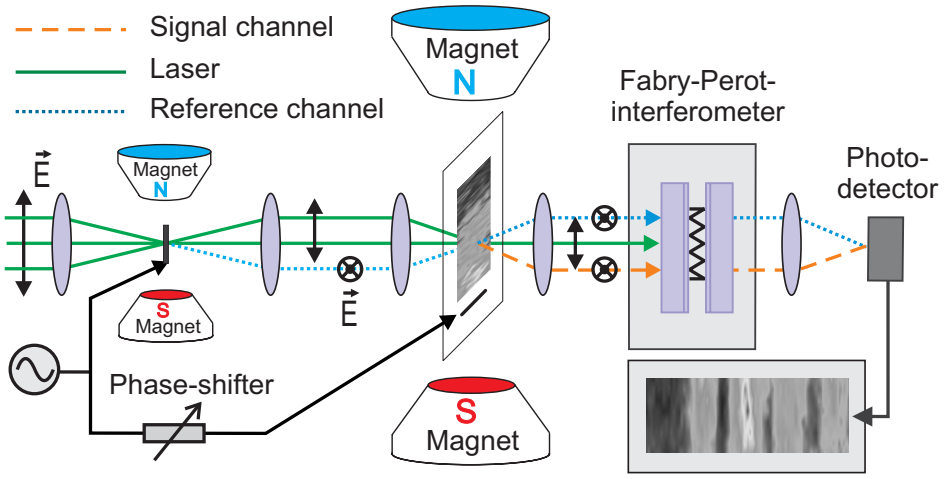

Fig. 1: Experimental setup: phase resolved BLS. Phase sensitivity is created by interference between the light inelastically scattered by the spin waves (dashed line) and a coherent reference beam (dotted line), frequency shifted and turned in polarization by the magneto-optical modulator.

part of the beam is now frequency shifted and simultaneously rotated in polarization forming the reference beam. Focussing of the laser beam is necessary to enhance the efficiency of the scattering process. Firstly the beam is focussed near to the exciting antenna, where the intensity of the spin wave and scattering-probability is highest and secondly, most of the scattered light is collected by the second lens.

Note that a great part of the laser light passes the modulator unchanged in frequency and polarization. Some part of this undisturbed light undergoes a second scattering process in the sample and forms the sample beam. Having the same polarization direction and the same frequency, the reference beam and the sample beam now fulfill the condition for interference at the photo-detector.

Before the implementation of the *magneto*-optical modulator, the necessary frequency shift for the reference beam was created by using an *electro*-optical modulator based on a lithium-niobate crystal [4]. However phase-resolved BLS spectroscopy using magneto-optical modulation has several advantages compared to electro-optic-modulation.

In order to increase the conversion efficiency, the lithium-niobate-crystal in our electro-optical modulator was placed inside a microwave cavity. Due to the strong distortion of the electric field inside the cavity by influence of this dielectric ($\varepsilon = 40$) material, the adjustment of the modulator was very complicated and as a result only a few fixed frequencies were accessible. This restriction does not exist for a magneto-optical modulator which can be tuned continuously in frequency by an external magnetic field. Thus, the RF-frequency can be implemented as an additional free parameter during a measurement.

Another important advantage of a magneto-optical modulator, which is based on Brillouin light scattering, is that the polarization of the reference beam and the sample beam is the same. On contrary, the electro-optical modulator does not change the polarization of the frequency-shifted light and as a result no interference with non-elastically scattered light occurs without special disalignment of the polarization filter placed before the interferometer. In conventional BLS spectroscopy this filter is used to block the elastically-scattered light and thus consequently decreases the optical noise. In this way the disalignment of the filter allows interference but also significantly increases the noise level. This disalignment is not necessary for a magneto-optical modulator, where the polarization condition for the best interference is fulfilled automatically.

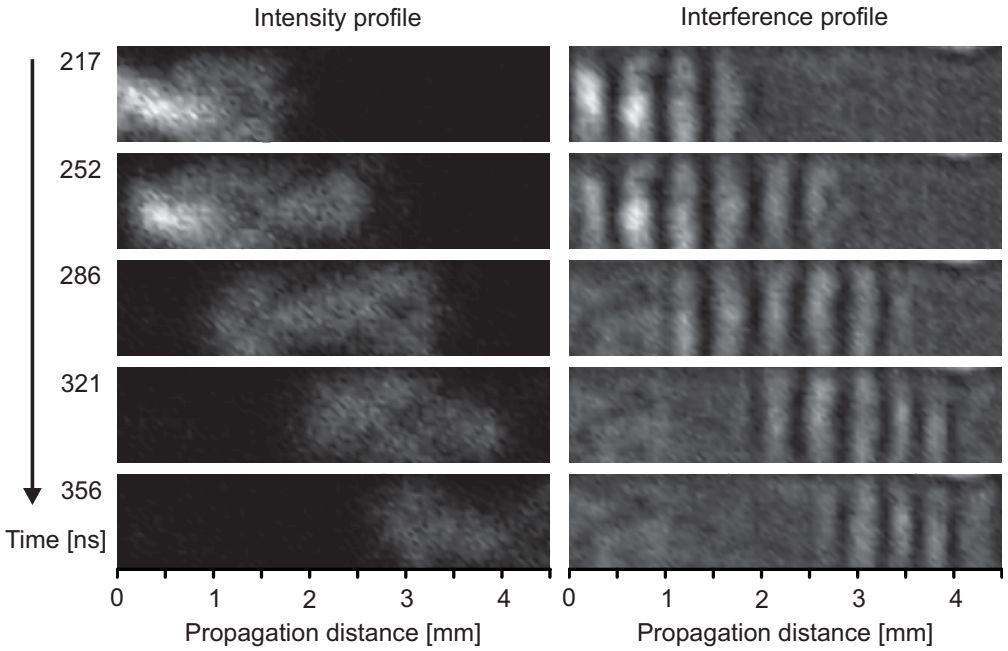

Fig. 2: Phase resolved measurement of a propagating spin- wave packet using a magneto-optical modulator. The first column is obtained with the conventional space- and time-resolved Brillouin light scattering setup and shows two-dimensional maps of the spin-wave intensity distribution for given times. The right column shows the corresponding interference patterns. The carrier frequency is 7 GHz and the applied field H_0 is $1.44 \cdot 10^5$ A/m (1815 Oe). The intensity in each profile is normalized to the respective maximum value at 217 ns.

In the following we present the first measurements with the new setup. Figure 2 shows the comparison between the intensity and the interference pattern of a propagating spin-wave pulse in a 4.5 mm long YIG-film also in BVMSW-configuration. The first column shows the decaying intensity of the spin-wave packet propagating in the sample. The intensity data is obtained by switching out the exciting microwave-current in the modulator. In the second column the interference pattern of the sample-beam and reference beam is depicted. It is clearly observable that for the long propagation times, the spin wave is much more visible in the interference patterns in comparison to the intensity profiles. Thus an increasing in the dynamic range of the BLS setup is obtained.

The contrast of the phase profiles can be additionally improved by subtracting the background in the interference patterns. Note, that signal intensity E_s^2 and reference intensity E_r^2 combine to $E_s^2 + 2E_sE_r\cos(\varphi) + E_r^2$ with a phase shift of φ, which can be adjusted with a phase shifter (see Fig. 1). In this equation the pure reference component E_r^2 adds no information about the spin wave itself and can be regarded as background. The contrast can be improved by just subtracting the intensity profile of the reference beam from the interference profile: $E_s^2 + 2E_sE_r\cos(\varphi)$. To get the information about spatial and temporal distribution of the background, for each point of the two-dimensional scan an additional reference pulse was recorded with a delay of 900 ns. Figure 3 shows the result of the calculation. Spurious signals, e.g. the spot at the upper right corner, which originates from defects and optical non nonuniformities in the YIG-film, are completely erased from the interference pattern and distribution of the spin wave itself can be distinguished better from the homogenous white noise.

In conclusion we have increased phase contrast and reduced optical noise by using a magneto-optical modulator in a time-, space-, and phase-resolved BLS setup. We also demonstrated that

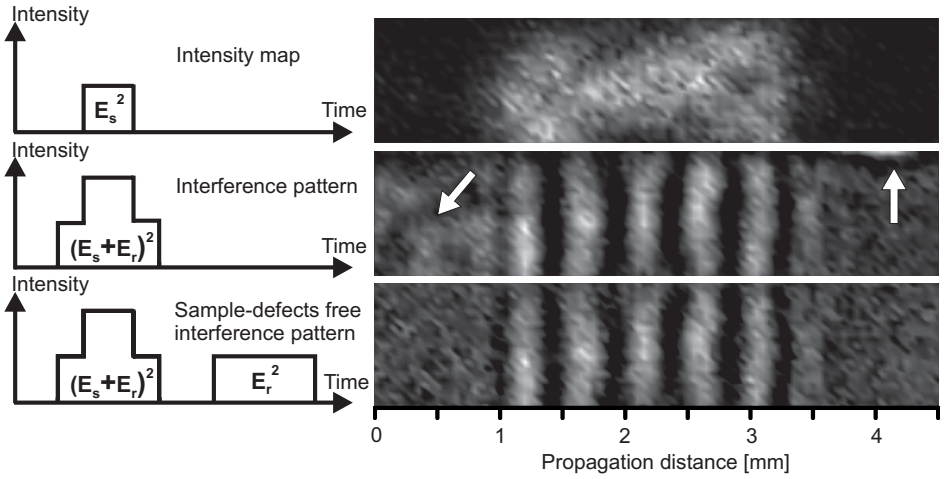

Fig. 3: Phase resolved measurement of a spin-wave packet using a magneto-optical modulator. The first two panels show the intensity map of the sample beam (E_s^2) and the interference pattern ($E_s^2 + 2E_sE_r\cos(\varphi) + E_r^2$) at 286 ns. The intensity in each profile is normalized to the respective maximum value at 286 ns. In the third panel the intensity of the pure reference profile is subtracted from the interference pattern ($E_s^2 + 2E_sE_r\cos(\varphi)$) and thus signal variations caused by optical nonuniformities are removed (white arrows).

quality of the resulting interference patterns can be improved by data postprocessing using the simultaneously recorded information about the reference light.

Support by the Deutsche Forschungsgemeinschaft within the project Hi 380/21-1 is gratefully acknowledged.

References

[1] S.O. Demokritov, A.A. Serga, V.E. Demidov, B. Hillebrands, M.P. Kostylev, B.A. Kalinikos, Nature **426**, 159 (2003).
[2] T. Schneider, A.A. Serga, T. Neumann, M.P. Kostylev, B. Hillebrands, EPL **77**, 57002 (2007).
[3] T. Schneider, A.A. Serga, T. Neumann, M.P. Kostylev, B. Hillebrands, Phys. Rev. B **77**, 214411 (2008).
[4] A.A. Serga, T. Schneider, S.O. Demokritov, M.P. Kostylev, B. Hillebrands, Appl. Phys. Lett. **89**, 063506 (2006).

6.16 Spin-wave interferometer on a waveguide

T. Schneider, A.A. Serga, and B. Hillebrands[1]

Recently we suggested spin-wave logic gates using a Mach-Zehnder type interferometer [1]. In that work we demonstrated a NOT gate as a proof of principle. Later we were able to upgrade this technique and construct a XNOR (exclusive not or) as well as an universal NAND (not and) gate [2]. One drawback of these logic gates was the use of two separated waveguides in the interferometer. Here we present the first realization of a spin-wave interferometer on a common waveguidestructure.

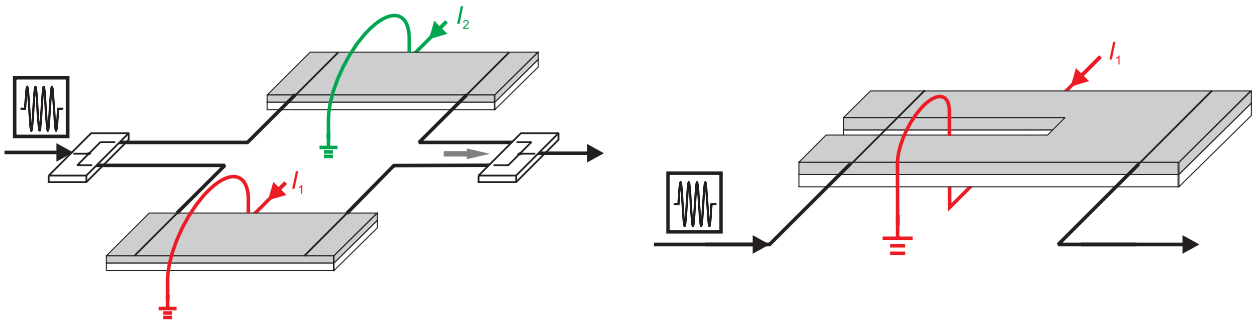

Fig. 1: Experimental setup. Left column: General design of a spin-wave interferometer. Right column: Spin-wave interferometer on a waveguide.

The left part of Fig. 1 shows the general design of a spin-wave interferometer used in the past. Spin waves are excited in two waveguides (in our experiments made from yttrium iron garnet (YIG)). A wire loop is attached to each of the waveguides (interferometer arms). The Oersted field created by a dc current through the wire leads to a phase shift of the spin wave in the appropriate arm and the wire loop works as a current controlled phase shifter. We have demonstrated that this phase shift can easily reach a value of π [1]. If one interprets a phase shift of π (or the current necessary to create that phase shift) as logical one and no phase shift (or current) as logical zero the interference signal of the two spin waves matches the output of a XNOR gate [2]. If one uses only one of the wire loops, the interferometer can be used as a NOT gate.

In our realization of the interferometer on a waveguide, for the sake of simplicity, we only added a phase shifter to one of the arms and thus are only able to use it as a NOT gate. Nevertheless the design can easily be improved to work as XNOR- or NAND-gate. The right part of Fig. 1 demonstrates the setup. We use a fork-like structure (again produced from YIG, film thickness 8 µm, width of the structure 2.5 mm) that consists of two interferometer arms (fork arms) and a combiner (fork handle).

Producing the structure from YIG has the advantage of low spin-wave damping and thus the possibility to construct the device on a macroscopic scale. This enables us to easily access the structure with microwave power and Brillouin light scattering spectroscopy (BLS). Permalloy on the contrary allows a spin-wave propagation over several tens of micrometers and thus is well suited for the fabrication of micrometer devices. The physical principles that we are using for our device would remain practically the same if one changes the medium.

[1] In collaboration with M.P. Kostylev, School of Physics, University of Western Australia, Crawley, Australia.

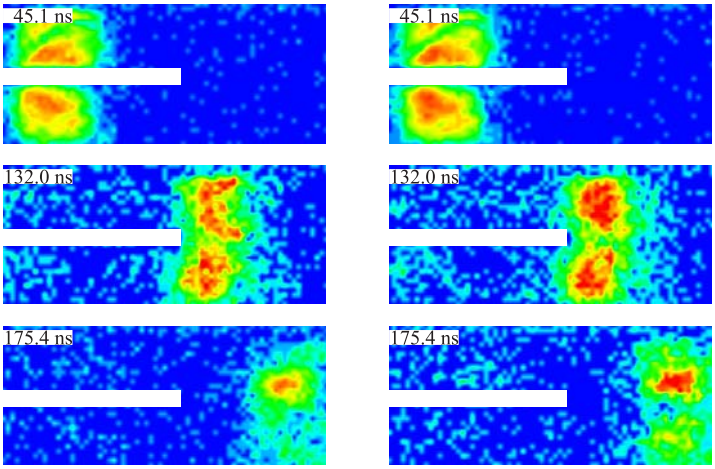

Fig. 2: Space and time resolved BLS measurements of the spin-wave interferometer. Spin-wave pulses are excited in the interferometer arms, then propagate to the combiner area where they interfere. Left column: No current applied to the wire. Interference leads to an output pattern with a maximum in the center. Right column: Current applied to the wire loop. The spin wave in the lower arm is phase shifted by π. The resulting interference pattern shows a minimum in the center and two maxima at both sides of the waveguide.

Spin waves are excited in both interferometer arms by the same microwave antenna. To avoid heating effects and to check the applicability of the proposed design we use a pulsed microwave signal to excited the spin waves as well as a pulsed current to influence the phase (length of microwave pulses: 40 ns, repetition time 25 µm). The spin-wave carrier frequency is 7.132 GHz, a magnetic bias field of 1885 Oe is applied along the waveguides axis, thus allowing the excitation of so called backward volume spin waves [3]. The resulting interference patterns in the combiner can be detected either by space and time resolved BLS [4] or by the microwave signal induced in the output antenna. Note that the BLS measurement gives the spin-wave intensity in every point of the sample, while the microwave signal gives the integrated intensity along the antenna.

The left column of Fig. 2 shows a BLS scan of the interferometer structure without a current applied to the wire loop. The spin waves that are excited in the arms overlap and interfere in the combiner area and form a pattern with a clear maximum in the center. This structure can be understood as the first order (symmetrical) width mode of the spin wave. Note that there is no visible back reflection at the transition.

If one applies a current to the wire loop, the spin-waves in both arms are turned out of phase to each other. The right column of Fig. 2 demonstrates this for a current that corresponds to a phase shift of π. As a result the interference picture in the combiner is changed. One now observes a minimum in the center and two maxima at both sides of the waveguide. In contrast to the previously discussed case this corresponds to the second order (unsymmetrical) width mode.

Applying a current to the loop thus allows us to switch the output signal from a symmetrical to an antisymmetrical mode. If we define the applied current as logical one and no current as logical zero (the same definition that was used for the logic gates in [2]), the output signal corresponds to a logical NOT gate (where logical one is attributed to the symmetrical mode and logical zero to the antisymmetrical mode). The output mode configuration can, for example, be read out by the BLS signal obtained in the center of the waveguide.

An easier approach is the use of an additional microwave antenna as shown in Fig. 1. Since the two maxima in the unsymmetrical mode are shifted in phase by π in respect to each other, the microwave output signal in this case is minimal. Figure 3 shows the intensity of this signal as a function of the applied current. The huge difference (nearly 10 dB) between minimal signal and the signal without an applied current clearly demonstrate the functionality of the interferometer as a NOT gate.

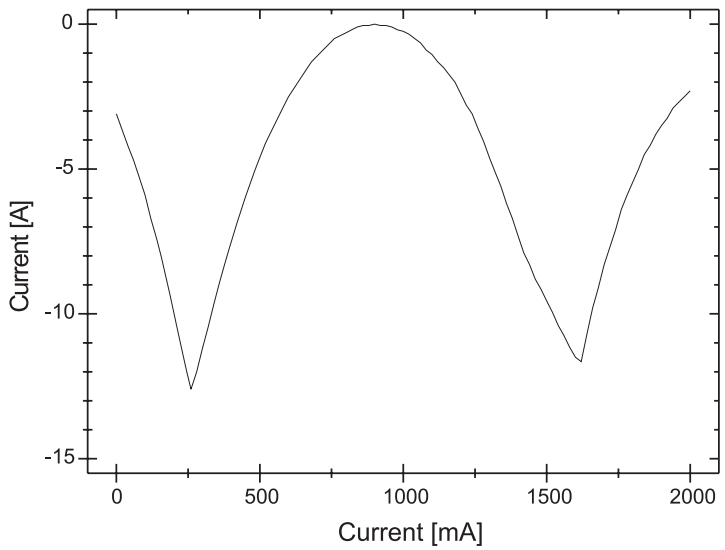

Fig. 3: Microwave output from the spin-wave interferometer as function of the current applied to the wire loop.

In conclusion we demonstrated the working principle of a spin wave interferometer on a waveguide and the possibility to use this device as a NOT gate. The construction of NAND and XNOR gates following the concepts presented in [2] using this interferometer can easily be done and thus the work presented here is an important step towards an all-spin-wave logic. Support by the Deutsche Forschungsgemeinschaft (Graduiertenkolleg 792), by the Australian Research Council, and by the European Community within the EU-project MAGLOG (FP6-510993) is gratefully acknowledged.

References

[1] M. P. Kostylev, A. A. Serga, T. Schneider, B. Leven, and B. Hillebrands, Appl. Phys. Lett. **87**, 153501 (2005).
[2] T. Schneider, A. A. Serga, B. Leven, B. Hillebrands, R. L. Stamps, and M. P. Kostylev, Appl. Phys- Lett. **92**, 022505 (2008).
[3] R. W. Damon and J. R. Eshbach, J. Phys. Chem. Solids **19**, 308 (1961).
[4] O. Büttner, M. Bauer, S. O. Demokritov, B. Hillebrands, Yuri S. Kivshar, V. Grimalski, Yu. Rapport, and A. N. Slavin, Phys. Rev. B **61**, 11576 (2000).

Chapter 7: Publications

Most publications can be downloaded from http://www.physik.uni-kl.de/hillebrands.

7.1 published

1. *Interfacial spin order in exchange biased systems*
   L.E Fernandez-Outon, G. Vallejo-Fernandez, Sadia Manzoor, B. Hillebrands, K. O'Grady
   J. Appl. Phys. **104**, 093907 (2008).

2. *Formation of guided spin-wave bullets in ferrimagnetic film stripes*
   A.A. Serga, M.P. Kostylev, B. Hillebrands
   Phys. Rev. Lett. **101**, 137204 (2008).

3. *Signal propagation in time-dependent spin transport*
   Yao-Hui Zhu, B. Hillebrands, H.C. Schneider
   Phys. Rev. B **78**, 054429 (2008)
   Virtual Journal of Nanoscale Science & Technology **18**(9), (2008).

4. *Modification of the thermal spin wave spectrum in a $Ni_{81}Fe_{19}$ stripe by a domain wall*
   C.W. Sandweg, S.J. Hermsdoerfer, H. Schultheiss, S. Schäfer, B. Leven, B. Hillebrands
   J. Phys. D: Appl. Phys. **41**, 164008 (2008).

5. *Dissipation characteristics of quantized spin waves in nano-scaled magnetic rings structures*
   H. Schultheiss, C.W. Sandweg, B. Obry, S.J. Hermsdoerfer, S. Schäfer, B. Leven, B. Hillebrands
   J. Phys. D: Appl. Phys. **41**, 164017 (2008).

6. *Ultrafast magnetization processes*
   B. Hillebrands
   J. Phys. D: Appl. Phys. **41** 160301 (2008).

7. *Scattering of backward spin waves in a one-dimensional magnonic crystal*
   A.V. Chumak, A.A. Serga, B. Hillebrands, M.P. Kostylev
   Appl. Phys. Lett. **93**, 022508 (2008).

8. *Phase reciprocity of spin-wave excitation by a microstrip antenna*
   T. Schneider, A.A. Serga, T. Neumann, B. Hillebrands, M.P. Kostylev
   Phys. Rev. B **77**, 214411 (2008).

9. *Influence of the $L2_1$ ordering degree on the magnetic properties of Co_2MnSi Heusler films*
   O. Gaier, J. Hamrle, S.J. Hermsdoerfer, H. Schultheiß, B. Hillebrands, Y. Sakuraba, M. Oogane, Y. Ando
   J. Appl. Phys. **103**, 103910 (2008).

10. *Direct observation of domain wall structures in curved permalloy wires containing an anti-notch*
    C.W. Sandweg, N. Wiese, D.R. McGrouther, S.J. Hermsdoerfer, H. Schultheiss, B. Leven, B. Hillebrands, J.N. Chapman
    J. Appl. Phys, **103**, 093906 (2008).

11. *Microwave spectral analysis by means of non-resonant parametric recovery of spin-wave signals in a thin magnetic film*
S. Schäfer, A.V. Chumak, A.A. Serga, G.A. Melkov, B. Hillebrands
Appl. Phys. Lett. **92**, 162514 (2008).

12. *Spin-wave ferromagnetic film combiner as a NOT logic gate*
T. Schneider, A. Serga, B. Hillebrands, M. Kostylev
Journal of Nanoelectronics and Optoelectronics **3**(1),(2008).

13. *Observation of coherence and partial decoherence of quantized spin waves in nano-scaled magnetic ring structures*
H. Schultheiss, S. Schäfer, P. Candeloro, B. Leven, B. Hillebrands, A.N. Slavin
Phys. Rev. Lett. **100**(4), 047204 (2008)
Virtual Journal of Nanoscale Science & Technology **17**(6), (2008).

14. *Exchange interaction and magnetic domain formation in periodically inhomogeneous magnetic media*
S. Blomeier, B. Hillebrands, B. Reuscher, A. Brodyanski, M. Kopnarski, R.L. Stamps
Phys. Rev. B **77**, 094405 (2008).

15. *Realization of spin-wave logic gates*
T. Schneider, A.A. Serga, B. Leven, B. Hillebrands, R.L. Stamps, M.P. Kostylev
Appl. Phys. Lett. **92**, 022505-1 (2008).

16. *Spin dynamics in Magnetic Nanostructures: Micro-Brillouin Light Scattering Spectroscopy*
V.E. Demidov, S.O. Demokritov, B. Hillebrands
In: K.H.J. Buschow, R.W. Cahn, M.C. Flemings, B. Ilschner, E.J. Kramer, S. Mahajan (eds) Encyclopedia of Materials: Science and Technology.

17. *The distribution of crystalline material in obstructed stents–in need for intra-luminal surface modification?*
N. Laube, L. Kleinen, V. Avrutin, U. Böde, A. Meissner, C. Fisang
J Biomed Mater Res B Appl Biomater **87**, 590-7 (2008).

18. *Ex-vivo investigations on the friction behavior of amorphous carbon coated ureteral stents*
L. Kleinen, U. Böde, N. Laube
Diamond and Related Materials **17**, 1746 (2008).

19. *New materials with high spin polarization: half-metallic Heusler compounds*
C. Felser, B. Hillebrands
J. Phys. D: Appl. Phys. **40**, (2007).

20. *Induced anisotropies in exchange-coupled systems on rippled substrates*
M.O. Liedke, B. Liedke, A. Keller, B. Hillebrands, A. Mucklich, S. Facsko, J. Fassbender
Phys. Rev. B **75**, 220407 (2007).

21. *Thermally excited spin wave modes in synthetic antiferromagnetic stripes*
Y. Ando, Y.M. Lee, T. Aoki, T. Miyazaki, H. Schultheiß, B. Hillebrands
Jour. Magn. Magn. Mat. **310**(2), 1949 (2007).

22. *Parametically stimulated recovery of microwave signal stored in stadnding spin-wave modes of a magnetic film*
A.A. Serga, A.V. Chumak, A. André, G.A. Melkov, A.N. Slavin, S.O. Demokritov, B. Hillebrands
Phys. Rev. Lett. **99**, 227202 (2007).

23. *Resonant and non-resonant scattering of dipole-dominated spin waves from a region of inhomogeneous magnetic field in a ferromagnetic film*
M.P. Kostylev, A.A. Serga, T. Schneider, T. Neumann, B. Leven, B. Hillebrands, R.L. Stamps
Phys. Rev. B **76**, 184419 (2007).

7.2 in press

1. *Brillouin Light Scattering Investigations of Magnetic and Elastic Properties in MBE Grown Trilayer Mo/Co/Au Systems*
R. Gieniusz, T. Blachowicz, A. Maziewski, A. Petroutchik, L.T. Baczewski, A. Wawro, J. Hamrle, O. Serga, B. Hillebrands
Acta Physica Polonica A, in press.

7.3 submitted

1. *Frequency-dependent reflection of spin waves from a magnetic inhomogeneity induced by a surface DC-current*
T. Neumann, A.A. Serga, B. Hillebrands, M.P. Kostylev
submitted to Appl. Phys. Lett.

2. *Probing of a parametrically pumped magnon gas with a packet of non-resonant traveling spin waves*
T. Neumann, A.A. Serga und B. Hillebrands
submitted to Appl. Phys. Lett.

3. *Brillouin light scattering study of $Co_2Cr_{0.6}Fe_{0.4}Al$ and Co_2FeAl Heusler compounds*
O. Gaier, J. Hamrle, S. Trudel, A. Conca Parra, B. Hillebrands, E. Arbelo, C. Herbort, M. Jourdan
submitted to J. Phys. D: Appl. Phys.

4. *Determination of exchange constants of Heusler compounds by Brillouin light scattering spectroscopy: application to Co_2MnSi*
J. Hamrle, O. Gaier, Seong-Gi Min, B. Hillebrands, Y. Sakuraba, Y. Ando
submitted to J. Phys. D: Appl. Phys.

5. *Parametrically-stimulated recovery of a microwave signal using standing spin-wave modes of a magnetic film*
A.V. Chumak, A.A. Serga, G.A. Melkov, V. Tiberkevich, A.N. Slavin, B. Hillebrands
submitted to Phys. Rev. B.

Chapter 8: Conferences, Workshops, Schools, Seminars

(shown in chronological order with the speaker named)

8.1 Conferences

8.1.1 Invited talks

B. Hillebrands:
Optics with new light: optics with spin waves
International Conference on “Nonlinear Waves - Theory and Applications”, Beijing, China, June 2008

B. Hillebrands:
Current induced spin-wave emission from ferromagnetic nano-structures
IEEE Nanotechnology Materials and Device Conference 2008, Kyoto, Japan, October 2008

8.1.2 Contributed talks and posters

L. Kleinen:
Multifunktionale Nanoschichten gegen Baktereinbiofilme
MEDICA, Düsseldorf, Germany, November 2007

S. Hermsdörfer:
Spin waves in semi-circular $Ni_{81}Fe_{19}$ ring segments in the presence of domain walls
MMM, Tampa, USA, November 2007

A.A. Serga:
Dynamics of magnon gas at the bottom of the spin-wave spectrum
MMM, Tampa, USA, November 2007

T. Schneider:
Basic and universal logic gates employing spin waves influenced by current controlled Oersted fields
MMM, Tampa, USA, November 2007

T. Schneider:
Spin-wave caustics excitation by point like antenna structures
MMM, Tampa, USA, November 2007

A. Chumak:
Design and optimization of one-dimensional YIG film based magnonic crystal
Intermag 2008, Madrid, Spain, May 2008

J. Hamrle:
Exchange constant and magnetic anisotropy in Co_2-based Heusler compounds
Intermag 2008, Madrid, Spain, May 2008

T. Neumann:
Influence of current induced magnetic inhomogeneity on spin-wave propagation
Intermag 2008, Madrid, Spain, May 2008

S. Schäfer:
Non-resonant parametric recovery of spin-wave signals
Intermag 2008, Madrid, Spain, May 2008

H. Schultheiß:
Investigation of spin-wave radiation and current controlled three-magnon-scattering in spin-torque nanocontact devices
Intermag 2008, Madrid, Spain, May 2008

A.A. Serga:
Experimental realization of spin-wave logic gates
Intermag 2008, Madrid, Spain, May 2008

A.A. Serga:
Negative transitional damping of spin waves at the bottom of magnon spectrum
International Conference on “Nonlinear Waves - Theory and Applications”, Beijing, China, June 2008

T. Neumann:
Brillouin Light Scattering Observations of Thermal Modes in Yttrium-Iron-Garnet Films
International Conference on “Nonlinear Waves - Theory and Applications”, Beijing, China, June 2008

C. Sandweg:
Spin waves and domain walls in $Ni_{81}Fe_{19}$ nanowires
Junior Euromat 2008, Lausanne, France, July 2008

G. Wolf:
Magneto-optic investigations on the dynamics of the switching behavior of TMR structures
Junior Euromat 2008, Lausanne, France, July 2008

T. Schneider:
Observation of diffractionless spin-wave beams in yttrium iron garnet films
JEMS08, Dublin, Ireland, September 2008

T. Schneider:
Phase symmetry of microwave excited spin waves
JEMS08, Dublin, Ireland, September 2008

8.1.3 Contributions to the DPG Frühjahrstagung

12 contributions: DPG Frühjahrstagung, Berlin, February 2008

8.2 Workshops and Schools

8.2.1 Invited talks

T. Neumann:
Longitudinal parametric amplification of spin waves
MATCOR student workshop, Kaiserslautern, January 2008

T. Neumann:
Observation of Spin Waves by Brillouin Light Scattering Spectroscopy
MATCOR student workshop, Mainz, June 2008

B. Hillebrands:
Nonlinear optics with new light: optics with spin waves
Workshop on high temporal and spatial resolution studies of magnetic nanostructures, Augustów, Poland, June 2008

B. Hillebrands:
Spin waves in magnetic rings: linear and nonlinear properties, non-local damping
SPINSWITCH workshop on spin momentum transfer, Krakow, Poland, September 2008

B. Hillebrands:
Brillouin light scattering spectroscopy
M-SNOW International School 2008, Nancy, France, November 2008

J. Hamrle:
Magneto-optical Kerr effect and exchange stiffness on Co_2-based Heusler compounds
International Workshop on Advances in Spintronic Materials: Theory and Experiment, Duisburg, November 2008

8.2.2 Contributed talks and posters

J. Hamrle:
Brillouin light scattering technique
4^{th} Summer school of MAINZ and 7^{th} International Symposium on New Materials with high spin polarization, Dresden, August 2008

A. Laraoui:
Investigation of spin-wave radiation in spin-torque nano-oscillators
SPINSWITCH Workshop ”Spin Momentum Transfer”, Krakow, Poland, September 2008

F. Ciubotaru:
Non-linear spin-wave radiated in spin-torque
SPINSWITCH Workshop ”Spin Momentum Transfer”, Krakow, Poland, September 2008

T. Neumann:
Phase-Shaping of Spin-Wave Pulses by Non-Resonant Parallel Pumping
MATCOR Summer School ”Simulation of Macromolecules on Different Scales”, Hall in Tirol, Austria, September 2008

8.3 Meetings

A.A. Serga:
Parametrically stimulated recovery of microwave signals stored in discrete modes of a magnon gas
Kick-off meeting and Workshop of the SFB/TRR 49 “Condensed Matter Systems with Variable Many-Body Interactions”, Schmitten, November 2007

H. Schultheiß:
Investigation of spin-wave radiation and current controlled three-magnon-scattering in spin-tourque nanoconntact devices
Dreikönigstreffen, Bad Honnef, January 2008

J. Hamrle:
Magneto-optical investigations and ion-beam induced modification of materials with high spin polarization
Project meeting of FGG 559, Sendai, Japan, March 2008

J. Harmle:
Mapping of spin polarization in lateral structures using Brillouin light scattering
Project meeting of FGG 559, Sendai, Japan, March 2008

B. Hillebrands:
Fundamentals on spin waves
SPINSWITCH Young Researchers Meeting, Kaiserslautern, June 2008

J. Hamrle:
Magneto-optical Kerr effect: Introduction to setup
SPINSWITCH Young Researchers Meeting, Kaiserslautern, June 2008

T. Neumann:
Probing of a Magnon Gas by Non-Resonant Traveling Spin Waves
TRR-Annual Retreat, Waldthausen September 2008

8.4 Invited colloquia

B. Hillebrands:
Laudatio
Award ceremony of doctors honoris causae A. Fert, P. Grünberg and S.S.P. Parkin, RWTH Aachen, Germany, November 2007

B. Hillebrands:
Linear and nonlinear optics with new light: optics with spin waves
Institutskolloquium, MPI Halle, November 2007

B. Hillebrands:
Lineare und nichtlineare Optik in neuem Licht: Optik mit Spinwellen
Physikalisches Kolloquium, Universität Regensburg, December 2007

B. Hillebrands:
Lineare und nichtlineare Optik in neuem Licht: Optik mit Spinwellen
Physikalisches Kolloquium, Universität Erlangen-Nürnberg, February 2008

B. Hillebrands:
Lineare und nichtlineare Optik in neuem Licht: Optik mit Spinwellen
Physikalisches Kolloquium, Universität Stuttgart, April 2008

8.5 Seminars

H. Schultheiß:
Brillouin Light Scattering Microscopy of Magnetization Dynamics in Nano-Scaled Devices
Laboratoire de Physique des Matériaux, Nancy-Université, France, January 2008

B. Hillebrands:
Lineare und nichtlineare Optik in neuem Licht: Optik mit Spinwellen
Kompaktseminar des GRK 792, Bad Münster am Stein, April 2008

T. Schneider:
Orts-, zeit- und phasenaufgelöste Brillouin-Lichtstreuung an mikrowellenangeregten Spinwellen
Kompaktseminar des GRK 792, Bad Münster am Stein, April 2008

T. Schneider:
Phasensymmetrie von mikrowellenangeregten Spinqwellen
Kompaktseminar des GRK 792, Bad Münster am Stein, April 2008

F. Ciubotaru, A. Laraoui:
Investigation of spin-waves radiation in spin-torque nanocontact devices
International Colloquium on Magnetization Dynamics, Irsee, September 2008

S. Hermsdörfer:
Modification of the thermal spin-wave spectrum in a $Ni_{81}Fe_{19}$ stripe in the presence of domain walls
International Colloquium on Magnetization Dynamics, Irsee, September 2008

H. Schultheiß:
Coherence and dissipation of spin-wave eigenmodes in magnetic micro- and nano-structures
International Colloquium on Magnetization Dynamics, Irsee, September 2008

H. Schultheiß:
Dissipation characteristics of quantized spin waves in nano-scaled magnetic ring structures
International Colloquium on Magnetization Dynamics, Irsee, September 2008

B. Leven:
Modification of the thermal spin-wave spectrum in a $Ni_{81}Fe_{19}$ stripe by a domain wall
International Colloquium on Magnetization Dynamics, Irsee, September 2008

A. Laraoui:
Laser and DC current induced spin dynamics in magnetic nanostructures
SPINSWITCH Training, Universität Konstanz, October 2008

J. Hamrle:
Spin currents in lateral structures
SFB-Seminar “Spin currents in lateral structures”, Universität Regensburg, October 2008

H. Schultheiß:
Brillouin light scattering microscopy of magnetization dynamics in nano scaled devices
National Institute of Science and Technology, Boulder, USA, October 2008

H. Schultheiß:
Brillouin light scattering microscopy of magnetization dynamics in nano scaled devices
University of Colorado at Colorado Springs, Colorado Springs, USA, October 2008

H. Schultheiß:
Brillouin light scattering microscopy of magnetization dynamics in nano scaled devices
Colorado State University, Fort Collins, USA, October 2008

8.6 Contributions to other meetings

G. Wolf:
Halbjahresbericht (Kooperation mit PREMA)
Halbjahrestreffen des BMBF-Projektes Heuspin, September 2008

8.7 Contributions of the Institute for Thin Film Technology

8.7.1 Contributed talks and posters

L. Kleinen:
Multifunktionale Nanoschichten gegen Bakterienbiofilme
MEDICA, Düsseldorf, Germany, November 2007

L. Kleinen:
Investigations of the biofilm reducing properties of amorphous carbon on urological implants in an extended in-vitro crystallization model
8th World Biomaterials Congress (WBC) 2008 - Crossing Frontiers in Biomaterials and Regenerative Medicine, Amsterdam, Netherlands, May 2008

L. Kleinen:
Reduction of biofilm formation on a-C:H coated implants: investigation of biofilm-surface-interactions by variation of thin film properties
11th International Conference on Plasma Surface Engineering (PSE), Garmisch-Partenkirchen, September 2008

8.7.2 Meetings

L. Kleinen:
Reduction of biofilm formation on amorphous carbon coatings: "From bench to beside"
Nano2Life (N2L) Research School, Saarbrücken, May 2008

L. Kleinen:
Plasmen für biomedizinische Anwendungen
Seminar für Oberflächentechnik des Instituts für Oberflächentechnik der Technischen Universität Carolo Wilhelmina zu Braunschweig und des Fraunhofer Instituts für Schicht- und Oberflächentechnik, Braunschweig, July 2008

L. Kleinen:
Oberflächenmodifikation mit Plasmen für biomedizinische Anwendungen
Herbstsitzung des AK-Plasma, Kaiserslautern, November 2007

8.7.3 Contributions to other meetings

L. Kleinen:
Einfluss von Schichteigenschaften auf Inkrustationsneigung und Reibwertverhalten urologischer Katheter
BMBF-Projekttreffen "BioMinMed - Plasmadeponierte funktionalisierte Kohlenstoffschichten zur Minderung von Infektionsrisiken", Achenmühle, January 2008

L. Kleinen:
Einfluss von Plasmabedingungen auf Schichteigenschaften und die Bildung kristalliner Bakterienbiofilme
BMBF-Projekttreffen "BioMinMed - Plasmadeponierte funktionalisierte Kohlenstoffschichten zur Minderung von Infektionsrisiken", Achenmühle, January 2008

Appendix: Impressions from 2008

Group Excursion

Merry Christmas and a Happy New Year!